DERPARTMENT OF NANOBIOTECHNOLOGY

SURPERVISOR: Prof. Dr. Wolfgang Knoll

Surface Plasmon Optics for Biosensors with Advanced Sensitivity and Throughput

DISSERTATION FOR OBTAINING THE DOCTORAL DEGREE

UNIVERSITY OF NATURAL RESOUCES AND LIFE SCIENCES, VIENNA

SUBMITTED BY

Mana Toma, M.Sc.

VIENNA, AUGUST 2012

Acknowledgements

Abstract

Plasmonic biosensors represent a rapidly advancing technology which enables rapid and sensitive analysis of target analytes. This thesis focuses on novel metallic and polymer structures for plasmonic biosensors based on surface plasmon resonance (SPR) and surface plasmon-enhanced fluorescence (SPF). It comprises four projects addressing key challenges concerning the enhancement of sensitivity and throughput. In the project 1, an advanced optical platform that relies on reference-compensated angular spectroscopy of hydrogel-guided waves is developed. The optical setup provides superior refractive index resolution of 1.2×10^{-7} RIU and offers an attractive platform for direct detection of small analytes which cannot be analyzed by regular SPR biosensors. The project 2 carries out theoretical study of SPR imaging with advanced lateral resolution based on Bragg scattered surface plasmons (BSSPs) on sub-wavelength metallic gratings. The results reveal that the proposed concept provides improved lateral resolution and fidelity of the images. This feature opens ways for high-throughput SPR biosensors with denser arrays of sensing spots. The project 3 investigates surface plasmon coupled-emission from fluorophores in the vicinity of plasmonic Bragg-gratings. The experimental results provide leads on advancing the collection efficiency of fluorescence light by controlling the directions of fluorescence emission. This functionality can directly improve the sensitivity of fluorescence-based assays. In the last project 4, a novel sensing scheme with actively tuneable plasmonic structures is developed by employing thermo-responsive hydrogel binding matrix. The hydrogel film simultaneously serves as a large capacity binding matrix and provides means for actuating of surface plasmons through reversible swelling and collapsing of the hydrogel. This characteristic is suitable for multiplexing of sensing channels in fluorescence-based biosensor scheme.

Table of contents

1. Introduction

Analytical devices which are capable of rapid, selective and sensitive detections of biomarkers, pathogens and toxic substances with simple operation are strongly desired in clinics, food industries, environmental monitoring facilities and important facilities which can be a target of bio-terrorisms. A variety of bio-analytical methods, such as enzyme linked immunosorbent assay (ELISA), radio immunoassay, cell culture, polymerase chain reaction (PCR), a high performance chromatography, mass spectroscopy, and nuclear magnetic resonance are currently used for the analysis of molecular analytes [1]. However, these methods generally require laborious and time-consuming processes, rely on specialized laboratory equipment and have to be operated by highly trained persons. Therefore, they are not suitable for applications where the analysis time is critical, or the target molecules needs to be detected on-site.

A biosensor is an analytical device which is able to detect biological and chemical analytes quantitatively by utilizing a biological recognition element (BRE) which is in direct contact with a physicochemical transducer [2]. As it is a self-contained integrated device, a biosensor provides simplified detection system without the need of additional separation steps and sample processing. Since the first concept of biosensor was proposed in 1962 [3] which is based on bio-catalysis of glucose by enzymes attached to an electrode, a variety of biosensors have been developed for broad range of applications in the important fields including medical diagnostics, drug discovery, food safety, environmental monitoring and homeland security [4-8]. Up to now, several biosensors including blood glucose monitors and surface plasmon resonance biosensors (Biacore) [9] have been successfully introduced into a market. The market size of biosensors is estimated to be double in next 6 years [10].

In a biosensor, biological recognition elements (BRE) which specifically interact with the target analyte are attached to physicochemical transducer which converts the biological interaction into measurable signals, see Fig. 1.1. The BREs can be natural or engineered biological components as well as chemically synthesized compounds, for example, enzyme, antibody, DNA, RNA, peptide, tissue, cell and molecular imprinted polymers (MIPs) [11, 12]. In order to retain their activity, the BREs need to be incorporated on top of a transducer by a bio-interface. The mass, optical, chemical, electrical, electrochemical or thermal changes of BRE induced by the bio-molecular interactions are converted into the sensor signals by the detectors [13].
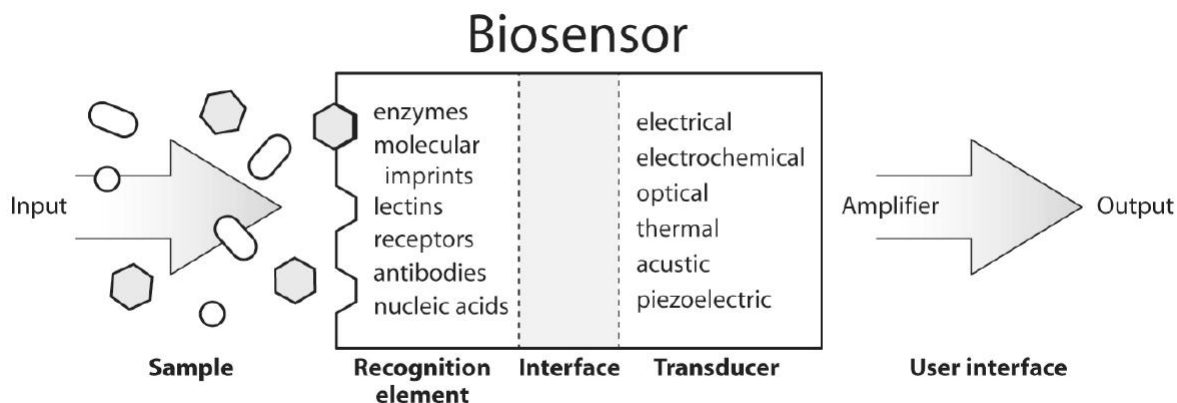
1

Fig.1.1 Schematic of biosensors represented from ref [12].

Optical biosensors have attracted great deal of attention due to its potential for rapid, sensitive and high throughput detection of target analytes. Up to now, various sensing schemes have been proposed including label-free detection based on surface plasmon resonance (SPR) spectroscopy, optical waveguide spectroscopy, interferometry [13] as well as fluorescence detection [14]. Among them, SPR-based sensors hold a prominent position and have become one of the standard laboratory equipments for biomolecular interaction analysis (BIA) since the commercial SPR sensor was released from Pharmacia Biosensor AB (the company became Biacore AB followed by merging with GE Healthcare) in 1990 [9]. Nevertheless, the performance characteristics of SPR biosensors including sensitivity and sensor throughput need to be advanced in order to bring them into practical applications. A variety of approaches has been introduced by means of advancing SPR biosensor instrumentation [15], manipulating surface plasmons mode [16] as well as utilizing signal amplification schemes [17]. In particular, the recent advancement of nanotechnologies and material sciences have provided new concepts of plasmonic devices utilizing nano-structured plasmonic surfaces [18, 19] and hybrid systems consisting of metal and external stimuli responsive materials [20-22]. These newly generated systems open a straightforward way to manipulate light confined by surface plasmons which is essential for fundamental studies of plasmonics as well as their biosensors applications [23, 24]. This thesis mainly focuses on the techniques which can manipulate light interacting with surface plasmons within a scope of biosensor applications.

2. Fundamental principles

2.1. Surface plasmons on metallic surfaces

2.1.1. Basic properties of surface plasmons on a planar metallic surface

Surface plasmons (SPs) are collective oscillations of free electrons at metal/dielectric interfaces. Further, a plane interface between two semi-infinite non-magnetic metal and dielectric is considered as shown in Fig.2.1a. The optical properties are described by frequency-dependent complex dielectric constant $\varepsilon_m(\omega)$ for the metal and real dielectric constant $\varepsilon_d(\omega)$ for the dielectric layer. The Cartesian coordinate system is used with x-y plane in parallel to the metal/dielectric interface and z-axis perpendicular to the surface. The electromagnetic wave propagating in x-direction at a metal/dielectric interface is assumed. As SPs are associated with oscillation of surface charge density, their field exhibits transverse magnetic (TM) polarization with electric field components in x and z directions. The dispersion relation of SPs is obtained from Maxwell equations with standard boundary conditions [25]. The dispersion relation of SPs can be expressed as:

$$k_{sp} = \frac{\omega}{c}\sqrt{\frac{\varepsilon_m \varepsilon_d}{\varepsilon_m + \varepsilon_d}} = k_0 \sqrt{\frac{\varepsilon_m \varepsilon_d}{\varepsilon_m + \varepsilon_d}} \; , \tag{1}$$

where ω, c and k_0 denote angular frequency, speed and propagation constant of light in vacuum, respectively. Noble metals such as gold, silver and copper can support SPs in the visible spectrum of light. Fig. 2.1b shows a typical dispersion relation of SPs at gold surface in contact with air and that of propagating light in air. The wavenumber of light propagating in dielectric k_{ph} holds:

$$k_{ph} = \frac{\omega}{c}\sqrt{\varepsilon_d} = \frac{2\pi}{\lambda}\sqrt{\varepsilon_d} \; , \tag{2}$$

where λ denotes the wavelength of light. The dielectric constant of gold was obtained from Drude model with a plasma frequency of bulk Au of $\omega_p = 1.37 \times 10^{16}$ rad/s [26] and the imaginary part of the dielectric constant was omitted.
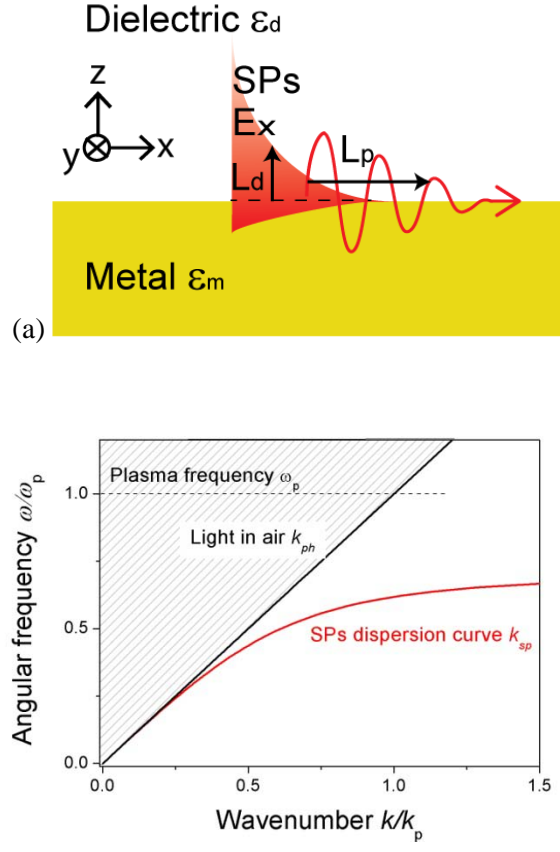
(a)

(b)

Fig.2.1 (a) Schematic of surface plasmons propagating at a metal/dielectric interface. (b) The dispersion relation of light in air (black line) and surface plasmons at a gold/air interface (red line). The angular frequency and the wavenumber are normalized by the plasma frequency of gold ($\omega_p = 1.37 \times 10^{16}$ rad/s) and the wavenumber of light at plasma frequency ($k_p = 4.59 \times 10^7$ 1/m), respectively.

As the dielectric constant of real metals is complex due to Ohmic losses, the propagation of SPs is damped. The complex propagation constant of surface plasmons can be expressed as [25]:

$$k_{sp} = k'_{sp} + ik''_{sp} = \frac{\omega}{c}\sqrt{\frac{\varepsilon'_m \varepsilon_d}{\varepsilon'_m + \varepsilon_d}} + i\left[\frac{\omega}{c}\left(\frac{\varepsilon'_m \varepsilon_d}{\varepsilon'_m + \varepsilon_d}\right)^{2/3} \frac{\varepsilon''_m}{2(\varepsilon'_m)^2}\right], \tag{3}$$

where k'_x and k''_x denote real and imaginary part of the propagation constant of surface plasmons, ε'_m and ε''_m are real and imaginary part of the dielectric constant of metal. The imaginary part of the propagation constant leads to a distance at which SPs can propagate along a metal surface. The distance is quantified by a propagation length L_p where the electric field intensity of SPs drops to $1/e$:

$$L_p = \frac{1}{2k''_{sp}}. \tag{4}$$

4

From equation (4), the propagation lengths of SPs at gold/air and gold/water interface are calculated as 10.3 μm and 6.4 μm, respectively, for wavelength of λ = 630 nm.

The field of SPs exponentially decreases perpendicular to a surface. The distance where the evanescent field intensity falls to *1/e* is referred to as penetration depth L_d which can be expressed as:

$$L_d = \frac{1}{|k_{zi}|} = \left(\frac{c}{\omega}\right)\sqrt{\frac{|\varepsilon'_m| + \varepsilon_d}{\varepsilon_i^2}} \tag{5}$$

where k_{zi} (i=m, d for metal or metal, respectively) denotes the z-component of wavenumber of SPs and ε_i denotes the dielectric constant for metal or dielectric. From equation (5), the penetration depth into gold and air were calculated as 30 nm and 284 nm, respectively, at wavelength of λ=633 nm.

## 2.1.2. Excitation of surface plasmons by light

Surface plasmons can be excited by electrons or photons. In order to excite SPs by photons, the momentum of a light beam needs to be matched to that of SPs, in other word, the dispersion relation of the incident light beam and SPs need to cross. However, the wavenumber of SPs is always larger than that of the light propagating in dielectric above the metal as shown in Fig.2.1b. It indicates that the photons directly hitting the metal are not able to couple to SPs. Thus a coupler needs to be used.

Prism coupler

In the prism coupling scheme, a prism made from optical glass of higher refractive index ε_p than that of the dielectric medium ε_d ($\varepsilon_p > \varepsilon_d$) is used to enhance the wavenumber of the light beam. Fig.2.2a shows the prism coupler based on the attenuated total reflection (ATR) method with Kretschmann configuration[27]. The incident beam is reflected at prism base coated with a thin metallic film at an angle θ which is above the critical angle. The evanescent field of totally internally reflected light penetrates through the metallic film with the enhanced propagation constant ($\sqrt{\varepsilon_p} \cdot k_0$). Fig. 2.2b shows the dispersion relations of SPs at gold/air interface and that of light in air and a prism. The resonant coupling occurs when a parallel component of the propagation constant of the evanescent field matches that of SPs at the outer metal/dielectric interface. The parallel x-component of wave vector of incident light is tuned by the angle of incident or wavelength in order to match that of SPs:

$$k'_{SP} = \sqrt{\varepsilon_p}\, k_0 \sin\theta \,, \tag{6}$$

where θ is the angle of incidence.
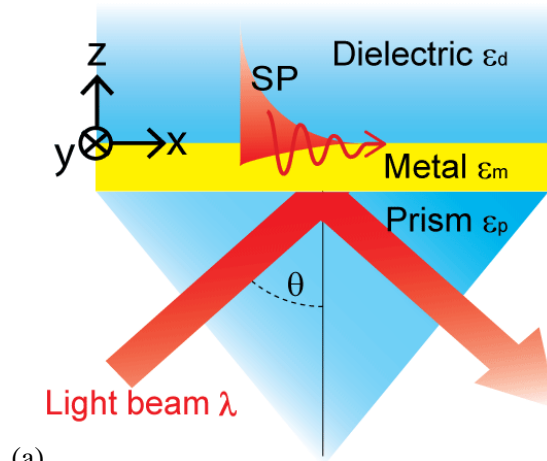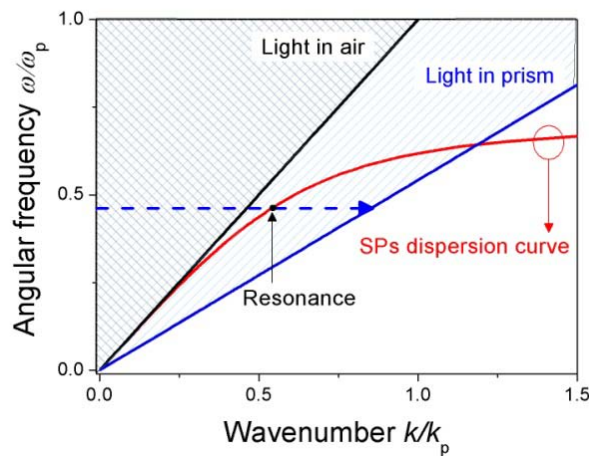
Fig.2.2 (a) Sketch of a prism coupler based on the attenuated total reflection (ATR) method in Kretschmann configuration. (b) The dispersion relation of light propagating in air (black line) and in prism (blue line). The dispersion relation of SPs at gold/air interface (red line).

Grating coupler

Alternatively, diffraction gratings can be used to increase the wavenumber of incident beam in order to excite surface plasmons. In this coupling scheme, a light beam is made incident to a metallic grating with a period of Λ at an angle of incidence θ, see Fig.2.3a. The incident beam is diffracted with various diffraction orders, which provides additional grating momentum $G=2\pi/\Lambda$. With the certain diffraction order m, the momentum of the diffracted light beam can be matched with that of SPs:

$$k'_{SP} = \sqrt{\varepsilon_d}\,k_0 \sin\theta + mG$$

(7)

where *m* is an interger. The dispersion relation of SPs on diffraction grating is shown in Fig.2.3b assuming a metallic grating made with gold in contact with air. The wavenumbers accesible by propagating light in air are indicated as an area filled by diagonal lines.
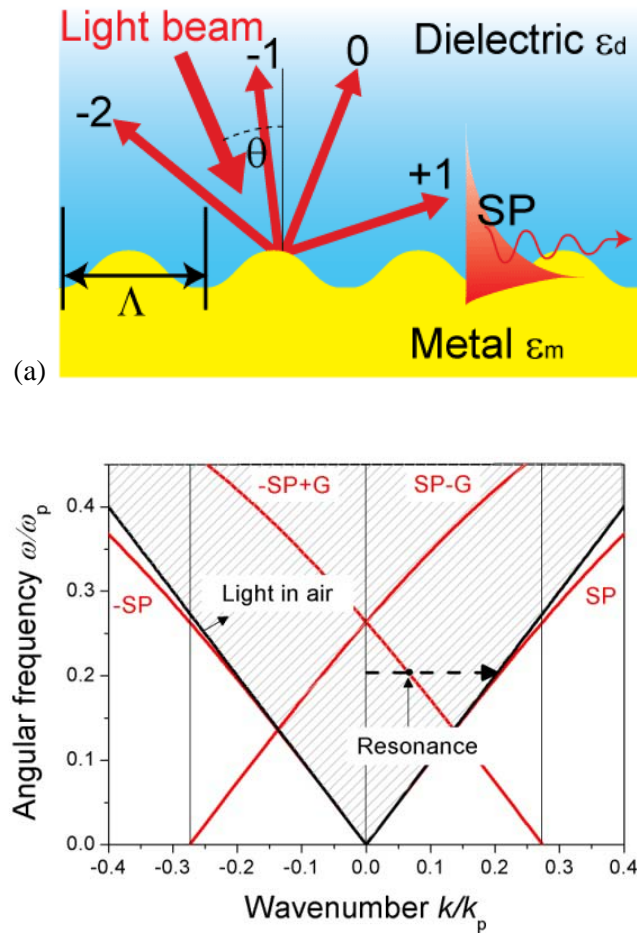

(a)

(b)

Fig.2.3 (a) Sketch of a grating coupler for the excitation of surface plasmons. (b) The dispersion relations of SPs diffracted by a diffraction grating (red lines) and light in air (black line).

2.1.3. Resonance curves and field enhancement effect

In both prism and grating-based coupling method, surface plasmon resonance (SPR) is manifested as a dip in the reflectivity spectrum. The coupling efficiency of incident light to SPs is determined as the minimum reflectivity at the resonance. In ATR method with Kretschmann configuration, the coupling efficiency can be controlled by the thickness of metallic layer. Typically, 45-50 nm thick metallic film allows full coupling which is associated to the nearly zero reflectivity at the resonance [27]. Fig. 2.4a shows an example of simulated SPR curves for a 50 nm thick gold layer on the top of LASFN9 glass prism in contact with water at wavelength of 633 and 800 nm. A computational software Winspall relying on Fresnel equations was used for calculating the reflectivity from optical multilayer systems. Fig. 2.4b shows the electric field intensity profiles upon the resonant excitation of surface plasmons.

Fig. 2.4 a-b show how the SPR spectrum and the field intensity are varied by means of refractive index of gold at different wavelength. The penetration depths of SP field into water are calculated as 182 nm and 348 nm at wavelength of 633 and 800 nm, respectively.
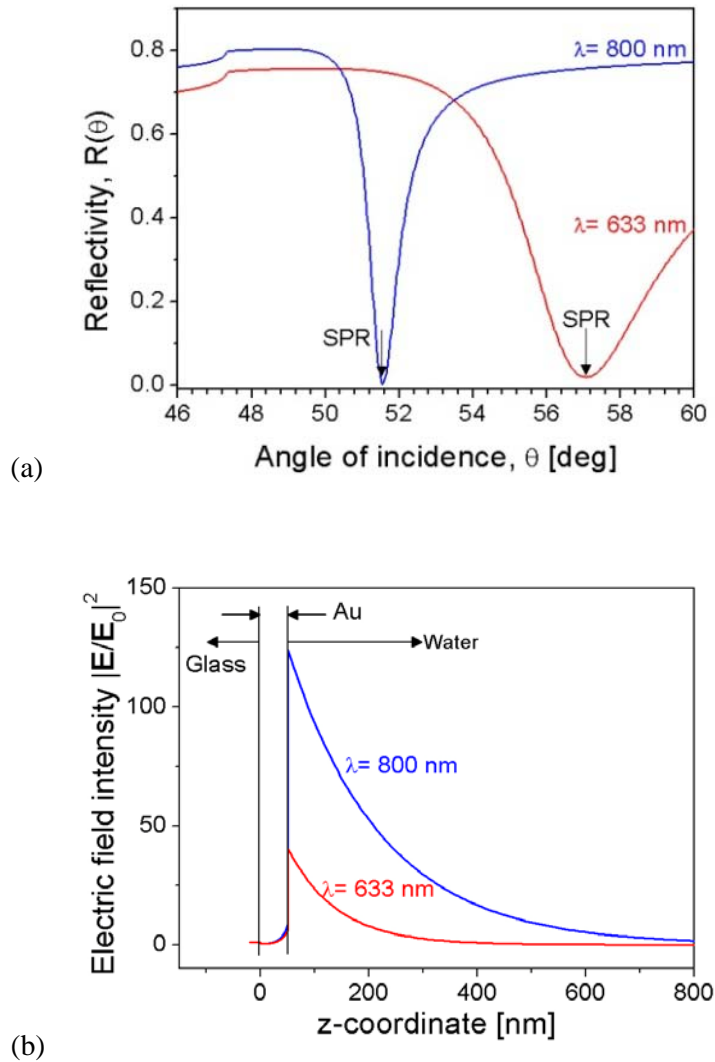

(a)

(b)

Fig. 2.4 (a) Typical SPR spectra simulated at wavelength of λ= 633 nm (red line) and 800 nm (blue line). The refractive indexes of gold used for the calculation are 0.2+i3.5 and 0.14+i5.1 for λ= 633 nm and 800 nm, respectively. (b) Simulated electric field intensity at resonance angles normalized that of the incident beam.

2.1.4. Other types of surface plasmon modes

Long range surface plasmons

Further, a different layer structure is considered in which a thin metallic film is embedded into two dielectrics with similar dielectric constants ($\varepsilon_{d1} \sim \varepsilon_{d2}$), see Fig.2.5. If the thickness of metal layer d_m is comparable to the penetration depth of SPs into metal L_p, the SPs at each interfaces couple which results in generating two new modes referred to as long range surface plasmons (LRSPs) and short range surface plasmons (SRSPs). The parallel x-component of electric field of LRSPs and SRSPs are schematically depicted in Fig. 2.5. The dispersion relation of LRSPs and SRSPs follows [28]:

$$\varepsilon_d k_{zm} + \varepsilon_m k_{zd} \tanh\left(k_{zm} d_m \Big/ 2i \right) = 0 \quad \text{(LRSPs)} \tag{8}$$

$$\varepsilon_d k_{zm} + \varepsilon_m k_{zd} \coth\left(k_{zm} d_m \Big/ 2i \right) = 0 \quad \text{(SRSPs)} \tag{9}$$

For the sake of illustration, an angular reflectivity spectra of LRSPs is simulated for the layer structure consisting of LaSFN9 glass, 900 nm thick buffer layer, 20 nm thick gold layer in contact with water based on ATR method with Kretschmann configuration at wavelength of λ=633 nm, see Fig.2.6a. It reveals that the excitation of LRPS is accompanied with a narrower resonance due to the longer propagation length of 88 μm with respect to regular surface plasmons at this wavelength. As shown in Fig.2.6b, the simulated electric field intensity exhibits a symmetric profile across the metallic layer at the resonance angle. It indicates that this mode is weakly confined along the metal surface with a larger penetration depth L_p=487 nm.
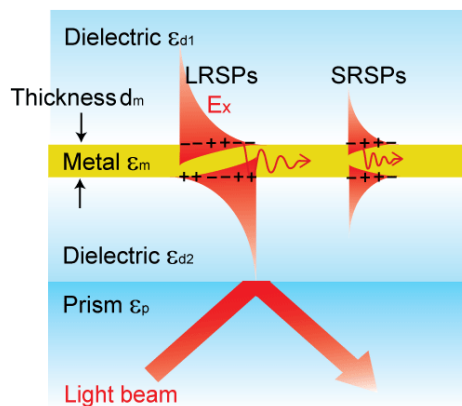

Fig. 2.5 Schematic of the layer structure supporting long range surface plasmons (LRSPs) and short range surface plasmons (SRSPs).

(a)

(b)
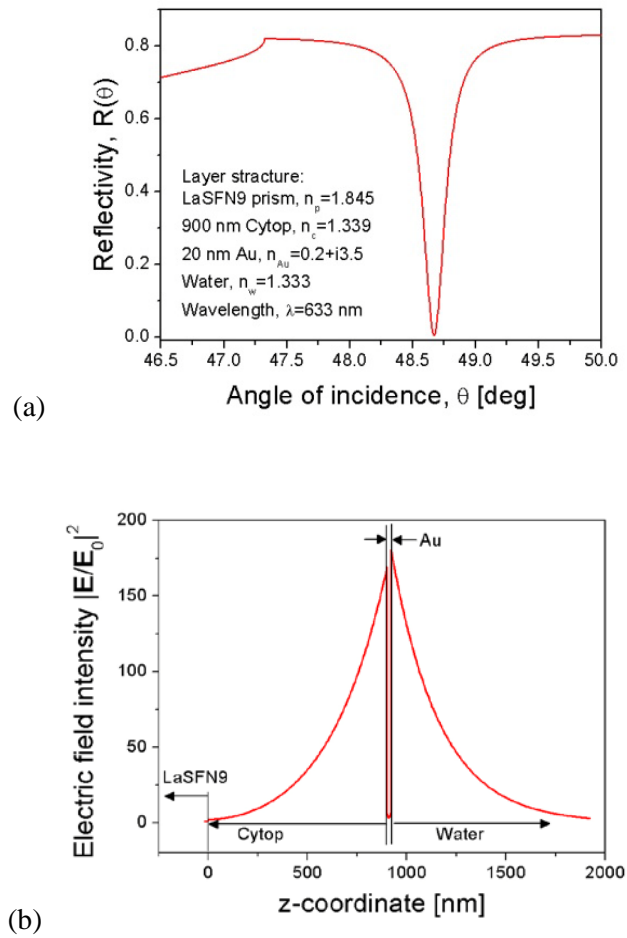
Fig. 2.6 (a) A simulated angular reflectivity spectrum of LRSPs at wavelength of λ=633 nm and (b) normalized electric field intensity profile at the resonance angle of LRSPs.

Optical waveguide mode

When a dielectric layer is attached to a metallic surface supporting SPs with a thickness comparable to the wavelength, additional guided waves that are partially coupled to SPs can be observed [29] as schematically described in Fig.2.7a. This mode is referred to as optical waveguide mode and the dielectric layer serves as a waveguide supporting layer. Fig. 2.7b shows an example of simulated reflectivity curve for the layer structure consisting of 50 nm gold and 1500 nm dielectric layer (refractive index, n_{d2}= 1.4) in contact with water at the wavelength of 633 nm. It shows that for ATR-based coupling the excitation of optical waveguide modes is manifested as sharp reflectivity dips at angles of incidence of 48.4 deg (TM_2 mode) and 51.8 deg (TM_1 mode). The simulated electric field intensity profiles at resonance angles of optical waveguide mode and SPs are shown in Fig. 2.7c. The guided wave modes associated with reflectivity drops in Fig.2.7b are identified with the number of anti-nodes in the respective electric field intensity profile.

(a)

(b)

(c)

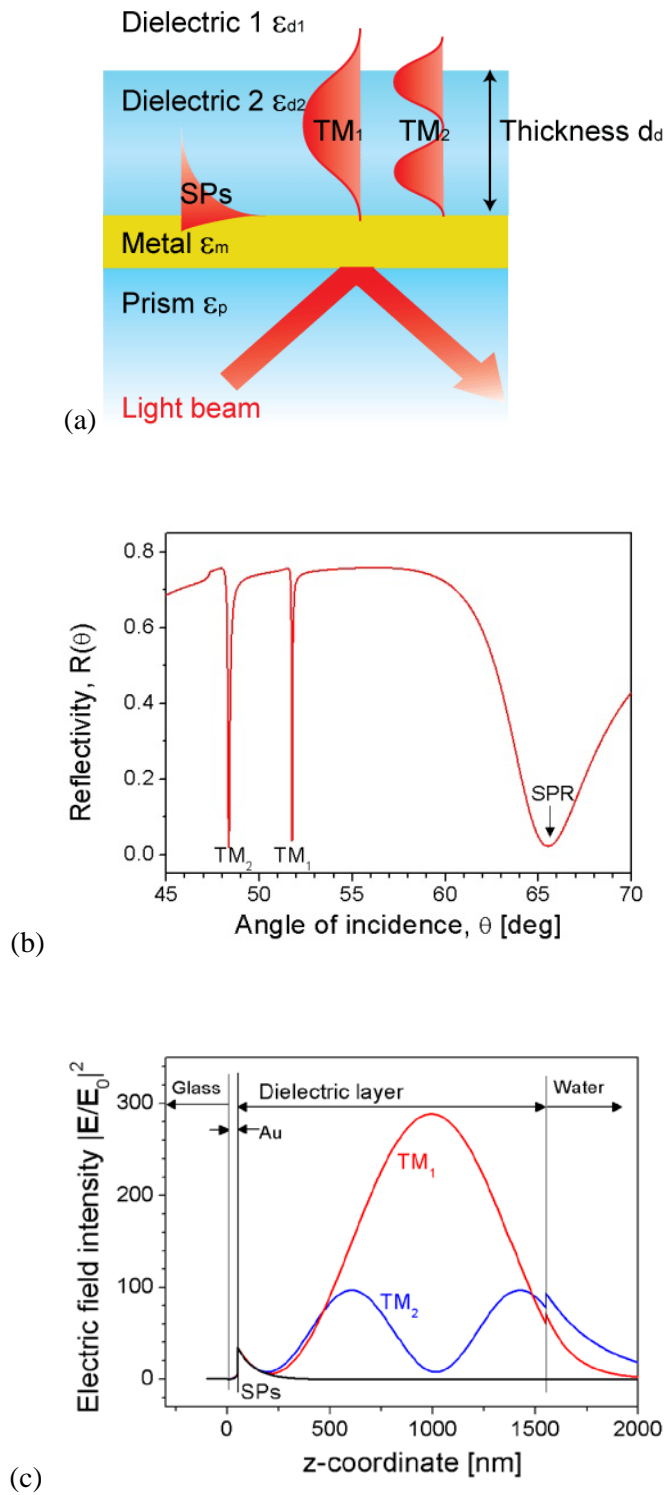Fig. 2.7 (a) Schematic of a layer structure supporting surface plasmons and optical waveguide mode. (b) A simulated angular-reflectivity spectrum for optical waveguide mode and surface plasmons. (c) Simulated electric field intensity profiles for surface plasmons (in black line) and optical waveguide mode (TM$_1$ mode in red line, TM$_2$ mode in blue line).

Bragg-scattered surface plasmons

Dense sub-wavelength metallic gratings offer another means to alter the characteristics of surface plasmon by diffraction [19, 30, 31]. In what follows, the SPs propagating on a dense sub-wavelength metallic grating with a period Λ and modulation depth d are considered, see Fig.2.8a. The dispersion relations of SPs on this metallic grating are schematically described in Fig.2.8b. The new plasmon modes appear in the dispersion relation when the Bragg condition is fulfilled between the wavenumber of SPs and the grating vector ($G = 2\pi/\Lambda$) which can be expressed as [30, 32],

$$2k'_{SP} = G .$$

(10)

In Fig.2.8b, this condition is fulfilled where the dispersion of counter-propagating surface plasmons diffracted by a grating crosses to that of propagating SPs. The constructive or destructive interference between propagating and counter-propagating SPs results in the altered dispersion relations of SPs. When the condition (10) holds, a band gap opens up in SP dispersion relation and two new modes appear at the edge of the band gap. These modes exhibit standing wave nature and are referred to as $\omega+$ mode (at higher frequency) and $\omega-$ mode (at lower frequency). For the sake of illustration, the simulated electric field intensity profiles of BSSPs $\omega+$ mode and $\omega-$ mode are shown in Fig. 2.9 a-b, respectively. The electric field intensity is localized at grating valleys ($\omega+$ mode) or peaks ($\omega-$ mode) of the periodically corrugated metallic surface. The key parameters for the excitation of BSSPs modes are the spectral position and width of a badgap which can be controlled by the period Λ and the modulation depth d of the corrugation, respectively [32]. For instance, the position of the bandgap shifts to long-wavelength when the grating period is increased and the width of the bandgap increases with the modulation depth is increased. To excite BSSPs in a visible wavelength range with gold film, the adequate period is 200 to 300 nm that is about half of the period used for grating coupling scheme.
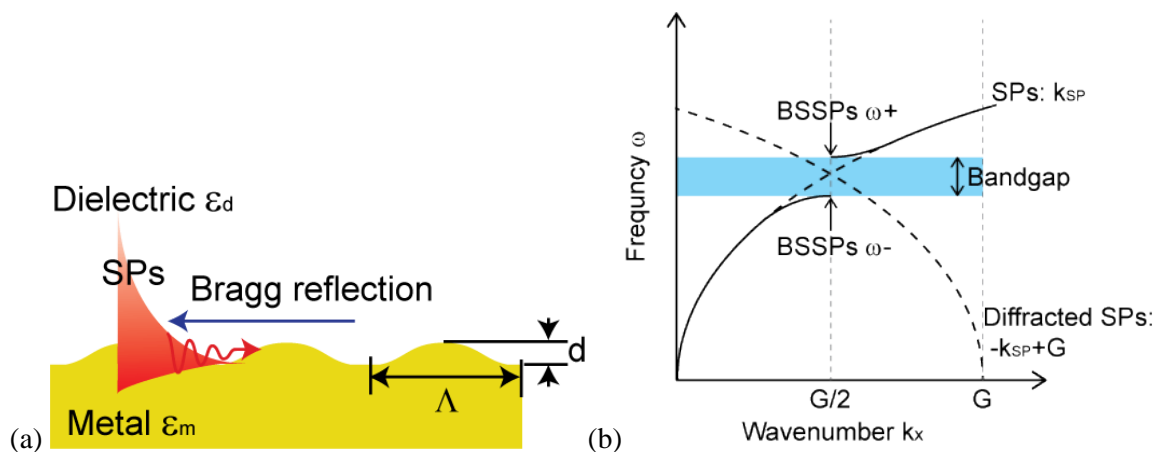

Fig. 2.8 (a) Sketch of surface plasmons propagating on a corrugated metallic surface. (b) The schematic dispersion relation of Bragg scattered surface plasmons.
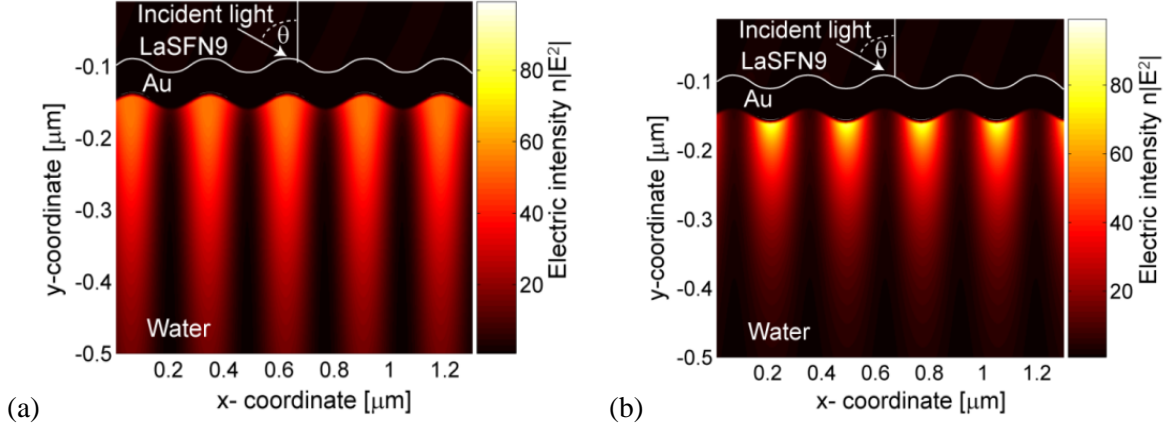
Fig. 2.9 The simulated electric field intensity of BSSPs ω+(a) and ω−(b) modes, respectively.

2.2. Fluorescence in the vicinity of metallic surface

The presence of surface plasmons alters fluorescence characteristics when a fluorescent emitter is brought close to a metallic surface. In this section, the key mechanisms through which surface plasmons mediate the fluorescence excitation and emission are presented. Based on these phenomena, the concept of enhanced fluorescence (SPF) and surface plasmon coupled emission (SPCE) is presented.

A fluorophore is a fluorescent chemical compound which can absorb light energy at specific wavelength λ_{ex} and re-emit light at higher wavelength λ_{em} ($\lambda_{em} > \lambda_{ex}$). The mechanism of photo absorption and emission can be described by the Jablonski diagram as shown in Fig. 2.10a. An orbital electron of a fluorophore is excited from the ground state to higher state by absorbing a photon. The excited electron transfers to the ground state by emitting a photon at lower energy to a free space or by non-radiative relaxation to heat. The fluorescence emission rate P_{em} can be expressed as,

$$P_{em} \propto P_{ex} \frac{P_r}{P_r + P_{nr}}$$

(11)

where P_{ex} denotes the excitation rate, P_r and P_{nr} denote radiative and non radiative decay rate, respectively [14]. The equation (11) reveals that the fluorescent emission rate P_{em} is proportional to the excitation rate. If it is far from the saturation, P_{ex} is proportional to intensity of the excitation light at absorption wavelength λ_{em}.

If a fluorophore is placed in close proximity to a metallic surface supporting SPs, new excitation and relaxation channels open up, see Fig.2.10a. Firstly, the enhanced electromagnetic field of SPs increases excitation rate P_{ex} which results in the higher fluorescent emission. Secondly, Föster energy

13

transfer occurs which leads to the fluorescence quenching. Thirdly, an additional decay channel associated with the coupling to SPs can be observed. The changes in the fluorescence decay channels due to the interaction between fluorophore and the metal surface strongly depend on the distance. Fig. 2.8b shows normalized decay rates of fluorescence emission to photons (γ_r^{ph}) and SPs (γ_r^{SP}) as well as the quenching (γ_{nr}) as a function of the distance between a fluorophore and a gold surface. From 0 to 10 nm, quenching by the Föster energy transfer is dominant. From 10 to 50 nm, fluorescence light is preferably coupled to SPs at a metallic surface. From 50 nm to farther, most of the fluorescence light is emitted into free space [17]. The fluorescence light coupled to SPs field at a metallic surface can be extracted by using reverse Kretschmann configuration [33] or diffraction gratings [34]. The re-emitted fluorescence light in to free space is called surface plasmon coupled emission (SPCE). This fluorescence light exhibits highly directional angular distribution as the emission of fluorescence light follows the coupling condition between SPs and light as discussed in the previous section (2.1.2). The enhanced fluorescence emission induced by the electromagnetic field of resonant excitation of SPs at the excitation wavelength λ_{ex} is referred to as surface plasmon-enhanced fluorescence (SPF).
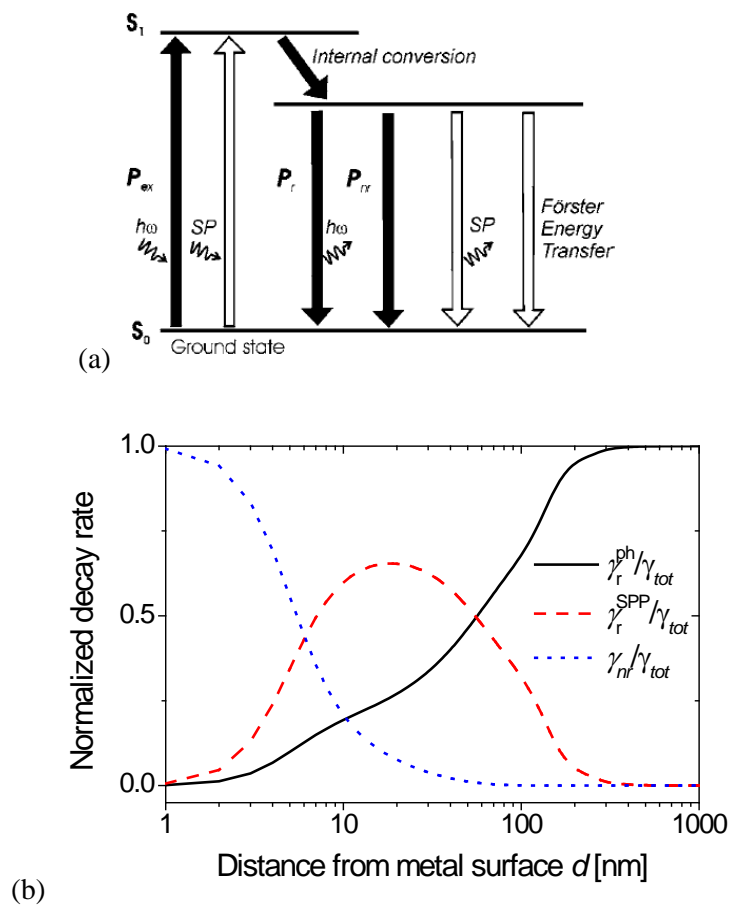

Fig. 2.10 (a) Jablonski diagram represented from ref [14]. (b) Normalized decay rate as a function of distance from the metallic surface.

2.3. Biosensor implementations

SPR is applied for the analysis of the analytes based on detection of binding-induced refractive index changes. This method provides the advantage of direct method without the need of labelling of target analyte. In addition, the implementation of SPF and SPCE to fluorescence spectroscopy offers attractive means for the amplification of signal in various fluorescence assays. In this chapter the key basic principles of SPR and SPF based biosensors are introduced.

2.3.1. Surface architectures

In order to capture target analyte on the sensor surface, the metallic surface needs to be functionalized with BREs by surface modifications. The general requirements for the surface modification include stability in aqueous environment and ability to control the density of BREs and retain their activity. The building blocks such as self-assembled monolyers [17], layer-by-layer assembled films [35], self-assembled protein structure such as S-layer protein [36], lipid bilayers [37] and hydrophilic polymers [38] have been used for the surface modification.

Self-assembled monolayers (SAMs) of alkanethiols are the most commonly used surface modification method of metallic surfaces such as gold [39, 40]. Alkane thiols consist of S-H head group connected with an alkyl chain and a functional terminate group. The functionality of the surface can be varied by changing the terminal groups of alkane thiols including amine group (NH_2), carboxyl group (COOH), polyethylene glycol (PEG), biotin or photo-reactive moieties such as benzophenone group.

In addition, surface attached hydrogel films were studied in order to increase the binding capacity on the sensor surface and utilize the additional optical functionality as an optical waveguide supporting layer [38, 41-43]. Hydrogels are highly water-swollen polymer networks of hydrophilic polymer chains. Due to their substantial water absorbance, hydrogels exhibit various attractive characteristics for biological applications, such as stability in aqueous environment, biocompatibility and non-fouling properties [38]. The chemical characteristics can be varied depending on the used monomers. Particularly, the hydrogels which are photo-crosslinkable, carry functional groups for their chemical modification (e.g. attaching BREs) and exhibit stimuli-responsive characteristics are attractive [44]. Poly (N-isopropylacrylamide) (pNIPAAm) hydrogels represent a widely explored class of polymers which exhibit thermo-responsiveness [45] . Fig.2.11 shows an example of pNIPAAm-based hydrogel that can be crosslinked by UV light exposure via benzophenone moieties and chemically modified by activation of carboxyl groups introduced to the polymer backbone. The carboxyl group can be coupled with proteins, nucleotide or arbitrary molecules which own amine groups. The surface attached pNIPAAm hydrogel thin films have been successfully utilized in various SPR-based biosensors [38, 43, 46].
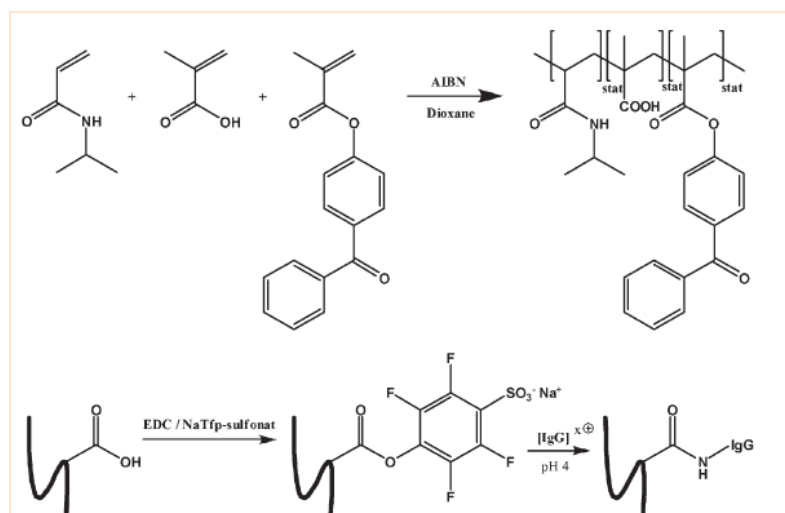
Fig. 2.11 Schematic of pNIPAAm based hydrogel and the activation scheme of carboxyl groups represented from ref [38].

2.3.2. Detection assay

In SPR based biosensors, several types of detection assays are used depending on the characteristics of the target analyte. The commonly used detection assays include direct, sandwich, competitive and inhibition assay [47]. In direct assay, the bio-recognition element (BRE) for the target analyte is immobilized on sensor surface and the binding of the target analyte is directly detected as sensor signal, see Fig.2.12A. This assay is typically used for refractometric detection of large and medium molecules. The sensitivity and selectivity of the sensor can be improved by using the sandwich assay. In sandwich assay, the additional BREs for the target analytes are brought in contact with the sensor surface after the binding of target analyte, see Fig.2.12B. In competitive assay, the sensor surface is covered with the BRE and a mixture of target analyte and the conjugate of target analyte are brought into the sensor surface, see Fig.2.12C. The target analyte and the conjugate compete to bind the limited binding site of BRE. The sensor signal is inversely proportional to the concentration of target analyte. In inhibition assay, the conjugate of target analyte is immobilized on the sensor surface and the mixture of the BRE for target analyte and target analyte is flew over the sensor surface and the binding of BRE is detected as the sensor signals, see Fig.2.12D. The competitive assay and inhibition assay are often used for the detection of small target analyte (molecular weight is less than 5 kDa) which are not able to be detected by direct assay and sandwich assay.
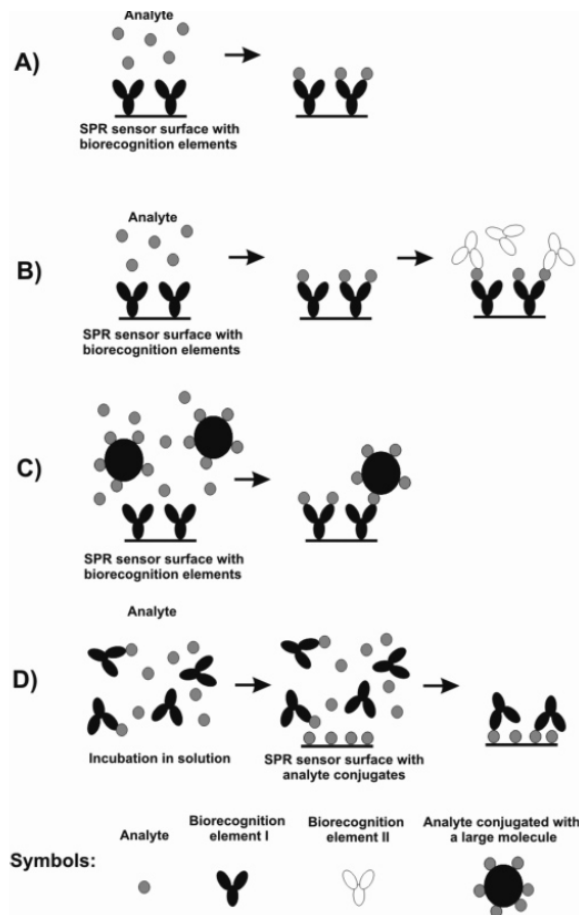
Fig.2.12 The detection format represented from ref [47].

2.3.3. Surface plasmon resonance for refractometric detection

Spectroscopy based on surface plasmon resonance was firstly applied for detection of biological samples by Liedberg et al.[48]. In an SPR biosensor, bio-recognition elements (BRE) which specifically bind to the target analytes are immobilized on the sensor surface as depicted in Fig.2.13a. Typically, a liquid sample containing target analytes is flowed over a sensor surface. The specific capture of the analyte from a sample induces a change in the refractive index on the sensor surface which alters the propagation constant of SPs results in a shifts SPR feature in the reflectivity spectrum as shown in Fig.2.13b. Depending on the interrogation of SPR changes, SPR sensor can be classified to those relying on angular, intensity, wavelength [49] or phase [50] modulation of SPR.

(a)

(b)
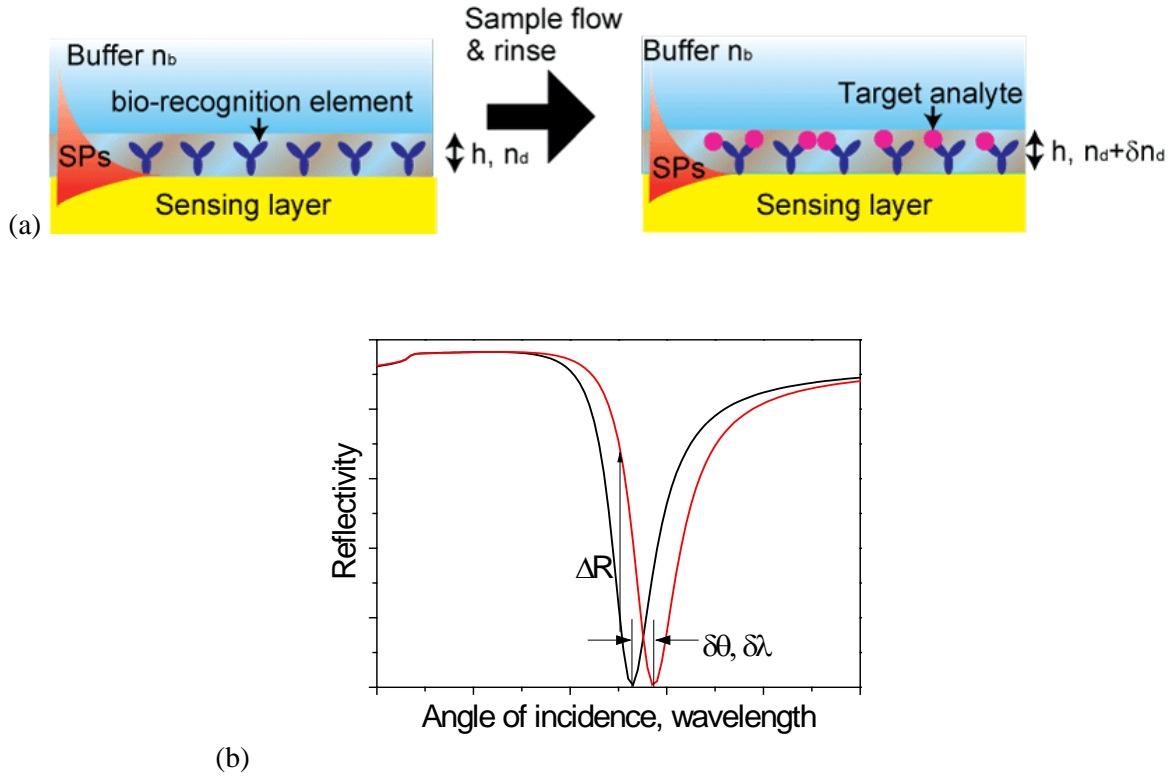
Fig. 2.13 (a) Schematic drawing of affinity binding event at sensor surface. (b) Typical SPR curve before and after the capture of target analyte.

The analysis of SPR changes (e.g. by fitting an angular reflectivity spectrum) enables the quantitative measurement of the adsorbed molecules on the sensor surface. Typically, it is quantified by surface mass density Γ defined as:

$$\Gamma = (n_d - n_b)\left(\frac{1}{dn/dc}\right)h$$

(12)

where n_d and n_b is the refractive index of biomolecule and buffer, respectively. *(dn/dc)* denotes the refractive index increment of the analyte molecules and h is the thickness of the dielectric layer composed of biomolecules. For protein analytes, the factor *dn/dc* is typically 0.18 cm³/g [51]. The detectable surface mass density change is limited by the measurable refractive index change of the used sensor instrument.

The accuracy of SPR biosensor is often described by figure of merit (FOM). A FOM is obtained as a ratio of the SPR dip shift (*S*) due to a unit refractive index (RIU) change devided by a full width at half maximum (FWHM) of the reflectivity dip. In general, the large FOM enables reaching higher accuracy. For the sake of illustration, examples of FOMs are calculated for SPs modes and optical

waveguide mode which are introduces in previous section 2.1 with angular interrogation. For conventional SPs mode (Fig. 2.4a), FOMs are 25 (S=117 deg/RIU) and 96 (S=98 deg/RIU) at the wavelength of 633 nm and 800 nm, respectively. For long range surface plasmons (Fig. 2.5b), the simulated FOM reaches to 224 (S=42 deg/RIU) at the wavelength of 633 nm. For optical waveguide mode (Fig. 2.6b), FOM for TM1 and TM2 mode are 69 (S=3.8 deg/RIU) and 193 (S=25 deg/RIU).

In SPR biosensors based on angular modulation, a shift of the resonance angle $\delta\theta$ is measured. Fig. 2.14 shows a typical optical setup for angular-resolved reflectivity measurement based on ATR method in Kretschmann configuration. In this setup, the TM-polarized incident beam is launched into prism base where a sensor chip is attached, and reflected intensity is measured by a photodetector. The angle of incidence of incident beam is controlled by a rotation stage. A set of an optical chopper and a lock-in amplifier is used to reduce the background signals.
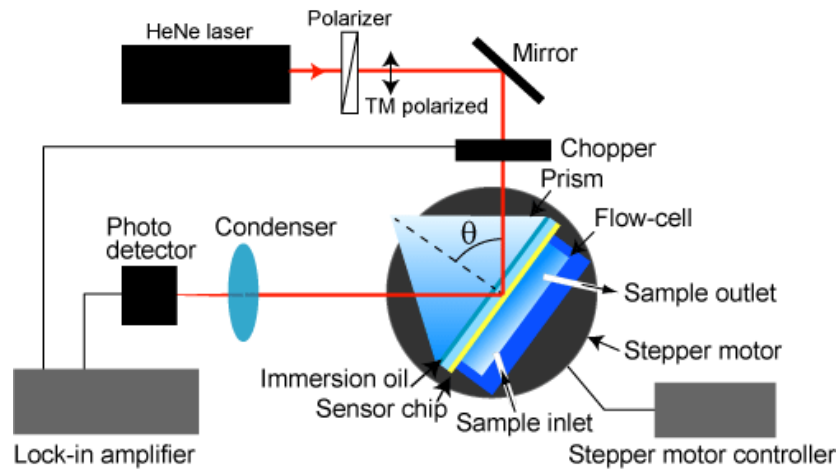
Fig. 2.14 An Optical setup for angular resolved reflectivity measurement.

Intensity modulation detection is often used for the kinetics measurement of molecular binding events. In this method, the reflected intensity is measured in time at a fixed angle of incident (shown as ΔR in Fig.2.13b. Typically, the angle of incident is set at a slightly lower angle with respect to the resonant angle where the slope of reflectivity curve can be approximated to be linear function of the angle of incident.

The intensity measurement is straightforward to increase the sensor throughput by implemention of optics for imaging [52, 53]. This optical platform is referred to as SPR imaging as well as SPR microscopy [54]. Fig. 2.15 shows a typical SPR imager using a prism coupler. A collimated monochromatic light is TM polarized with a polarizer and made incident to a prism base. A sensor

chip modified with an array of BREs is attached to the prism base. The reflected beam is then projected to two-dimensional detector array such as a charge-coupled device (CCD camera) with imaging optics. The angle of incident is set at an angle which is slightly lower from the resonance angle. The molecular binding events occurring at individual sensing spot are simultaneously detected as the changes in the reflected intensity from the corresponding area in the obtained SPR image. The parallel detections from multiple spots provide means for high throughput SPR biosensors.
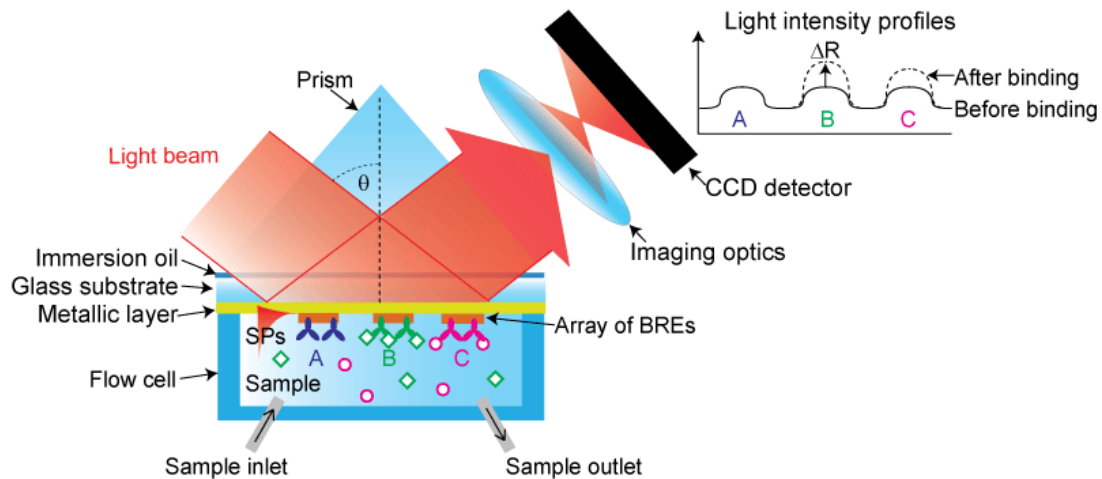
Fig. 2.15 Schematic image of a high throughput SPR biosensor based on SPR imaging.

In an SPR biosensor based on wavelength modulation, the shift of resonance wavelength δλ induced by molecular binding events is detected at a fixed angle of incidence. In this method, a collimated polychromatic light beam is used and a wavelength reflectivity spectrum is typically measured by a spectrometer [49]. The phase modulation measurement offers sensitive detection of SPR changes and is typically implemented by using the interference of a light beam coupled with SPR and a reference beam that is altered by an SPR phase shift [50].

2.3.4. Surface plasmon-enhanced fluorescence detection

Fluorescence spectroscopy based on surface plasmon-enhanced fluorescence (SPF) and surface plasmon coupled emission (SPCE) has been implemented into biosensor applications over the last years [14, 17, 55]. In fluorescence-based biosensors, typically sandwich or competitive assays are used with detection antibodies labelled with fluorophores. Fig.2.16. shows an example of the sandwich assay in which the presence of the analyte in the liquid sample is observed by binding of detection antibody labelled with fluorophore as increase of fluorescence intensity.

Fig. 2.16 Schematic of sensor surface.

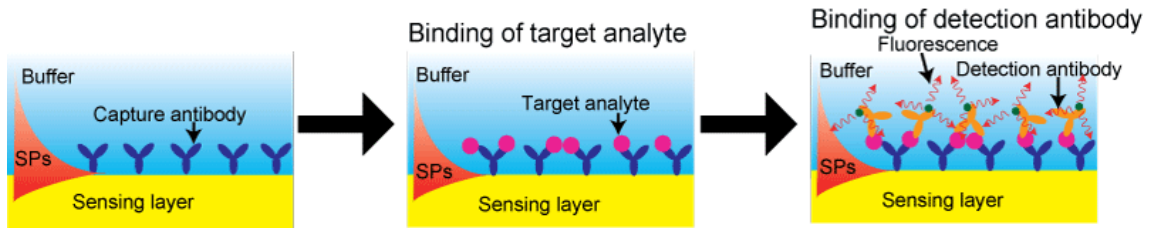In surface plasmon-enhanced fluorescence spectroscopy (SPFS), the enhanced intensity of electromagnetic field associated with the resonant excitation of surface plasmons is used for the excitation of the fluorophores [17]. Fig.2.17 shows a typical optical setup of SPFS that combines the fluorescence detection scheme with regular spectrometer based on angular interrogation of SPR. In this setup, the wavelength of the laser beam is chosen to overlap with the absorption band of the fluorophore labels. The excitation of surface plasmons provides the enhanced field intensity in close proximity to the metal surface where the specific bindings of analyte and detection antibody take place. The fluorescence signal emitted above the sensor surface through a flow-cell is detected by a photomultiplier. As seen in Fig.2.18, the fluorescence signal is amplified by the high intensity of surface plasmon field which is manifested as a strong fluorescence peak that coincides with the SPR in the angular reflectivity spectrum. Let us note that, due to the strong confinement of surface plasmon field, the excitation of fluorophores occurs selectively only at the sensor surface and thus the background signal is efficiently decreased. However, the collection efficiency of fluorescence intensity is significantly limited by the used optics and sensor configurations due to the non-directional fluorescence emission from fluorophores. Typically, only several per cent of the fluorescence light emitted from fluorophores can be detected with this sensor implementation.
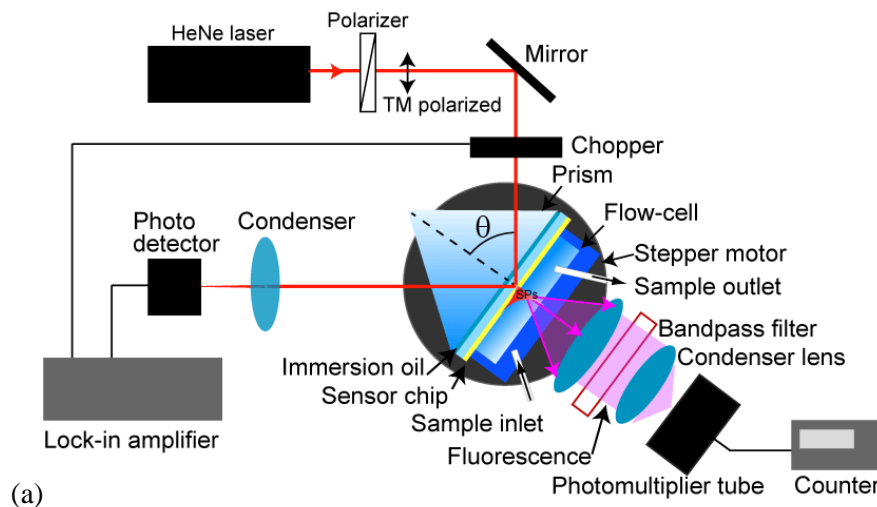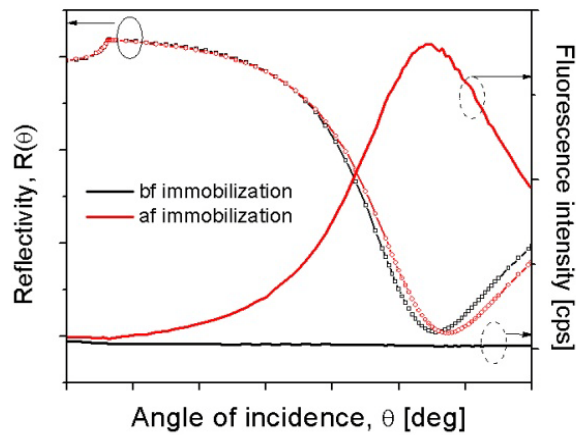

(a)

Fig. 2.17 An optical setup for surface plasmon enhanced fluorescence spectroscopy.

(b)

Fig. 2.18 A typical angular reflectivity and fluorescence spectra before and after binding of fluorophore labelled target analyte.

Surface plasmon-coupled emission (SPCE) takes advantage of the confined field of surface plasmons for efficient collecting of fluorescence light (see Fig.2.8). Surface plasmon-coupled emission provides means which enables great enhancement of the collection efficiency of fluorescence light. Reverse Kretschmann configuration with prism coupler can be used to extract the fluorescence light emitted via surface plasmons. The out-coupled fluorescence light beam is highly directional and forms a characteristic cone propagating away from the thin metallic film in a dielectric substrate. In addition, directional emission is attractive for discriminating between fluorescence and background signals. The SPCE cone can be projected to a two-dimensional detector array by using bulk optical elements [33] or can be partially collected by using an optical fiber [55].

.

2.4. Key performance characteristics of SPR-based biosensors

The key performance characteristics of a biosensor include the limit of detection (LOD), dynamic range, and detection time. In this section, recent efforts relevant to improving the sensitivity of SPR and SPFS biosensor platforms are briefly overviewed.

Refractive index resolution

The refractive index resolution is one of the most important properties of an SPR sensor which determines the measurable surface mass density change induced by the molecular binding events. It is defined as the smallest detectable bulk refractive index change in dielectric medium above the sensor surface. It is often expressed by the standard deviation of noise of the sensor output divided by bulk refractive index sensitivity [47]. The typical resolution of an SPR sensor obtained by the intensity

modulation of SPR at wavelength of 633 nm is in the range of 10^{-5} RIU [46]. For the same instrumentation, the refractive index resolution can be improved by 14 times at the same wavelength by using LRSPs (see Fig.2.4-5) through enhancing the figure of merit (FOM) [56]. Similarly, the employment of hydrogel optical waveguide mode on the top of the metallic film (see Fig.2.7) were shown to improve the resolution by one order of magnitude [46]. The detection schemes based on the detection of the SPR angle or wavelength by the analysis of whole reflectivity spectrum (angular or wavelength modulation of SPR) provide better refractive index resolution. For instance, a commercial SPR biosensor based on angular modulation - Biacore 4000 (GE Healthcare) – is capable of measurements with refractive index resolution of 1×10^{-7} RIU [9]. The combination of wavelength modulated detection scheme with a high FOM of LRSPs mode was reported to provide the refractive index resolution as low as 2.5×10^{-8} RIU [16]. Refractive index resolution obtained for the phase modulation of 2×10^{-7} RIU was reported [15].

Limit of detection

The limit of detection is defined as minimum concentration of target analyte in the sample which induces detectable changes in sensor signal. Typically, the detectable sensor signal change is determined by the one which is 3 times higher than the signal noise. In SPR biosensors based on refractometric detection, the LOD highly depends on the refractive index resolution of the instrument [57]. For plasmon-enhanced fluorescence spectroscopy, the LOD depends on the number of fluorophores per area which provides detectable signal. In addition, LODs are varied depending on mass transfer of analyte to the sensor surface (typically by diffusion), density of the bio-recognition elements (BREs) on the sensor surface and affinity constants between BREs and target analytes.

In refractometric detection, the change in the sensor signal due to the binding of target analyte on the sensor surface is proportional to the surface mass density of the adsorbed molecules. The detectable change in surface mass density can be estimated by the refractive index resolution of the SPR sensor. For example, an SPR sensor with refractive index resolution of 10^{-5} RIU at a wavelength of 633 nm is able to detect surface mass density variations of 8 pg/mm^2. This feature varies the limit of detection depending on the molecular weight of target analyte. Typically, SPR biosensors based on direct assay are suitable for the analysis of medium and large molecules. For example, the LOD of 50 pM was reported for commonly used immunoglobulin G (IgG) molecules with the molecular weight of 150 kDa by using the instrument with intensity modulation of SPR [46]. The LOD for this analyte was improved to 10 pM by using the hydrogel optical waveguide spectroscopy due to its higher FOM and enhanced binding capacity [46]. Additional amplification strategies have been employed which are based on sandwich assay and utilize metallic nanoparticle labels to enhance the refractive index changes associated with the molecular binding events [58]. This approach allowed the limit of detection of IgG at further low concentrations of 6.7 pM [58]. For the detection of small molecules

(molecular weight < 5 kDa), other types of assays such as inhibition or competitive assay are employed [59].

The biosensors relying on surface plasmon-enhanced fluorescence were shown to push the LOD by 2 to 3 orders of magnitude with respect to regular SPR with refractometric readout [17, 42, 43]. The key parameter of the sensor performance is the amplification strength of fluorescence signal which is determined by the field intensity enhancement factor associated with surface plasmon resonance (see chapter 2.1.3-4). Therefore, the probing of the sensor surface with LRSP or HOW modes which provides large field intensity enhancement (compare Fig. 2.5 and Fig.2.6 with Fig.2.4) than regular SPs results in better LOD [43, 56]. The LOD for detecting of IgG as low as 20 fM was reported for the LRSP-enhanced fluorescence spectroscopy [43]. Directional fluorescence emission of surface plasmon-coupled emission was utilized for efficient collection of fluorescence light in biosensor applications [55, 60]. The advanced LOD of 6.7 fM for human IgG was obtained by detecting fluorescence emission via SPCE with parabolic structure sensor array [61].

Parallel detection of multiple analytes
The capability of monitoring multiple reactions on the sensor surface in parallel is important for increasing of the sensor throughput and for the analysis of multiple compounds contained in a sample.

For SPR-biosensors based on refractometric detection, SPR imaging (SPRi) is most commonly used approach to increase the sensor throughput (see chapter 2.3.2) [52, 62]. The number of reactions that can be observed by SPR imaging depends on the density of individual sensing spots that are functionalized with different BRE. The common techniques for the functionalization of sensor chips for SPR imaging include micro-spotting [52], micro-contact printing [63], patterning by photolithography [64], and micro-fluidics [65]. The dimension of one sensor spot is typically larger than 100×100 μm^2 [63]. The further decreasing of the spot dimensions and thus increasing micro-arrays density is attractive for applications requiring highly parallelized analysis of molecular compounds [66]. The detectable size of sensing spot by SPR imaging is ultimately limited by the spatial resolution of the image. The spatial (lateral) resolution is defined as a minimum size of an object which can be resolved by the SPR imager. It is mainly affected by the propagation length of surface plasmons which reaches several tens of micrometers as discussed in the previous section (section 2.1). Several approaches to shorten the propagating length were pursued by using lossy metals [67] or using an excitation wavelength where the metal exhibits strong absorption [68]. However, these approaches results in the deteriorating of refractive index sensitivity that is associated to the lower figure of merit.

The fluorescence signal amplification techniques relying on SPF and SPCE have been utilized for parallel detection of fluorescence biosensors as well. Up to now, several approaches have been

reported which is based on SPF and SPCE. A surface plasmon-enhanced fluorescence microscopy was developed for parallel detection of DNA hybridization in an array format [69]. In this study, an array of DNA probes was prepared on the sensor surface. The enhanced electromagnetic field associated with the resonance excitation of surface plasmons was used to detect the target DNA labelled with quantum dots. The increase of fluorescence signal is detected by the ultra sensitive CCD camera with imaging optics and a band pass filter. The other examples are based on the SPCE. Tawa et.al integrated a plasmonic grating sensor chip into a fluorescence microscopy [65]. The detection of fluorescence emission via SPCE with parabolic structure sensor array allows sensitive and parallel detection of fluorescence signals [60].

3. Research goals

The aim of this thesis is to advance the key performance characteristics of surface plasmon resonance-based biosensors utilizing refractometric (surface plasmon resonance) as well as fluorescence (surface plasmon-enhanced fluorescence) detection principles. In particular, novel optical phenomena are investigated which hold potential for improving the sensitivity and throughput. For the SPR biosensors relying on refractometric detection, new strategies for sensitive and multi-channel detection are explored. Firstly, new optical platform based on the multi-channel angular spectroscopy of hydrogel-guided waves is developed aiming at extreme refractive index resolution and reference-compensated measurements (section 4.1). Secondly, the non-propagating surface plasmons supported by dense sub-wavelength metallic grating is investigated to improve the spatial resolution of surface plasmon imaging which is widely used for the measurements on microarrays (section 4.2). For the biosensor schemes based on the fluorescence detection, novel approaches are proposed which can potentially provide means for simpler and more efficient collection of fluorescence signals in fluorescence assays. In the third project, the utilization of plasmonic Bragg gratings is proposed in order to control the emission direction of fluorescence light mediated by surface plasmon (section 4.3). The alternative approach is investigated which is based on actuating SPs by thermal-responsive hydrogel films attached to the sensor surface. This approach holds a potential for new actively controlled plasmonic structures that can be used for multiplexing of sensing channels in SPFS biosensors (section 4.4).

4. Project overview

4.1. Development of experimental setups

Several new optical setups were developed for spatially-resolved and reference-compensated SPR experiments as well as for advanced characterization of plasmonic structures. Firstly, an optical instrument for angular interrogation reflectivity measurement of a linear array of sensing spots was developed. This setup allows multi-channel detection and reference-compensated measurement. Secondly, an optical instrument for simultaneous wavelength and angular reflectivity measurements was developed for the studies of dispersion relation of surface plasmons on nano-structured metallic films. For the spatially-resolved measurements, SPR imaging and SPF microscopy were developed. In order to control temperature on the sensor surface, two systems utilizing micro-heaters and Peltier elements were integrated to the sensor chip. LabVIEW-based programs were developed in order to control the developed setups and perform data acquisition and processing.

Angular spectroscopy of guided waves

An optical setup was developed for reference compensated angular modulation measurement as shown in Fig.4.1a. In this setup, a light from LED light source (LE-1R-C, WT&T Inc) was coupled into an optical fiber (M25L02, Thorlabs, Germany) and colimated with a lens (14 KLA 001, fl= 60 mm, CVI Melles Griot, Germany). The collimated beam passed a bandpass filter (FL632.8-10, Thorlabs, USA), a polarizer (LPVIS100-MP, Thorlabs, USA) and an optical slit (VA100/M, Thorlabs, USA). The light is focused on the sensor chip which is optically matched with the prism base by a cylindrical lens (022-0673, OptoSigma, Japan) in order to provide ranges (ψ= 1.3 deg) in the angle of incidence (θ). The reflected beam was projected to the CCD camera (piA1000-48gm, Basler AG) by using a set of imaging lens (14 KLA 001, fl= 40 mm, CVI Melles Griot, Germany) and a cylindrical lens (022-1139, OptoSigma, Japan). The prism and CCD camera were mounted on a two-circle rotation stage (Huber GmbH, Germany) in order to control the angle of incidence θ in the prism. The incident angle is adgusted to resonance angle of hydrogel optical waveguide mode or SPs. When these modes are excited, a dip in the angular distribution of reflected light intensity can be observed corresponding to the resonance angle. A flow cell with four-flow channels is attached to the sensor surface. The data processing is described in Fig.4.1b. In step 1), the reflectivity spectra are acquired over 100 times and averaged in order to reduce the noise of the sensor signal. In step 2), the averaged spectrum is fitted with a second degree polynomial function with a threshold value. In the last step 3), the fitted resonance angles are plotted in time.
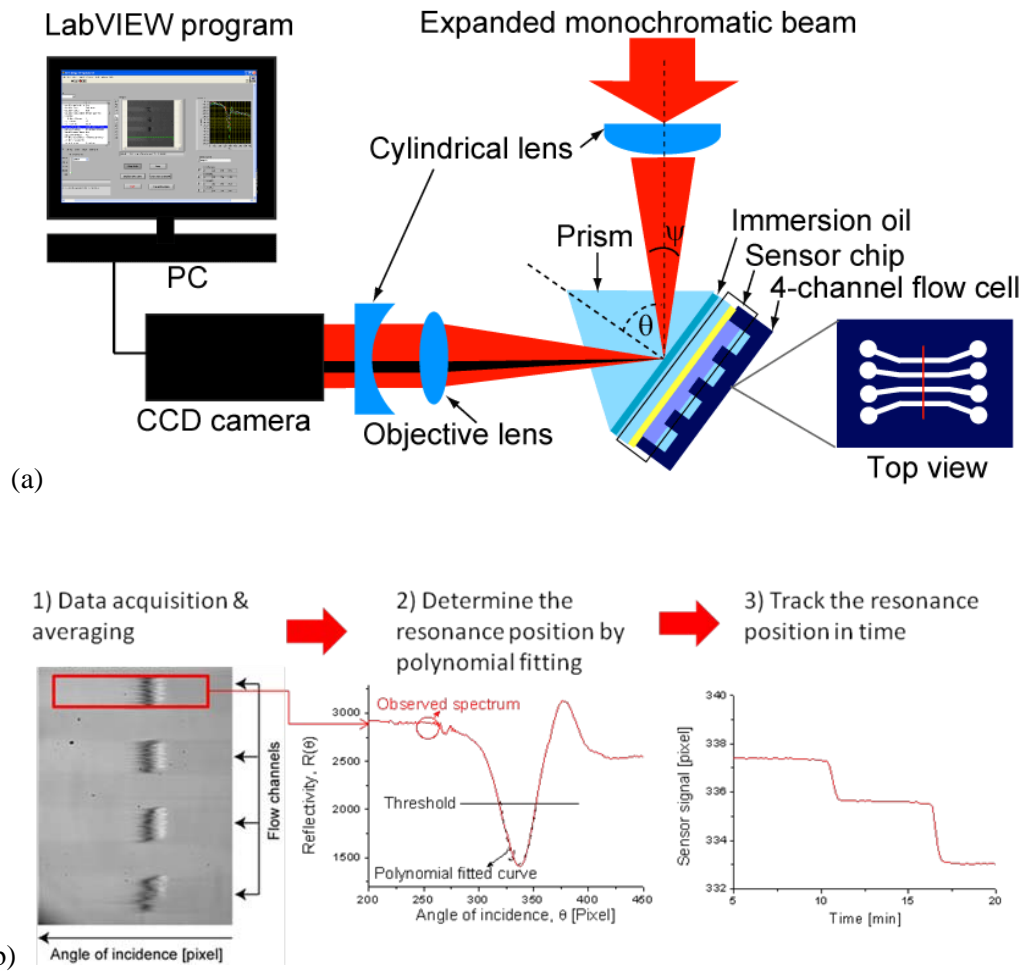
(a)

(b)

Fig. 4.1 (a) Optical setup of multichannel angular reflectivity spectrometer with 4-channel flow cell system. (b) Schematic drawing of data processing.

The developed setup is implemented into hydrogel optical waveguide spectroscopy. The RI resolution of this instrument was obtained by tracking the resonance angle of HOW mode upon the injection of PBS buffer with spikes of ethleneglycol, see Fig.4.2a. Fig. 4.2b shows a calibration curve between refractive index change in PBS buffer and change in sensor signals. The reference compensated-angular resolved measurement provides the bulk refractive index resolution of 1.4×10^{-7} RIU which is one order of magnitude better than that obtained with intensity modulated measurement [41].
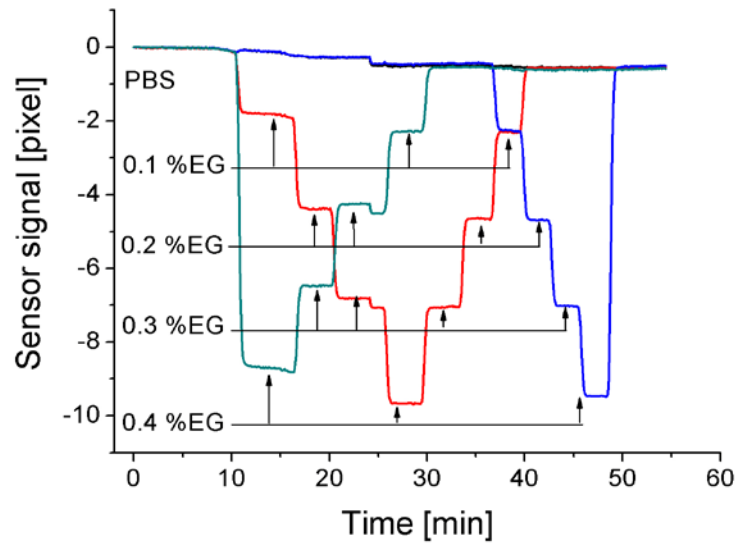
(a)
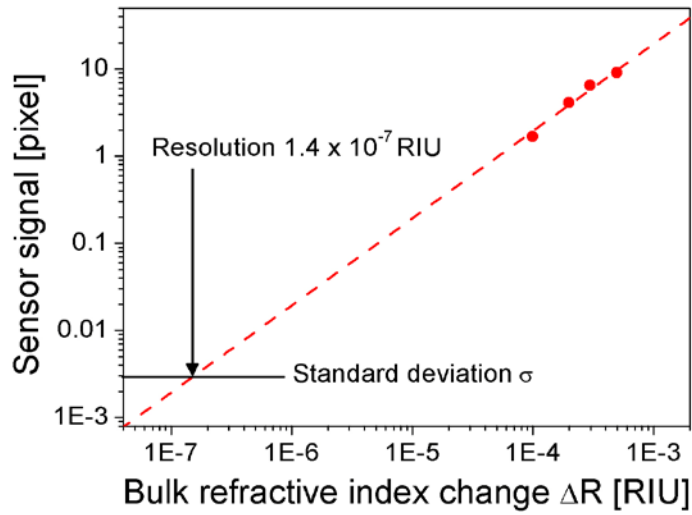
(b)

Fig. 4.2 (a) Time evolution analysis of resonance angle of HOW mode upon the injections of PBS buffer spiked with ethylene glycol at concentration from 0.1 to 0.4 %. (b) Calibration curve between bulk refractive index change in PBS buffer and the response in sensor signal.

Wavelength-angular reflectivity spectrometer

An optical setup was developed in order to observe the dispersion relation of surface plasmons as a function of wavelength λ and angle of incidence θ. As shown in Fig.4.3a, white light from a halogen lamp (LSH102, LOT-Oriel, Germany) was coupled into a multimode optical fiber (M25L02, Thorlabs, Germany) and colimated with a lens (14 KLA 001, fl= 60 mm, CVI Melles Griot, Germany). The light was polarized by a polarizer (LPVIS100-MP, Thorlabs, USA) and launched to a 90° glass prism. The sensor chip is attached to the prism base with refractive index matching liquid. The reflected light

beam was coupled into an optical fiber (M29L01, Thorlabs, Germany) and detected by a spectrometer (HR4000, Ocean Optics, USA). The prism and detectors were mounted on a two-circle rotation stage (Huber GmbH, Germany) in order to control the angle of incidence θ of the polychromatic beam in the prism. The wavelength reflectivity spectra were sequentially acquired at increasing angles of incidence. The reference spectra were taken with TE polarized light for normalization. For the sake of illustration, an example of wavelength-angular reflectivity map is presented in Fig.4.3b which shows a dispersion relation of surface plasmons propagating at gold /air interface. The developed optical setup was used for the characterization of dispersion relation of plasmonic Bragg-gratings in Project 3.
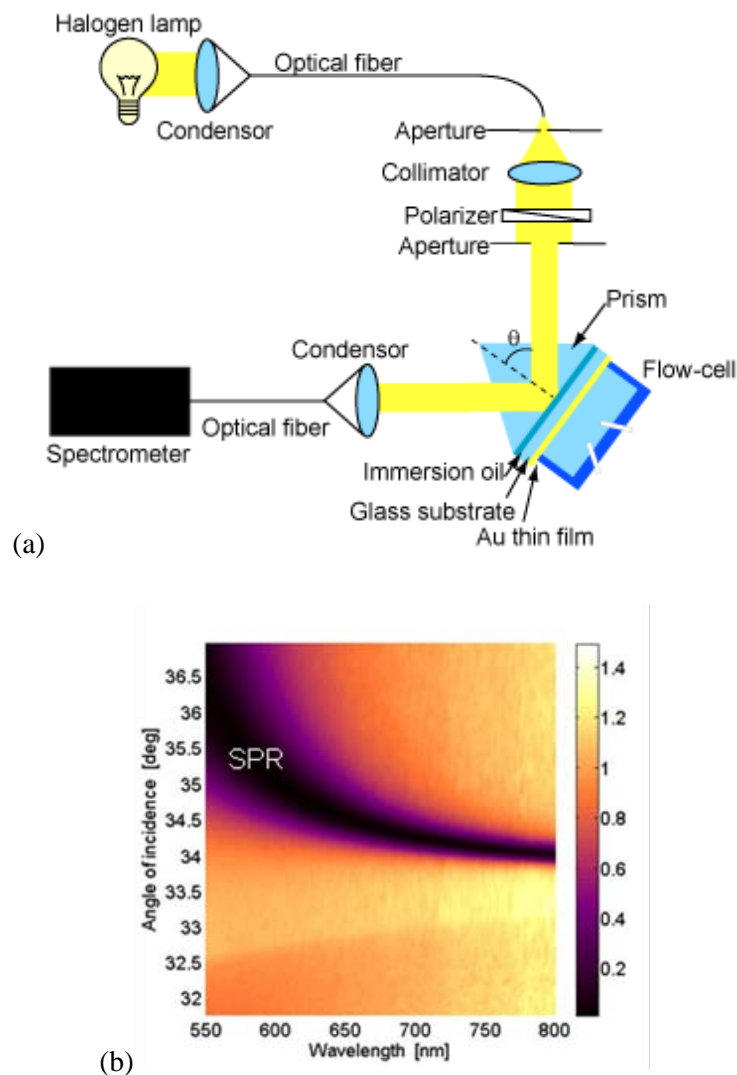

(a)

(b)

Fig.4.3 (a) An optical setup for wavelength-angular resolved reflectivity measurement. (b) A reflectivity map as a function of wavelength and angle of incidence for a gold surface in contact with air.

SPR imager

An SPR imager was implemented for spatially-resolved reflectivity measurement. As shown in Fig. 4.4, an expanded monochromatic light beam was reflected from the sensor surface at an angle of incidence fixed close to that of SPR dip and the reflectivity changes along the surface were imaged to a CCD detector (see chapter 2.3.3). In order to suppress the interference effects, a low coherent light LED-based source (LE-1R-C, WT&T Inc.) or a white light (LSH102, LOT-Oriel, Germany) with a narrow band pass filter (FL632.8-10, Thorlabs, Germany) were used. For the imaging of the sensor surface, a lens objective (UNIFOC 58, Schneider Kreuznach, Germany) and a CCD camera (piA1000-48gm, Basler AG) were used. The spatial resolution of developed SPR imaging setup was estimated to 2.5 μm. This setup was used for the time evolution measurement of thermo-responsive hydrogel films in the project 4.
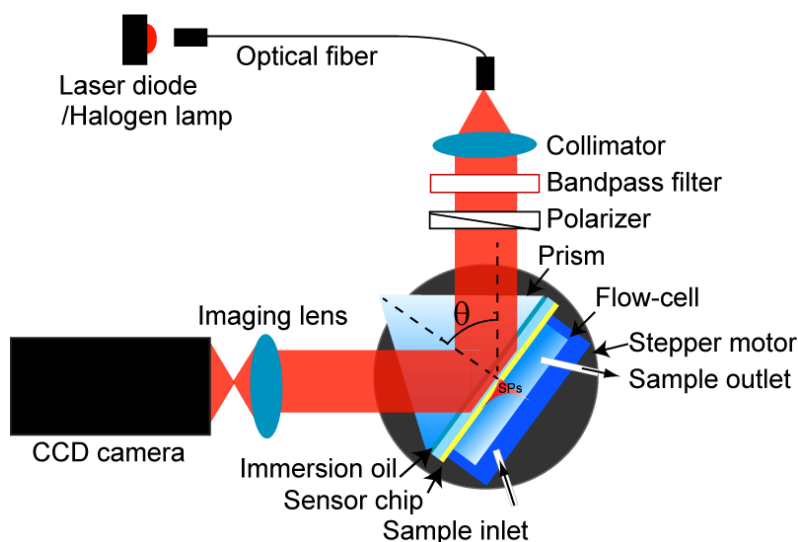

Fig.4.4 An optical setup for SPR imaging.

Surface plasmon-enhanced fluorescence microscope

Additional optical setup was developed in order to obtain spatially resolved surface plasmon-enhanced fluorescence images. Fig. 4.5 shows the schematic image of the setup. The laser beam is TM polarized by a polarized and expanded and collimated by a spatial filter consisting of a microscope objective (NT38-343, Edmund optics, USA), a pinhole (10 μm diameter, 10PP-10, Standa, Italy) mounted in x-z positioned (5ZYP, Standa, Italy) and a plano-convex lens (LPX-30.0-51.9-C, Melles Griot, Germany). The expanded beam is launched into a prism and made incident to a sensor chip which is optically matched with a prism base. A flow cell is attached to the sensor surface in order to flow the sample liquid. The prism base is mounted on a on a two-circle rotation stage (Huber GmbH, Germany) in order to control the angle of incidence θ of the polychromatic beam in the prism. An electron multiplying charge-coupled device (EM-CCD iXon+885, Andor Technology, Ireland) is mounted on the rotation stage which rotates the prism with a set of bandpass filter (670FS10-25,

LOT-Oriel, Germany) and a camera lens (UNIFOC 58, Schneider Kreuznach, Germany). The fluorescence images are taken upon the resonant excitation of surface plasmon by controlling the angle of incidence. The developed setup is employed in project 4.
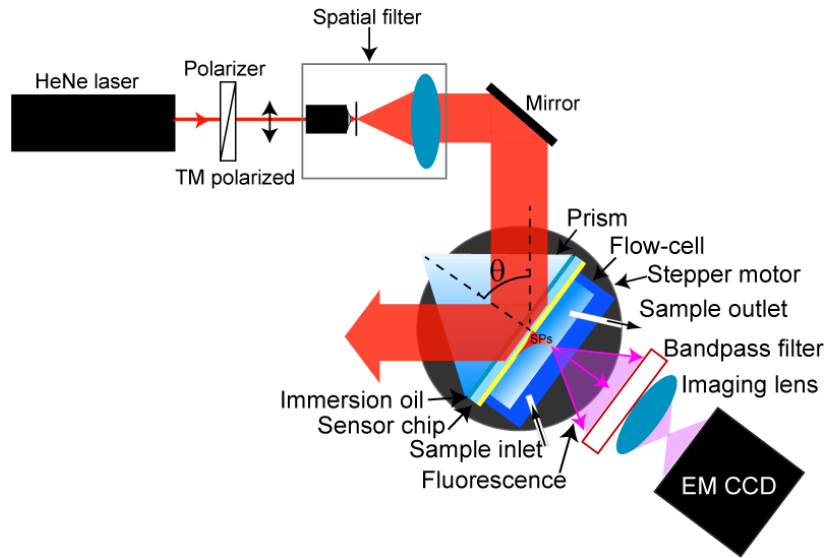
Fig.4.5 An optical setup for SPF microscopy.

Temperature controlling systems

Two different temperature controlling systems are integrated in order to characterize equilibrium and dynamics of swelling state of the hydrogel in project 4. Firstly, a temperature controlling system for the entire sensor chip is developed. The system consists of a flow cell, Peltier devices (QC-31-1.4-8.5M, Conrad, Austria), a temperature sensor (TCS10K5, Wavelength Electronics, USA), heat-sinks and fans, see Fig.4.6. A new flow cell is designed in order to make the sensor chip thermally isolated and stable. The Peltier devices and the temperature sensor are connected to the temperature controller (LFI3751, Wavelength Electronics, USA) which controls the current flow to Peltier device based on the feedback signals from the temperature sensor. The developed system enables the temperature range in 20 to 40 °C.

Fig. 4.6 The picture of temperature control system for whole sensor chip.

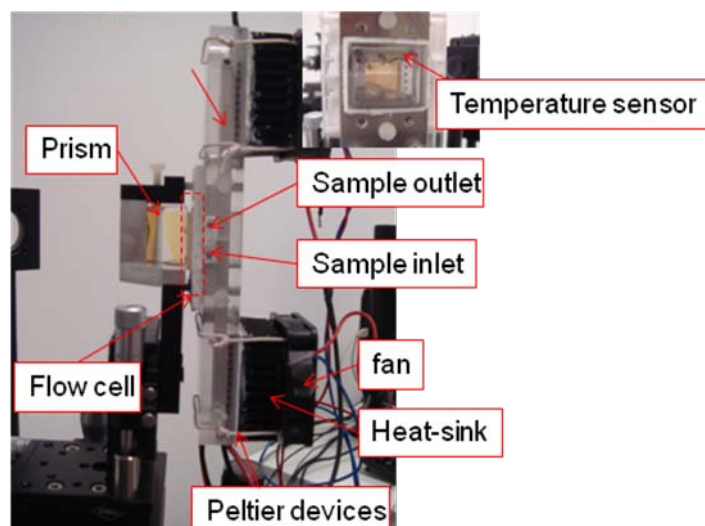The rapid temperature modulator is developed based on the implementation of Indium Tin Oxide (ITO) micro-heaters in to an SPR sensor chip. This sensor chip (shown in Fig.4.7b) is made by following procedure schematically drown in Fig. 4.7a, firstly microheaters with gold electrodes (50 nm thick gold layer with 3 nm of Ta adhesion layer) and ITO pads (thickness 25 nm) were deposited on BK7 glass using magnetron sputtering (UNIVEX 450C, Leybold Systems, Germany) and laser-cut stencil masks (PIU-PRINTEX, Austria). Afterwards, 700 nm thick Cytop fluoropolymer was spincoated and baked at temperature T = 160 ℃ for 1 hour on the hotplate. 20 nm thick Au pads were prepared on top of ITO microheaters in a same manner of deposition of ITO pads. In order to locally heat the sensor surface, gold electrodes were connected to a current modulator (NI9265, National Instruments). The local temperature changes at SPR sensor pads induced by a current apply to ITO microheaters are optically calibrated by using temperature depending refractive index change of water (see the attached publications for details). The time-evolution kinetics measurements reveals that the local temperature of a sensor pad can be heated over 10 °C within 100 ms.
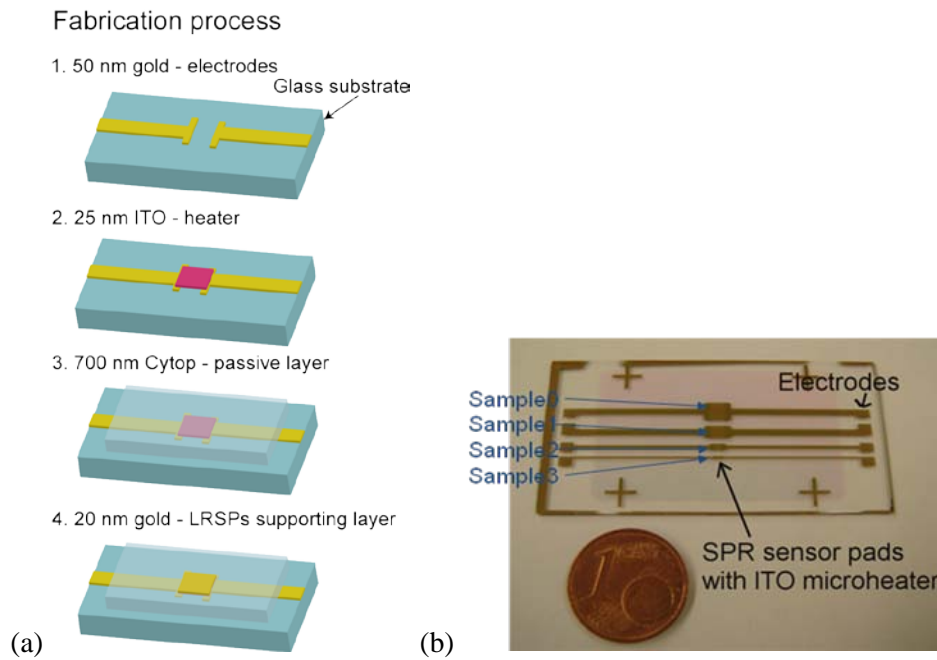
.

Fig. 4.7 (a) A picture of a sensor chip supporting long range surface plasmons with ITO microheaters. (b) The fabrication process of a sensor chip.

4.2. Bragg scattered surface plasmon microscopy: Theoretical study

A biosensor based on SPR imaging (SPRi) which is also referred to as SPR microscopy (schematically shown in Fig.4.8 a) technique has attracted great attentions due to its ability for rapid and parallel detection of multiple target analytes. In this study, a new approach to SPRi is presented which provides high refractive index sensitivity and spatial resolution that is not limited by the propagation length of SPs. It is based on non-propagating Bragg scattered surface plasmon mode which can be excited on the surface of sub-wavelength metallic gratings. Theoretical studies are carried out by using numerical simulations in order to investigate refractive index sensitivity and spatial resolution of SPR images proved by propagating SPs and BSSPs, respectively. The presented simulations predict that this approach exhibits about 2-times lower refractive index sensitivity than that obtained with regular SPs when it is applied for the observation of large dielectric features with lateral size above 10 μm. However, the improved spatial resolution, contrast and fidelity of the images are obtained by using BSSPs for the observation of smaller features with lateral size < 10 μm. Fig. 4.8b shows an example of simulated reflectivity profiles probing a dielectric step by propagating SPs and BSSPs, respectively. In addition, the simulated reflectivity profiles probed by BSSPs exhibits lower crosstalk between neighboring sensing spots. This fact opens a way for observation of denser

microarrays and thus enhancing throughput of the analysis which is important for the label-free readout of biomolecular interactions in microarray format. Furthermore, the smaller sensitivity of the excitation of BSSPs to changes in the angle of incidence holds potential for simplified instrumentation of SPR microscopy. Future efforts will be devoted to the implementation of the BSSP-based SPR microscopy that can be straightforwardly utilized by using nano-imprint lithography (NIL) for the fabrication of a sensor chip which can be directly used with regular instruments for SPR microscopy.

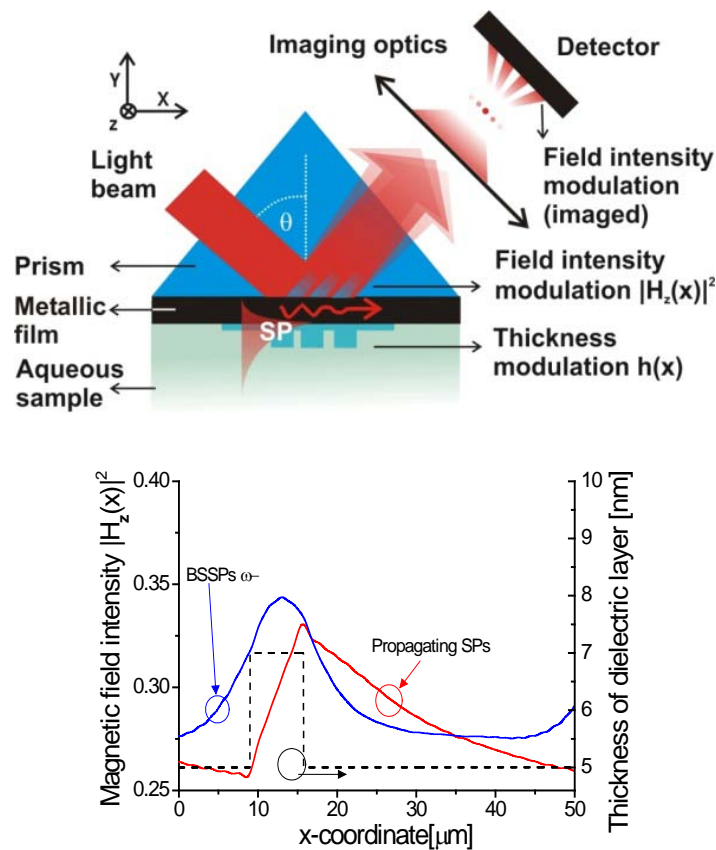Fig. 4.8 (a) Schematic of SPR microscopy. (b) Reflected magnetic field intensity profiles for probing dielectric step with a width of 6 μm and height of 2 nm, probed by propagating SPs (in red line) and BSSPs (in blue line).

This work was published to peer-reviewed journal paper as:

M. Toma, W. Knoll and J. Dostalek, "Bragg-scattered surface plasmon microscopy: Theoretical study," Plasmonics **7**, 293-299 (2012).

4.3. Directional control of surface plasmon coupled emission by Bragg-gratings

The altered dispersion relations of Surface plasmons on Bragg-gratings were employed to control the emission direction of surface plasmon coupled emission (SPCE). In this work, the directional fluorescence emission from fluorophores in the vicinity of a dense sub-wavelength metallic grating was observed by using the reverse Kretschmann configuration as shown in Fig.4.9a. This metallic grating supports Bragg-scattered surface plasmons and grating coupling surface plasmons at outer and inner interfaces, respectively. The experimental observation revealed that these plasmon modes can provide efficient fluorescence decay channels of fluorophores on the top of the metallic grating. The dispersion relation of these surface plasmon modes can be simply controlled by the refractive index at upper and lower interfaces of a metallic grating. The manipulation of the dispersion relation of SPs enables selective reducing or increasing the intensity of the fluorescence light emitted to certain directions, see Fig.4.10a-b. These features can provide means for controlling the interaction of emitters with surface plasmons which may lead to advance plasmon-enhanced fluorescence sensors through simpler and more efficient collection of fluorescence light emitted via Bragg-scattered surface plasmons. In addition, they hold potential for multiple detections by manipulating the emission direction of fluorescence light from different sensing spots to different directions.
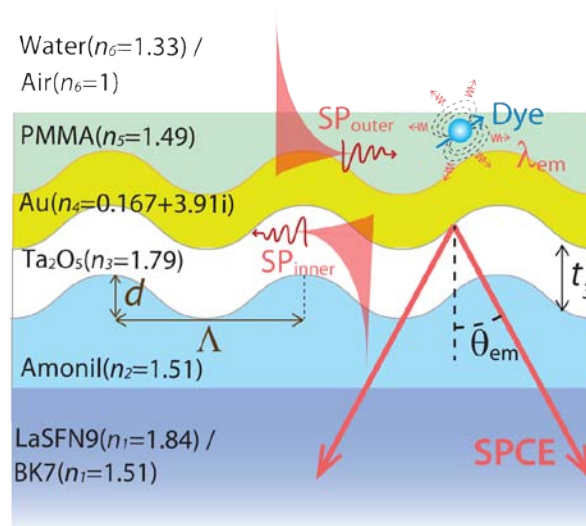

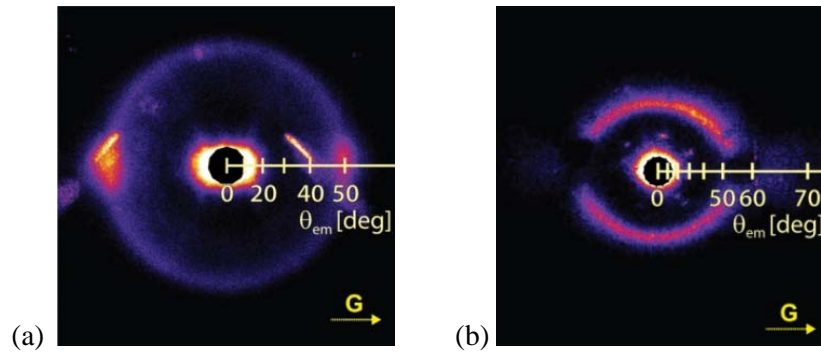Fig. 4.9 Schematic of the Bragg grating supporting surface plasmons

Fig. 4.10 (a) The spatial distribution of fluorescence emission coupled to BSSPs ω- mode. (b) the emission in to the parallel direction to grating vector is suppressed by a bandgap originated from anti-cross coupling between SP_{outer} and $G-SP_{inner.}$

This work was published to peer-reviewed journal paper as:

4.4. Active plasmonic biosensor schemes with thermo-responsive hydrogel binding matrix

A new approach for rapid actuating of surface plasmon resonance (SPR) is investigated by utilizing thermo-responsive NIPAAm-based hydrogel attached to an SPR-active sensor chip embedding ITO micro-heaters. It is based on the dramatic refractive index change of the hydrogel (as large as 0.1 RIU) at the lower critical solution temperature (LCST=33 ℃) accompanied with the decrease of the thickness, see Fig.4.11. The time evolution measurement is carried out for observing the swelling and collapsing of the hydrogel film upon the flow of the electric current to ITO microheater. The results reveal that the hydrogel film responds to a temperature stimulus faster than 100 ms, the swelling and collapsing is reversible over several hundred cycles. The presented approach is particularly suited for biosensor applications as the hydrogel network can simultaneously serve as a large binding capacity matrix for the specific capture of molecular analytes as well as optical waveguide supporting layer. This functionality is demonstrated in a biosensor experiment based on the hydrogel optical waveguide-enhanced fluorescence for detecting of fluorophore-labeled anti-mouse IgG. The actuating of hydrogel waveguide modes by collapsing and swelling of the matrix allowed switching on and off the fluorescence signal from a sensing pad. For instance, this functionality can be employed in future work for time multiplexing of sensing channels that utilizes sequential readout from spatially separated sensing spots.
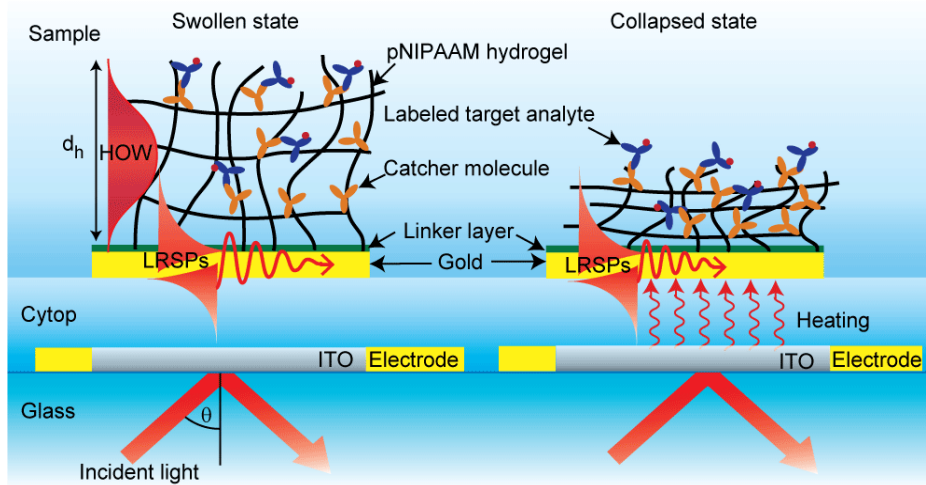
Fig. 4.11 Sensor chip supporting long range surface plasmons integrated with indium tin oxide (ITO) microheaters and thermo-responsive hydrogel film on its top. When the temperature is below the LCST, the hydrogel is highly swollen and supports HOW mode and LRSPs (the left sensor pad). When the temperature is above the LCST by applying current to ITO microheater, the hydrogel is collapsed and supports only LRSPs (the right sensor pad).

This work is in preparation for submission to peer-reviewed journal paper as:

M. Toma, U. Jonas, A. Mataescu, W. Knoll and J. Dostalek, "Active plasmonic biosensor based on thermo-responsive hydrogel," in preparation.

5. Conclusions

In this thesis, a range of novel approaches was investigated in order to advance the key performance characteristics of biosensors utilizing surface plasmon resonance and surface plasmon-enhanced fluorescence. These approaches include development of new optical platforms, investigation of new optical phenomena such as plasmonic Bragg gratings or actuating plasmonic surfaces which hold potential to improve the sensitivity and throughput of the SPR-based biosensors.

The newly developed optical setups provide rich information on SPs including dispersion relations of SPs and spatial resolved reflectivity profiles. Especially, multi-channel angular spectroscopy of hydrogel optical waveguide mode allows the improved bulk refractive index resolution which is comparable to the state-of-the-art of the SPR biosensors. The large binding capacity of the hydrogel binding matrix holds a potential for direct detection of small target analyte (with molecular weight < 5 kDa). The study of Bragg-scattered surface plasmons on dense sub-wavelength metallic gratings brings two important aspects. Firstly, the non-propagating Bragg scattered surface plasmon mode allows better fidelity and spatial resolution of SPR image compared to that of probed by propagating surface plasmons. This feature opens a way for high throughput SPR biosensors with dense array of sensing spots. Secondly, the altered dispersion relations of Bragg scattered surface plasmons are shown to be able to control the emission direction of surface plasmon mediated fluorescence emission. This fact provides means for simple and efficient collection of fluorescence signal emitted via SPCE. The implementation of thermo-responsive hydrogel binding matrix and rapid temperature control system into SPR sensor chip enables fast actuation of surface plasmons. The developed system provides a way to control resonance condition of SPR as well as HOW. This feature opens a way for multiple fluorescence detection with a simple experimental setup by tuning the fluorescence intensity of multiple sensor spots by controlling the resonance conditions.

References

1. V. P. Shah, Aaps Journal **9**, E43-E47 (2007).
2. D. R. Thevenot, K. Toth, R. A. Durst, and G. S. Wilson, Biosensors & Bioelectronics **16**, 121-131 (2001).
3. L. C. Clark, and C. Lyons, Annals of the New York Academy of Sciences **102**, 29-45 (1962).
4. T. Vo-Dinh, and B. Cullum, Fresenius Journal of Analytical Chemistry **366**, 540-551 (2000).
5. M. A. Cooper, Nature Reviews Drug Discovery **1**, 515-528 (2002).
6. O. Lazcka, F. J. Del Campo, and F. X. Munoz, Biosensors & Bioelectronics **22**, 1205-1217 (2007).
7. S. Rodriguez-Mozaz, M. J. L. de Alda, and D. Barcelo, Analytical and Bioanalytical Chemistry **386**, 1025-1041 (2006).
8. B. M. Paddle, Biosensors & Bioelectronics **11**, 1079-1113 (1996).
9. "Biacore," http://www.biacore.com/lifesciences/index.html.
10. "Biosensors - A global market overview," (2012), p. 251.
11. A. P. F. Turner, Science **290**, 1315-1317 (2000).
12. J. P. Chambers, B. P. Arulanandam, L. L. Matta, A. Weis, and J. J. Valdes, Current Issues in Molecular Biology **10**, 1-12 (2008).
13. X. Fan, I. M. White, S. I. Shopova, H. Zhu, J. D. Suter, and Y. Sun, Analytica Chimica Acta **620**, 8-26 (2008).
14. J. Dostalek, and W. Knoll, Biointerphases **3**, FD12-FD22 (2008).
15. M. Piliarik, L. Parova, and J. Homola, Biosensors & Bioelectronics **24**, 1399-1404 (2009).
16. R. Slavik, and J. Homola, Sensors and Actuators B: Chemical **123**, 10-12 (2007).
17. T. Liebermann, and W. Knoll, Colloids and Surfaces A: Physicochemical and Engineering Aspects **171**, 115-130 (2000).
18. C. Genet, and T. W. Ebbesen, Nature **445**, 39-46 (2007).
19. W. L. Barnes, A. Dereux, and T. W. Ebbesen, Nature **424**, 824-830 (2003).
20. V. K. S. Hsiao, Y. B. Zheng, B. K. Juluri, and T. J. Huang, Advanced Materials **20**, 3528-3532 (2008).
21. H.-S. Chen, J.-Y. Wang, S.-S. Yeh, C.-D. Chen, and H.-Y. Lin, Applied Physics Letters **100**, 011102-011102-011103.
22. H. Gehan, C. Mangeney, J. Aubard, G. Levi, A. Hohenau, J. R. Krenn, E. Lacaze, and N. Felidj, Journal of Physical Chemistry Letters **2**, 926-931.
23. J. Dostalek, P. Adam, P. Kvasnicka, O. Telezhnikova, and J. Homola, Optics Letters **32**, 2903-2905 (2007).
24. N. C. Lindquist, A. Lesuffleur, H. Im, and S. H. Oh, Lab on a Chip **9**, 382-387 (2009).
25. H. Raether, *Surface plasmons on smooth and rough surfaces and on gratings* (Springer-Verlag, Berlin; New York, 1988).
26. C. Kittel, *Introduction to solid state physics / Charles Kittel* (Wiley, New York :, 1976).
27. E. Kretschmann, Zeitschrift für Physik A Hadrons and Nuclei **241**, 313-324 (1971).
28. D. Sarid, Physical Review Letters **47**, 1927-1930 (1981).
29. W. Knoll, Annu. Rev. Phys. Chem. **49**, 569-638 (1998).
30. W. L. Barnes, T. W. Preist, S. C. Kitson, J. R. Sambles, N. K. Cotter, and D. J. Nash, Physical Review B **51**, 11164 (1995).
31. T. Okamoto, J. Simonen, and S. Kawata, Physical Review B **77** (2008).
32. W. L. Barnes, T. W. Preist, S. C. Kitson, and J. R. Sambles, Physical Review B **54**, 6227-6244 (1996).
33. J. R. Lakowicz, J. Malicka, I. Gryczynski, and Z. Gryczynski, Biochemical and Biophysical Research Communications **307**, 435-439 (2003).
34. P. Andrew, and W. L. Barnes, Physical Review B **64** (2001).
35. Y. M. Yu, C. L. Feng, A. M. Caminade, J. P. Majoral, and W. Knoll, Langmuir **25**, 13680-13684 (2009).

36. C. Huber, J. Liu, E. M. Egelseer, D. Moll, W. Knoll, U. B. Sleytr, and M. Sara, Small **2**, 142-150 (2006).

37. A. Lundquist, S. r. B. Hansen, H. NordstrÃ¶m, U. H. Danielson, and K. Edwards, Anal. Biochem. **405**, 153-159.

38. A. Aulasevich, R. F. Roskamp, U. Jonas, B. Menges, J. Dostálek, and W. Knoll, Macromolecular Rapid Communications **30**, 872-877 (2009).

39. W. Knoll, M. Liley, D. Piscevic, J. r. Spinke, and M. J. Tarlov, Advances in Biophysics **34**, 231-251 (1997).

40. J. C. Love, L. A. Estroff, J. K. Kriebel, R. G. Nuzzo, and G. M. Whitesides, Chemical Reviews **105**, 1103-1169 (2005).

41. Y. Wang, J. Dostálek, and W. Knoll, Biosensors and Bioelectronics **24**, 2264-2267 (2009).

42. Y. Wang, A. Brunsen, U. Jonas, J. Dostalek, and W. Knoll, Analytical Chemistry **81**, 9625-9632 (2009).

43. C. J. Huang, J. Dostalek, and W. Knoll, Biosensors and Bioelectronics **26**, 1425-1431 (2010).

44. A. Kumar, A. Srivastava, I. Y. Galaev, and B. Mattiasson, Progress in Polymer Science **32**, 1205-1237 (2007).

45. P. W. Beines, I. Klosterkamp, B. Menges, U. Jonas, and W. Knoll, Langmuir **23**, 2231-2238 (2007).

46. Y. Wang, C.-J. Huang, U. Jonas, T. Wei, J. Dostalek, and W. Knoll, Biosensors and Bioelectronics **25**, 1663-1668 (2009).

47. J. Homola, Chemical Reviews **108**, 462-493 (2008).

48. B. Liedberg, C. Nylander, and I. LunstrÃ¶m, Sensors and Actuators **4**, 299-304 (1983).

49. J. Homola, J. Dostalek, S. Chen, A. Rasooly, S. Jiang, and S. S. Yee, International Journal of Food Microbiology **75**, 61-69 (2002).

50. S. Shen, T. Liu, and J. Guo, Appl. Opt. **37**, 1747-1751 (1998).

51. T. Tumolo, L. Angnes, and M. S. Baptista, Anal. Biochem. **333**, 273-279 (2004).

52. M. Piliarik, H. Vaisocherova, and J. Homola, Biosensors & Bioelectronics **20**, 2104-2110 (2005).

53. H. J. Lee, T. T. Goodrich, and R. M. Corn, Analytical Chemistry **73**, 5525-5531 (2001).

54. B. Rothenhausler, and W. Knoll, Nature **332**, 615-617 (1988).

55. K. Toma, J. Dostalek, and W. Knoll, Optics Express **19**, 11090-11099.

56. J. Dostalek, A. Kasry, and W. Knoll, Plasmonics **2**, 97-106 (2007).

57. J. Homola, *Surface Plasmon Resonance Based Sensors* (Springer-Verlag, Berlin-Heidelberg-New York, 2006).

58. L. A. Lyon, M. D. Musick, and M. J. Natan, Analytical Chemistry **70**, 5177-5183 (1998).

59. D. R. Shankaran, K. V. A. Gobi, and N. Miura, Sensors and Actuators B-Chemical **121**, 158-177 (2007).

60. J. S. Yuk, M. Trnavsky, C. McDonagh, and B. D. MacCraith, Biosensors & Bioelectronics **25**, 1344-1349.

61. J. S. Yuk, B. D. MacCraith, and C. McDonagh, Biosensors and Bioelectronics **26**, 3213-3218.

62. E. A. Smith, and R. M. Corn, Applied Spectroscopy **57**, 320A-332A (2003).

63. K. Tamada, F. Nakamura, M. Ito, X. Li, and A. Baba, Plasmonics **2**, 185-191 (2007).

64. J. M. Brockman, B. P. Nelson, and R. M. Corn, Annu. Rev. Phys. Chem. **51**, 41-63 (2000).

65. K. Tawa, H. Hori, K. Kintaka, K. Kiyosue, Y. Tatsu, and J. Nishii, Optics Express **16**, 9781-9790 (2008).

66. C. Boozer, G. Kim, S. Cong, H. Guan, and T. Londergan, Current Opinion in Biotechnology **17**, 400-405 (2006).

67. K. F. Giebel, C. Bechinger, S. Herminghaus, M. Riedel, P. Leiderer, U. Weiland, and M. Bastmeyer, Biophysical Journal **76**, 509-516 (1999).

68. C. E. H. Berger, R. P. H. Kooyman, and J. Greve, Rev. Sci. Instrum. **65**, 2829-2836 (1994).

69. L. Niu, and W. Knoll, Analytical Chemistry **79**, 2695-2702 (2007).

6. Publications

Peer reviewed papers:

M. Toma, W. Knoll and J. Dostalek, "Bragg-scattered surface plasmon microscopy: Theoretical study," Plasmonics **7**, 293-299 (2012).

M. Toma[*], K. Toma[*], P. Adam, J. Homola, W. Knoll and J. Dostalek, "Surface plasmon-coupled emission on plasmonic Bragg-gratings," Optics Express **20**, 14042-14053 (2012). [*]Authors equally contributed to this work.
Also selected in The Virtual Journal for Biomedical Optics **7**, 8 (2012).

M. Toma, U. Jonas, A. Mataescu, W. Knoll and J. Dostalek, "Active plasmonic biosensor based on thermo-responsive hydrogel", Journal of Physical Chemistry C, in preparation.

Proceedings:

M. Toma, A. Mateescu, U. Jonas, W. Knoll and J. Dostalek, "Plasmonic biosensor schemes with thermo-responsive hydrogel binding matrix", Proceedings of International workshop Biophotonics 2011, Parma, Italy

Other conference papers and presentations:

M. Toma, Q. Zhang, U. Jonas, W. Knoll and J. Dostalek, "Hydrogel optical waveguide spectroscopy based biosensor for label-free detection of small molecules", Gordon research conference on biointerface science, Les Diablerets, Switzerland, May 2012 (Poster).

M. Toma, A. Mateescu, U. Jonas, W. Knoll and J. Dostalek, "Plasmon-enhanced fluorescence biosensor with active responsive hydrogel binding matrix", XI conference of optical chemical sensors and biosensors, Barcelona, Spain, April 2012 (Poster).

M. Toma, W. Knoll and J. Dostalek, "Bragg-scattered surface plasmons for high resolution SPR imaging", X conference of optical chemical sensors and biosensors, Prague, Czech republic, March 2010 (Poster).

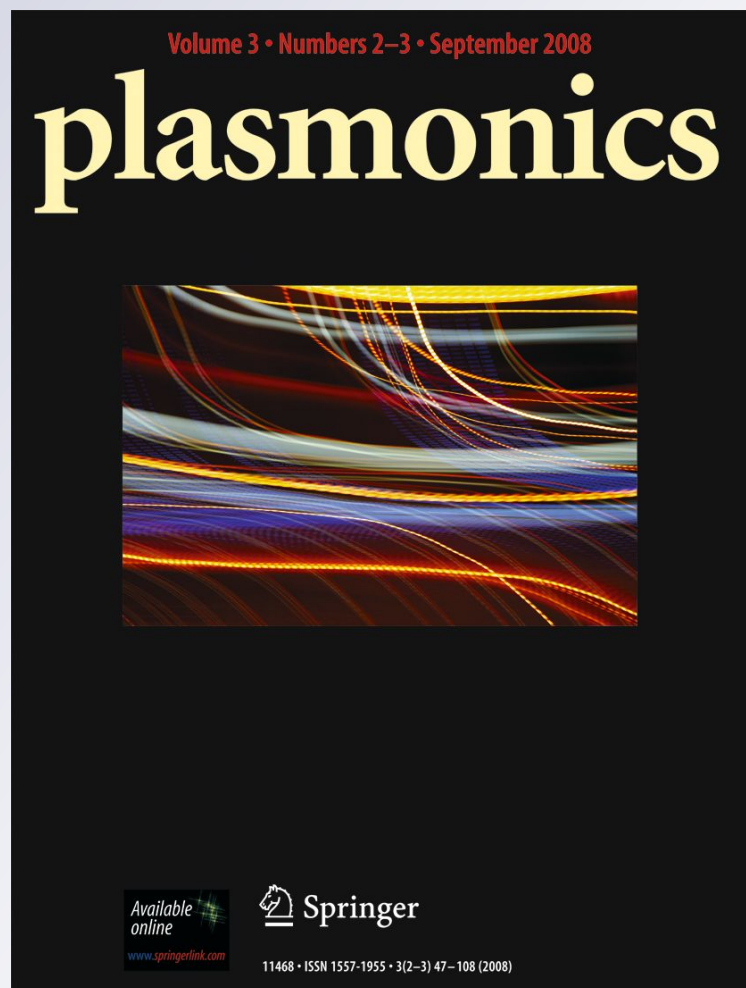# Bragg-Scattered Surface Plasmon Microscopy: Theoretical Study

Mana Toma, Wolfgang Knoll & Jakub Dostalek

Volume 3 · Numbers 2–3 · September 2008

plasmonics

Springer

Springer

Bragg-Scattered Surface Plasmon Microscopy: Theoretical Study

Mana Toma · Wolfgang Knoll · Jakub Dostalek

Abstract We present a new approach to surface plasmon microscopy with high refractive index sensitivity and spatial resolution that is not limited by the propagation length of surface plasmons. It is based on a nanostructured metallic sensor surface supporting Bragg-scattered surface plasmons. We show that these non-propagating surface plasmon modes are excellently suited for spatially resolved observations of refractive index variations on the sensor surface owing to their highly confined field profile perpendicular to as well as parallel to the metal interface. The presented theoretical study reveals that this approach enables reaching similar refractive index sensitivity as regular surface plasmon resonance (SPR) microscopy and offers the advantage of improved spatial resolution when observing dielectric features with lateral size <10 μm for the wavelength around 800 nm and gold as the SPR-active metal. This paper demonstrates the potential of Bragg-scattered surface plasmon microscopy for high-throughput SPR biosensing with high-density microarrays.

Keywords Surface plasmon resonance · SPR microscopy · SPR imaging · Diffraction grating · Biosensor

Introduction

Surface plasmon resonance (SPR) microscopy [1] that is also referred to as surface plasmon resonance imaging

M. Toma · W. Knoll · J. Dostalek (✉)
Health and Environment Department,
AIT-Austrian Institute of Technology GmbH,
Muthgasse 11,
1190 Vienna, Austria
e-mail: jakub.dostalek@ait.ac.at

becomes an established optical method for the sensitive observation of (bio)interfaces [2–5] and particularly has been used for high-throughput detection and interaction analysis of biomolecules [6–8]. In these applications, surface plasmons (SPs) are resonantly excited along a metallic sensor surface to probe a two-dimensional microarray of spots with immobilized ligands. In most common implementations, SPR microscopy utilizes the Kretschmann configuration with a prism coupler [9, 10], an optically matched microscope objective lens [11] or diffraction gratings [12] for the excitation of SPs by an optical wave incident to a metallic sensor surface. Surface plasmons exhibit an electromagnetic field that is strongly confined at the metallic interface, and they are extremely sensitive to minute changes in the refractive index associated with the binding of target biomolecules to ligands tethered at the sensor surface. These variations alter the coupling strength to surface plasmons and lead to changes in the intensity of the reflected optical wave that is subsequently imaged at a detector. Typical SPR microscopy instruments can resolve refractive index (RI) changes as small as 10^{-5} refractive index units from arrays of spots with the characteristic size from tens to several hundreds of micrometers [13]. In order to further increase the accuracy (e.g., for the observation of binding of small molecules inducing low refractive index changes) and throughput (e.g., by using denser microarrays), these characteristics need to be improved.

Up to now, various approaches exploiting phase-contrast measurements [14], wide-field excitation of SP [4, 15], and surface plasmon modes propagating along strongly absorbing metals or at low wavelengths [3, 16, 17] were investigated to advance SPR microscopy. In general, these efforts demonstrated that enhancing the spatial resolution is accompanied with deteriorating RI resolution and vice versa. The reason is that the smallest measureable refractive index change

(RI resolution) is inversely proportional to the propagation length of surface plasmons L_p, while the smallest measureable lateral size of a dielectric feature in the direction to the SP propagation (spatial resolution) is proportional to L_p [17]. This inherent limitation of SPR microscopy can be overcome by employing non-propagating localized surface plasmons (LSPs) supported by metallic nanoparticles [18]. Unfortunately, sensors based on the spectroscopy of LSPs offer significantly lower RI resolution with respect to their counterparts relying in propagating SPs due to their small figure of merit [19].

In this paper, we investigate another approach that holds potential for simultaneously advancing both RI and spatial resolution of SPR microscopy. It is based on Bragg-scattered surface plasmons (BSSPs) supported by periodically modulated metallic surface on which counterpropagating SPs are diffraction-coupled [20]. The total length that these modes travel along the surface is comparable to regular SPs on flat metallic surface which does not compromise the high RI resolution [21]. However, their lateral confinement on the surface due to the repeated Bragg scattering holds potential for improving the spatial resolution [22]. In this study, we carry out numerical simulations to investigate the key characteristics of this new approach to SPR microscopy.

Optical Configuration

In what follows, we assume SPR microscopy based on the attenuated total reflection (ATR) method in the Kretschmann configuration depicted in Fig. 1a. A transverse magnetically (TM) polarized plane wave was made incident through a high refractive index glass prism at its base with a thin gold film. The angle of incidence θ was set close to that for which resonant coupling to surface plasmons occurs at the outer interface between the gold film and a low refractive index dielectric on its top:

$$\frac{2\pi}{\lambda} n_p \sin(\theta) = \text{Re}\{\beta_{SP}\} = \frac{2\pi}{\lambda} \text{Re}\left\{\left(\frac{n_{Au}^2 n_w^2}{n_{Au}^2 + n_w^2}\right)^{1/2}\right\}, \qquad (1)$$

where λ is the wavelength, n_p is the refractive index of the prism, n_{Au} is the refractive index of the gold film, and n_w is the refractive index of the low refractive index dielectric. β_{SP} is a (complex) propagation constant of SP at an interface between a semi-infinite metal and a low refractive index dielectric. Re {} denotes the real part of a complex number. In further simulations, Cartesian coordinates were used with the x-axis lying parallel to the surface and in the plane of incidence, the y-axis perpendicular to the plane of incidence, and the z-axis perpendicular surface. The prism refractive
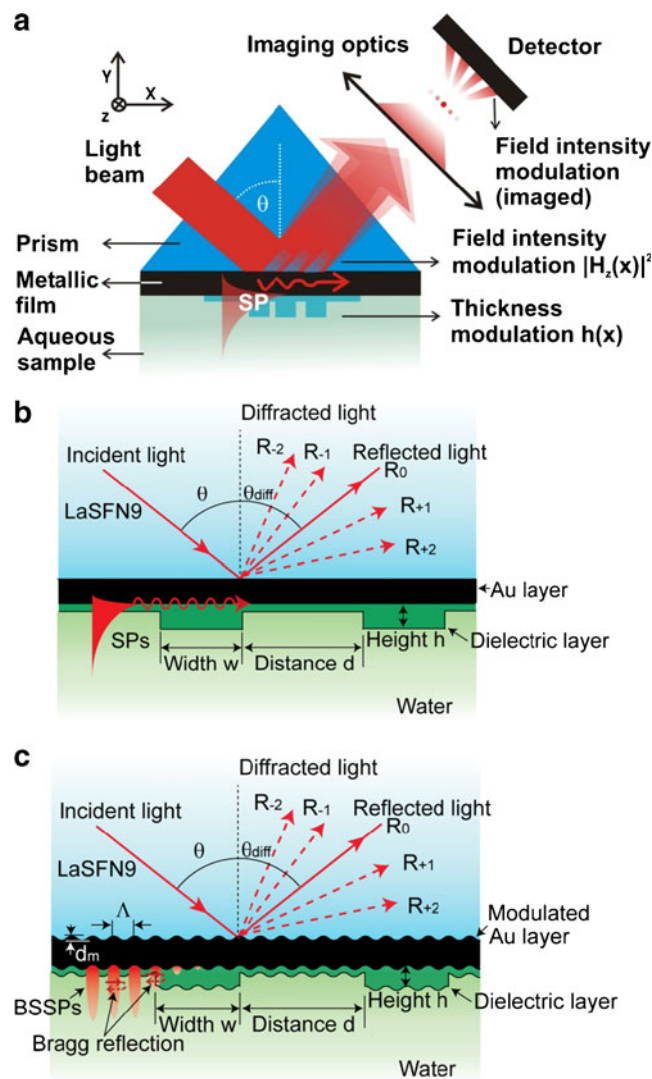
Fig. 1 **a** Schematics of the implementation of SPR microscopy based on ATR method with Kretschmann configuration utilizing **b** flat metallic film supporting regular surface plasmons and **c** periodically modulated metallic film supporting Bragg-scattered surface plasmons

index n_p was that of LaSFN9 glass [23]. A SPR-active gold film with the thickness of 50 nm and a refractive index n_{Au} taken from literature [24] was used. A dielectric film with a refractive index n_f=1.5 that is close to that of biomolecules [25] was attached on the gold surface, and its varied thickness $h(x)$ represented an object being imaged (e.g., an array of spots). The surface was brought in contact with semi-infinite aqueous medium with a refractive index of water n_w [26]. The gold film was assumed to be flat (for the excitation of regular SP, Fig. 1b) or with a sinusoidal relief modulation in the x direction with a periodicity of Λ= 280 nm and depth d_m=20 nm (for the excitation of BSSP, Fig. 1c).

The period of the modulation Λ was set to induce Bragg scattering of SP wave between wavelengths λ=750 and

800 nm. This period was obtained analytically from diffraction coupling condition (2):

$$\frac{2\pi}{\Lambda} = 2\mathrm{Re}\{\beta_{\mathrm{SP}}\} = \frac{4\pi}{\lambda}\mathrm{Re}\left\{\left(\frac{n_{\mathrm{Au}}^2 n_{\mathrm{w}}^2}{n_{\mathrm{Au}}^2 + n_{\mathrm{w}}^2}\right)^{1/2}\right\}. \qquad (2)$$

As an object, a dielectric film with a periodically modulated height along the surface $h(x)$ was assumed in the following form:

$$h(x) = h_0 + \Delta h \sum_{n=-\infty}^{\infty} \vartheta(x + nL)\vartheta(w - x - nL), \qquad (3)$$

where ϑ is a Heaviside step function, Δh is the height of a dielectric step, w is the lateral width of the dielectric step, L is the period, and n is an integer. Without the loss of generality, a thickness of the homogenous dielectric film of $h_0=5$ nm was chosen for the sake of improved convergence of the numerical model introduced in the next section. The dielectric layer thickness is varied only in one dimension that is parallel to the propagation of SP modes, and the characteristics of the imaging optics were omitted for simplicity.

Theoretical Model

The reflected field intensity variations along the inner metallic surface were calculated in the form of Rayleigh series for the probing of the sensor surface by regular SPs and BSSPs. As the probing optical wave was TM polarized, we calculated the changes in reflected magnetic field intensity with only non-zero component parallel to the surface H_z:

$$H_z(x) = \sum_{n=n_1}^{n_2} R_n \exp(+i\alpha_n x), \qquad (4)$$

$$\alpha_n = \frac{2\pi}{\lambda} n_{\mathrm{p}} \sin\theta + \frac{2\pi}{L} n, \qquad (5)$$

where R_n denotes the Rayleigh coefficient of the nth diffraction order. In the series (4), the sum over the diffraction orders from n_1 to n_2 was made to take into account diffraction orders propagating away from the metallic film through the glass medium at angles θ_{diff} between 0 and 90° (see Fig. 1b, c). The series of Rayleigh coefficients R_n were numerically solved by using finite element method that was implemented in a diffraction grating solver DiPoG (Weierstrass Institute, Germany). A grating in a computation cell with the length up to $L=45$ μm and height of 0.1 μm was approximated by a mesh of triangles (convergence was achieved for mesh with number of triangles larger than 40,000 for a flat gold film and 80,000 for a modulated gold

film). Let us note that for structures supporting BSSPs, the periods L and Λ were adjusted to $L = p\Lambda$ holds for certain integer p. In the used numerical model, the set of Maxwell equations was solved by using the PARDISO solver of sparse linear systems (University of Basel, Switzerland).

In order to verify the validity of the used numerical model, we compared the numerical results with those obtained from an analytical theory described by Berger et al. [17]. We calculated the reflected magnetic field intensity distribution $|H_z(x)|^2$ at an inner gold interface when regular surface plasmons propagating along a flat gold surface probe a dielectric step (with a width of $w=20$ μm, distance of $d=20$ μm, and height of $\Delta h=5$ nm). As the analytical model is based on the assumption that SPs sequentially passing through individual walls of a dielectric step do not interact, we used the wavelength of $\lambda=633$ nm at which the propagation length of SPs is much shorter than the width of the used dielectric step w. Let us note that such numerical simulations would require increasing the dielectric step width w and thus significantly higher computing power for the wavelength $\lambda=800$ nm. The propagation length of SPs on a flat surface can be analytically calculated as:

$$L_{\mathrm{p}} = \frac{1}{2\mathrm{Im}\{\beta_{\mathrm{SP}} + \Delta\beta_{\mathrm{SP}}\}}, \qquad (6)$$

and equals for the used structure to $L_{\mathrm{p}}=2.4$ and 13 μm at wavelengths $\lambda=633$ and 800 nm, respectively. Let us note that Eq. 6 takes into account the radiation losses due to the finite thickness of gold film by the additional term of $\Delta\beta_{\mathrm{SP}}$ in the denominator (details can be found in [27]).

Results in Fig. 2 reveal an excellent agreement between analytical and numerical simulations. The intensity of the reflected plane wave hitting the surface with a dielectric step at an angle of incidence $\theta_{\mathrm{inc}}=51.3°$ is modulated along the surface due to the varied coupling strength to SPs in areas
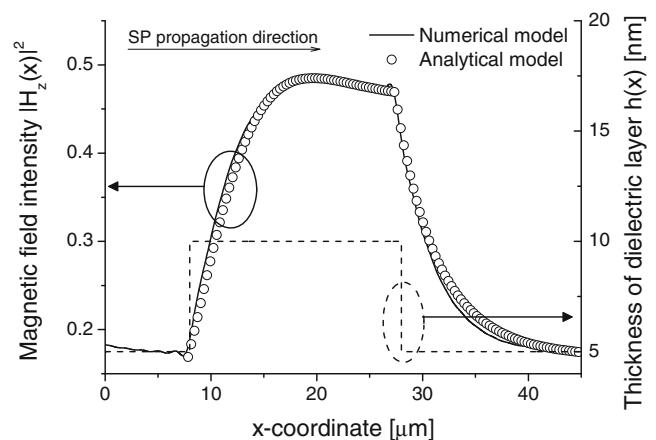

Fig. 2 Profile of the magnetic intensity $|H_z(x)|^2$ at the inner gold interface obtained by numerical and analytical models for a dielectric step at the outer gold film interface

with different thickness of the dielectric overlayer h. The changes of the field intensity distribution across dielectric step edges are not abrupt. The data show that the reflected field intensity $|H_z(x)|^2$ gradually increases and decreases when SP passes through the edge into the dielectric ($x=8$ μm) or out of the dielectric overlayer ($x=28$ μm), respectively. The exponentially saturating increase is slightly modulated due to the interference of SPs propagating into the dielectric through the edge at $x=8$ μm and SPs that are excited through the metal at $x>8$ μm. This interference originates from the shift of the propagating constant β_{SP} due to variations of the dielectric layer thickness [28]. The field intensity exponentially decreases after SPs pass into water through the edge at $x=28$ μm with a decay constant $1/L_p=0.49$ μm^{-1} which agrees with the propagation length calculated from Eq. 6.

Results and Discussion

Bragg-Scattered and Regular Surface Plasmons

In further simulations, we used a wavelength $\lambda\sim800$ nm which was reported to provide the highest RI refractive index resolution in SPR biosensors with a flat gold film [29]. Firstly, dispersion relations of regular and Bragg-scattered surface plasmon modes were studied in vicinity to this wavelength by simulating the dependence of the reflectivity $|R_0|^2$ on the wavelength λ and the angle of incidence θ. Figure 3 shows the obtained reflectivity for (a) flat gold film supporting regular SPs and (b) for periodically modulated gold thin film supporting BSSPs. The gold surface was not covered with the dielectric layer $h_0=\Delta h=0$, and it was interfaced with a semi-infinite water medium. In the case of the flat gold film, regular SPs' dispersion is observed as a reflectivity drop located at angle θ that decreases from $\theta=50°$ to $48.5°$ when increasing the

wavelength from $\lambda=700$ to 850 nm. These data are in accordance with the phase-matching condition (1).

For the modulated gold film, one can see a gap in the dispersion relation occurring at the wavelength band $\lambda=756$–802 nm, where SPs cease propagating due to the Bragg reflections on the grating. At edges of the band gap, two new Bragg-scattered surface plasmon modes appear that are referred to as ω^+ (at $\lambda=756$ nm) and ω^- (at $\lambda=802$ nm) modes. The dispersion relation of BSSPs in Fig. 3 reveals that the spectral positions of these resonances are weakly dependent on the angle of incidence θ which is characteristic for non-propagating (localized) surface plasmon modes. These modes exhibit standing wave properties, and their electromagnetic field is concentrated either at the peaks (ω^-) or valleys (ω^+) of the metal layer relief modulation [20]. This phenomenon is illustrated in Fig. 4 which compares the profile of the electromagnetic field intensity through the layer structure for (a) regular SP, (b) BSSP ω^+, and (c) BSSP ω^-.

SPR Microscopy with Bragg-Scattered and Regular Surface Plasmons

In order to investigate key characteristics of SPR microscopy with regular and Bragg-scattered SPs, we carried out series of simulations of the optical response upon probing minute changes in the dielectric thin film thickness $h(x)$. We calculated the reflected magnetic field intensity distribution $|H_z(x)|^2$ at the inner gold interface and related the observed features to the height Δh, width w, and distance d between dielectric rectangular steps defined by Eq. 3. Regular SPs were excited by a plane wave with a wavelength of $\lambda=800$ nm that was made incident on the gold surface under an angle $\theta=48.7°$. BSSPs ω^- are excited by a plane wave with almost identical wavelength of $\lambda=802$ nm at an angle of incidence $\theta=51°$. The ω^- was chosen as its excitation provides a field more confined to the metallic surface than

Fig. 3 Dispersion relation of surface plasmons propagating along **a** flat and **b** periodically modulated gold film in contact with water at the outer interface. The relief modulation of metallic film with the period of $\Lambda=280$ nm and depth of $d_m=20$ nm were assumed
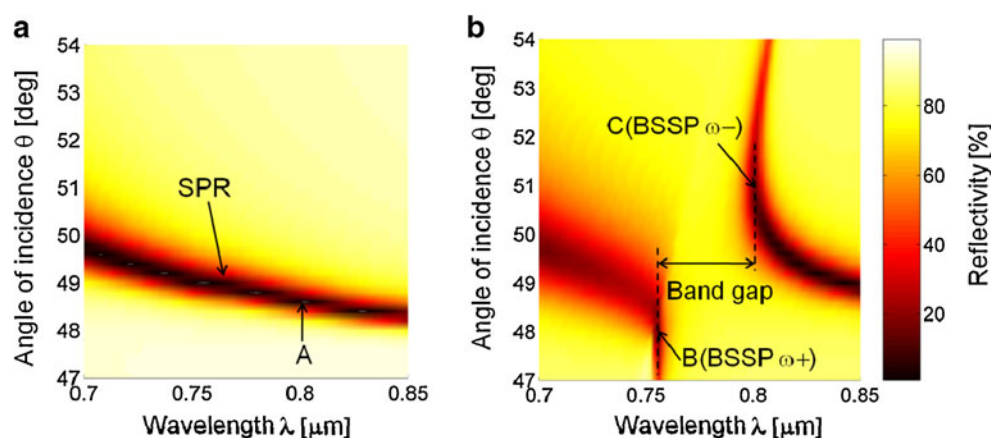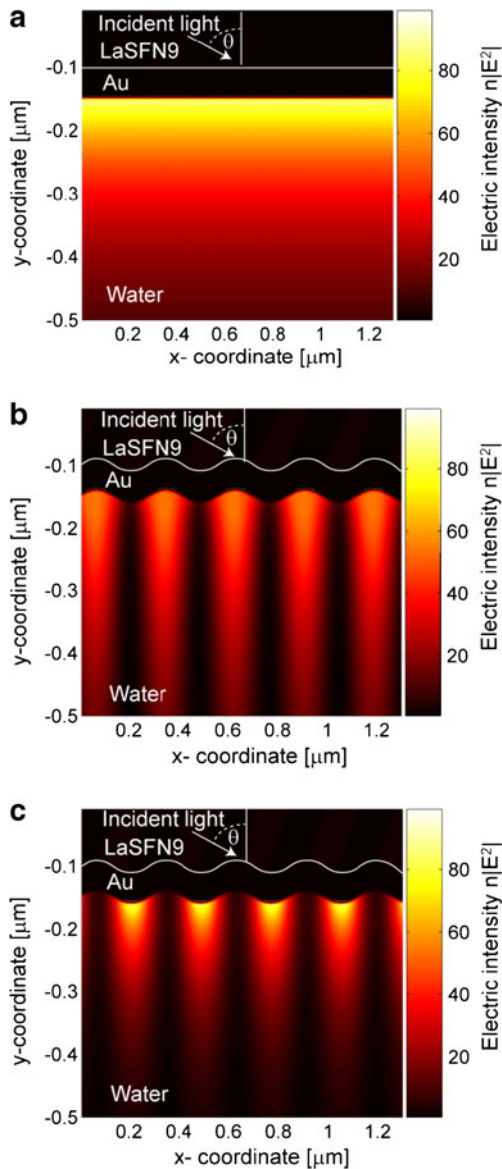
Fig. 4 Profile of field intensity at the outer gold surface for **a** regular SPs (*point A* in Fig. 3) and **b** ω^+ mode (*point B* in Fig. 3) and **c** ω^- mode (*point C* in Fig. 3) BSSPs

the ω^+ mode, see Fig. 3b, c. SP and BSSP ω^- modes were strongly excited at the gold surface with lower thickness $h(x)=h_0$ and weakly excited at areas with high thickness of a dielectric layer $h(x)=h_0+\Delta h$. The reason is that the resonant wavelength of regular SP and BSSP modes is red shifted when increasing the refractive index, and the coupling to these modes becomes detuned. Additionally, BSSP ω^- moves into the band gap in the area covered with dielectric step $(h(x)=h_0+\Delta h)$ in which SPs become strongly reflected on the grating.

The reflected magnetic field intensity $|H_z(x)|^2$ was firstly calculated for an array of dielectric rectangular steps with heights $\Delta h=1$, 2, and 3 nm, respectively, and with fixed

width $w=20$ μm, distance $d=25$ μm, and computing period $L=45$ μm ($L=w+d$). As seen in Fig. 5a, for regular SPs, the magnetic field intensity distribution $|H_z(x)|^2$ exhibits a sawtooth profile with its minimum at the edge where SPs pass into the dielectric ($x=9$ μm) and its maximum at the edge where SPs pass from the dielectric ($x=29$ μm). As the height of the dielectric step Δh increases, both maximum and the minimum field intensities increase. These smearing effects are due to the small distance d and width w that are comparable to the propagation length L_p. Contrary to that, Fig. 5b shows that for the probing by BSSPs, the magnetic field intensity $|H_z(x)|^2$ reaches its maximum in the vicinity to the center of the dielectric step and exponentially decays to both sides away from the step. The maximum magnetic field intensity change $\Delta|H_z|^2$ linearly increases with the step height Δh, and the slope $\Delta|H_z|^2/\Delta h$ is approximately two-fold higher for regular SPs than for BSSPs ω^-. This indicates that for large objects with lateral size exceeding approximately 10 μm, SPR microscopy with regular SPs
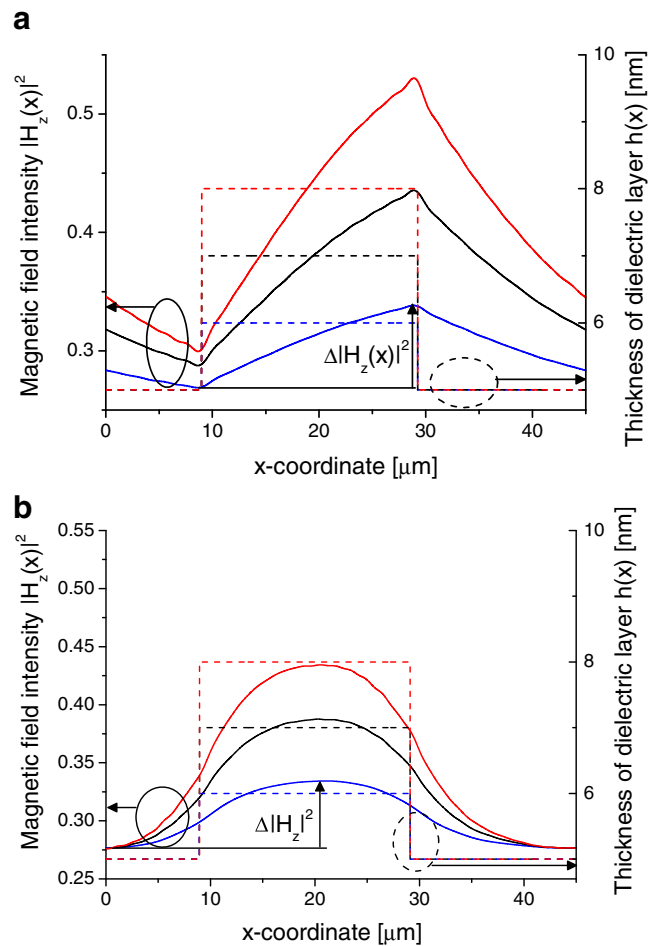

Fig. 5 The spatial dependence of reflected magnetic field intensity at the inner metal interface $|H_z(x)|^2$ on the height of the dielectric step for the structure supporting **a** regular SPs and **b** BSSPs ω^-

provides better refractive index sensitivity than that with BSSPs.

Afterwards, the dependence of the reflected magnetic intensity field distribution $|H_z(x)|^2$ on the width of a dielectric step ($w=6.7$, 11.2, and 20.2 µm) was calculated for a constant height $\Delta h=2$ nm and computing period $L=45$ µm. Figure 6 reveals that as the step width decreases, the width of associated feature in $|H_z(x)|^2$ also decreases. For the probing with regular SPs, the maximum field intensity change $\Delta|H_z|^2$ rapidly decreases when decreasing the dielectric step width w, and the distribution of $|H_z(x)|^2$ is asymmetrical with a slowly decreasing tail after the SP field passes through the edge from the dielectric to the water medium, see Fig. 6a. Contrary to these observations, Fig. 6b shows that $\Delta|H_z|^2$ is less dependent on the width step w when probed by BSSPs. In addition, the probing with BSSPs enables resolving small dielectric layer steps (with $w<6$ µm) with higher contrast (due to the higher maximum field intensity change $\Delta|H_z|^2$) than regular SPs. For such small dielectric features, the SPR microscopy with BSSPs takes clear advantage of the stronger lateral localization of the probing field. This can be quantified by the distance L_d between the maximum magnetic intensity field $|H_z(x)|^2$ and the position where $|H_z(x)|^2$ reaches half of its maximum. For BSSPs, L_d is approximately twice smaller ($L_d=5.4$ µm) than for regular SPs ($L_d=10.3$ µm).

Finally, the optical response was evaluated when two identical dielectric steps separated by different distances ($d=9$, 18, and 40.5 µm) were probed by regular SP and BSSP ω^-. The results presented in Fig. 7 were calculated for the width of steps of $w=4.5$ µm, height $\Delta h=2$ nm, and computation period $L=45$ µm. For regular SPs probing two dielectric steps brought in close proximity, the maximum intensities of the two associated peaks in $|H_z(x)|^2$ are significantly changed as the distance between neighboring steps gets closer. Contrary to these observations, the peaks in the magnetic field distribution $|H_z(x)|^2$ change negligibly for steps that are located at any distance from 9 to 40.5 µm when probed by BSSPs. This indicates that a strong cross

Fig. 6 The spatial dependence of reflected magnetic field intensity at the inner metal interface $|H_z(x)|^2$ on the width w of the dielectric step for the structure supporting **a** regular SPs and **b** BSSPs ω^-

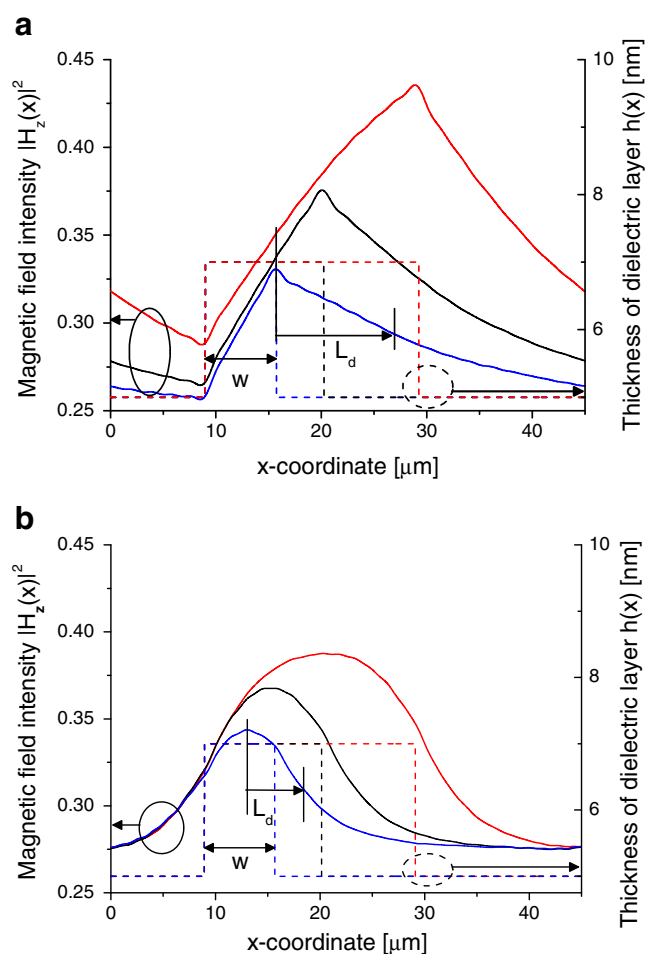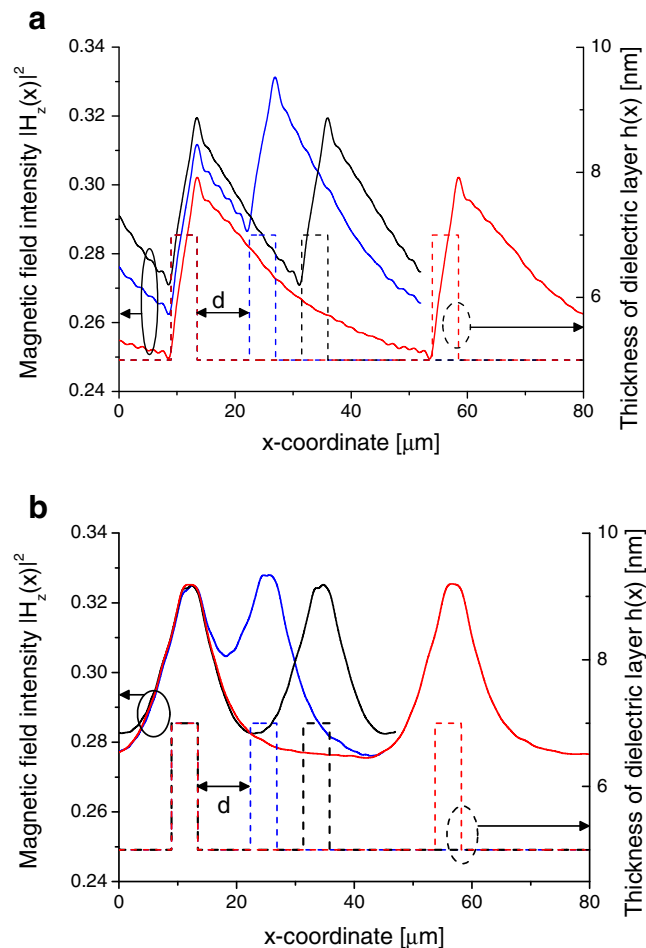**Fig. 7** The spatial dependence of reflected magnetic field intensity at the inner metal interface $|H_z(x)|^2$ on the distance between two neighboring steps in the dielectric film d upon probing by **a** regular SPs and **b** BSSPs ω^-

talk between neighboring sensing spots can be efficiently removed by using BSSP modes.

Conclusions

In this study, we introduced a finite element-based model for the investigation of spatial and refractive index resolution of SPR microscopy with flat and nano-structured metallic surfaces. In particular, we investigated the employment of densely periodically modulated gold surface supporting non-propagating Bragg-scattered surface plasmons for probing minute variations in the thickness of thin dielectric film. The presented simulations predict that this approach exhibits about two times lower refractive index resolution as regular SP microscopy when applied for the observation of large dielectric features with lateral size above 10 μm. However, for the observation of smaller features with lateral size <10 μm, we achieved an improved spatial resolution, contrast, and fidelity of the images by using BSSPs. For instance, when applied to the label-free readout of biomolecular interactions in microarray format, lower cross talk between neighboring spots will enable developing denser microarrays and thus enhancing throughput of the analysis. In addition, the smaller sensitivity of the excitation of BSSPs to changes in the angle of incidence holds potential for simplified instrumentation of SPR microscopy. Future efforts will be devoted to the implementation of the BSSP-based SPR microscopy that can be straightforwardly utilized by using nanoimprint lithography for the fabrication of a sensor chip which can be directly used with regular instruments for SPR microscopy.

References

1. Rothenhäusler B, Knoll W (1988) Surface–plasmon microscopy. Nature 332:615–617
2. Wang ZZ, Wilkop T, Han JH, Dong Y, Linman MJ, Cheng Q (2008) Development of air-stable, supported membrane arrays with photolithography for study of phosphoinositide–protein interactions using surface plasmon resonance imaging. Anal Chem 80:6397–6404
3. Giebel KF, Bechinger C, Herminghaus S et al (1999) Imaging of cell/substrate contacts of living cells with surface plasmon resonance microscopy. Biophys J 76:509–516
4. Jamil MMA, Denyer MCT, Youseffi M et al (2008) Imaging of the cell surface interface using objective coupled widefield surface plasmon microscopy. J Struct Biol 164:75–80
5. Scarano S, Mascini M, Turner APF, Minunni M (2010) Surface plasmon resonance imaging for affinity-based biosensors. Biosens Bioelectron 25:957–966
6. Smith EA, Corn RM (2003) Surface plasmon resonance imaging as a tool to monitor biomolecular interactions in an array based format. Appl Spectrosc 57:320–332
7. Boozer C, Kim G, Cong SX, Guan HW, Londergan T (2006) Looking towards label-free biomolecular interaction analysis in a high-throughput format: a review of new surface plasmon resonance technologies. Curr Opin Biotechnol 17:400–405
8. Lee HJ, Goodrich TT, Corn RM (2001) SPR imaging measurements of 1-D and 2-D DNA microarrays created from microfluidic channels on gold thin films. Anal Chem 73:5525–5531
9. Shumaker-Parry JS, Cambell CT (2004) Anal Chem 76:907–917
10. Johansen K (2005) Imaging SPR apparatus. US Patent 6862094
11. Huang B, Yu F, Zare RN (2007) Surface plasmon resonance imaging using a high numerical aperture microscope objective. Anal Chem 79:2979–2983
12. Singh BK, Hillier AC (2006) Surface plasmon resonance imaging of biomolecular interactions on a grating-based sensor array. Anal Chem 78:2009–2018
13. Yeatman EM (1996) Resolution and sensitivity in surface plasmon microscopy and sensing. Biosens Bioelectron 11:635–649
14. Piliarik M, Vaisocherova H, Homola J (2005) A new surface plasmon resonance sensor for high-throughput screening applications. Biosens Bioelectron 20:2104–2110
15. Stabler G, Somekh MG, See CW (2004) High-resolution widefield surface plasmon microscopy. J Microsc-Oxf 214:328–333
16. Wark AW, Lee HJ, Corn RM (2005) Long-range surface plasmon resonance imaging for bioaffinity sensors. Anal Chem 77:3904–3907
17. Berger CEH, Kooyman RPH, Greve J (1994) Resolution in surface-plasmon microscopy. Rev Sci Instrum 65:2829–2836
18. Stewart ME, Mack NH, Malyarchuk V et al (2006) Quantitative multispectral biosensing and 1D imaging using quasi-3D plasmonic crystals. PNAS 103:17143–17148
19. Kvasnicka P, Homola J (2008) Optical sensors based on spectroscopy of localized surface plasmons on metallic nanoparticles: sensitivity considerations. Biointerphases 3:FD4–FD11
20. Barnes WL, Preist TW, Kitson SC, Sambles JR, Cotter NK, Nash DJ (1995) Photonic gaps in the dispersion of surface plasmons on gratings. Physical Rev B 51:11164–11168
21. Dostalek J, Adam P, Kvasnicka P, Telezhnikova O, Homola J (2007) Spectroscopy of Bragg-scattered surface plasmons for characterization of thin biomolecular films. Opt Lett 32:2903–2905
22. Lindquist NC, Lesuffleur A, Im H, Oh SH (2009) Sub-micron resolution surface plasmon resonance imaging enabled by nanohole arrays with surrounding Bragg mirrors for enhanced sensitivity and isolation. Lab on a Chip 9:382–387
23. SCHOTT AG (2011) Optical Glass Data Sheets, Germany
24. Homola J (2006) Surface plasmon resonance based sensors. Springer, Berlin
25. Voros J (2004) The density and refractive index of adsorbing protein layers. Biophys J 87:553–561
26. Palik ED (1998) Handbook of optical constants of solids. Elsevier, New York
27. Kretschmann E (1971) Die bestimmung optischer konstanten von metallen durch anregung von oberflächenplasmaschwingungen. Zeitschrift für Physik A Hadrons Nuclei 241:313–324
28. Rothenhausler B, Knoll W (1988) Surface plasmon interferometry in the visible. Appl Phys Lett 52:1554–1556
29. Piliarik M, Homola J (2009) Surface plasmon resonance (SPR) sensors: approaching their limits? Opt Express 17:16505–16517

Surface plasmon-coupled emission on plasmonic Bragg gratings

Mana Toma,[1,3] Koji Toma,[1,3] Pavel Adam,[2] Jiří Homola,[2] Wolfgang Knoll,[1] and Jakub Dostálek[1,*]

[1] *AIT - Austrian Institute of Technology GmbH, Muthgasse 11, 1190 Vienna, Austria*
[2] *Institute of Photonics and Electronics, Academy of Sciences CR, Chaberská 57, 18251 Prague, Czech Republic*
[3] *These authors contributed equally to this work*
[*]jakub.dostalek@ait.ac.at

Abstract: Surface plasmon-coupled emission (SPCE) from emitters in a close proximity to a plasmonic Bragg grating is investigated. In this study, the directional fluorescence emission mediated by Bragg-scattered surface plasmons and surface plasmons diffraction cross-coupled through a thin metallic film is observed by using the reverse Kretschmann configuration. We show that controlling of dispersion relation of these surface plasmon modes by tuning the refractive index at upper and lower interfaces of a dense sub-wavelength metallic grating enables selective reducing or increasing the intensity of the light emitted to certain directions. These observations may provide important leads for design of advanced plasmonic structures in applications areas of plasmon-enhanced fluorescence spectroscopy and nanoscale optical sources.

©2012 Optical Society of America

OCIS codes: (240.6680) Surface plasmons; (300.2530) Fluorescence, laser-induced; (050.1950) Diffraction gratings; (050.6624) Subwavelength structures.

References and links

1. H. Aouani, O. Mahboub, N. Bonod, E. Devaux, E. Popov, H. Rigneault, T. W. Ebbesen, and J. Wenger, "Bright unidirectional fluorescence emission of molecules in a nanoaperture with plasmonic corrugations," Nano Lett. **11**(2), 637–644 (2011).
2. L. Novotny and N. van Hulst, "Antennas for light," Nat. Photonics **5**(2), 83–90 (2011).
3. P. A. Hobson, S. Wedge, J. A. E. Wasey, I. Sage, and W. L. Barnes, "Surface plasmon mediated emission from organic light-emitting diodes," Adv. Mater. (Deerfield Beach Fla.) **14**(19), 1393–1396 (2002).
4. S. Wedge, A. Giannattasio, and W. L. Barnes, "Surface plasmon-polariton mediated emission of light from top-emitting organic light-emitting diode type structures," Org. Electron. **8**(2-3), 136–147 (2007).
5. T. Okamoto, J. Simonen, and S. Kawata, "Plasmonic crystal for efficient energy transfer from fluorescent molecules to long-range surface plasmons," Opt. Express **17**(10), 8294–8301 (2009).
6. J. R. Lakowicz, K. Ray, M. Chowdhury, H. Szmacinski, Y. Fu, J. Zhang, and K. Nowaczyk, "Plasmon-controlled fluorescence: a new paradigm in fluorescence spectroscopy," Analyst (Lond.) **133**(10), 1308–1346 (2008).
7. J. Dostálek and W. Knoll, "Biosensors based on surface plasmon-enhanced fluorescence spectroscopy," Biointerphases **3**(3), FD12–FD22 (2008).
8. W. L. Barnes, "Fluorescence near interfaces: the role of photonic mode density," J. Mod. Opt. **45**(4), 661–699 (1998).
9. G. W. Ford and W. H. Weber, "Electromagnetic interactions of molecules with metal surfaces," Phys. Rep. **113**(4), 195–287 (1984).
10. P. Andrew and W. L. Barnes, "Molecular fluorescence above metallic gratings," Phys. Rev. B **64**(12), 125405 (2001).
11. J. R. Lakowicz, J. Malicka, I. Gryczynski, and Z. Gryczynski, "Directional surface plasmon-coupled emission: a new method for high sensitivity detection," Biochem. Biophys. Res. Commun. **307**(3), 435–439 (2003).
12. W. Knoll, M. R. Philpott, and J. D. Swalen, "Emission of Light from Ag Metal Gratings Coated with Dye Monolayer Assemblies," J. Chem. Phys. **75**(10), 4795–4799 (1981).
13. R. M. Amos and W. L. Barnes, "Modification of spontaneous emission lifetimes in the presence of corrugated metallic surfaces," Phys. Rev. B **59**(11), 7708–7714 (1999).
14. K. Tawa, H. Hori, K. Kintaka, K. Kiyosue, Y. Tatsu, and J. Nishii, "Optical microscopic observation of fluorescence enhanced by grating-coupled surface plasmon resonance," Opt. Express **16**(13), 9781–9790 (2008).

15. S. C. Kitson, W. L. Barnes, and J. R. Sambles, "Surface-Plasmon Energy Gaps and Photoluminescence," Phys. Rev. B Condens. Matter **52**(15), 11441–11445 (1995).
16. M. Kreiter, S. Mittler, W. Knoll, and J. R. Sambles, "Surface plasmon-related resonances on deep and asymmetric gold gratings," Phys. Rev. B **65**(12), 125415 (2002).
17. S. Wedge and W. L. Barnes, "Surface plasmon-polariton mediated light emission through thin metal films," Opt. Express **12**(16), 3673–3685 (2004).
18. W. H. Weber and C. F. Eagen, "Energy transfer from an excited dye molecule to the surface plasmons of an adjacent metal," Opt. Lett. **4**(8), 236–238 (1979).
19. E. Matveeva, J. Malicka, I. Gryczynski, Z. Gryczynski, and J. R. Lakowicz, "Multi-wavelength immunoassays using surface plasmon-coupled emission," Biochem. Biophys. Res. Commun. **313**(3), 721–726 (2004).
20. K. Toma, J. Dostalek, and W. Knoll, "Long range surface plasmon-coupled fluorescence emission for biosensor applications," Opt. Express **19**(12), 11090–11099 (2011).
21. Y. Wang, J. Dostalek, and W. Knoll, "Magnetic nanoparticle-enhanced biosensor based on grating-coupled surface plasmon resonance," Anal. Chem. **83**(16), 6202–6207 (2011).
22. E. Kretschmann, "Die Bestimmung optischer Konstanten von Metallen durch Anregung von Oberflächenplasmaschwingungen," Z. Phys. **241**(4), 313–324 (1971).
23. E. D. Palik, *Handbook of Optical Constants of Solids* (Elsevier, 1998).
24. W. L. Barnes, T. W. Preist, S. C. Kitson, and J. R. Sambles, "Physical origin of photonic energy gaps in the propagation of surface plasmons on gratings," Phys. Rev. B Condens. Matter **54**(9), 6227–6244 (1996).
25. F. Romanato, L. Hong, H. K. Kang, C. C. Wong, Y. Zong, and W. Knoll, "Azimuthal dispersion and energy mode condensation of grating-coupled surface plasmon polaritons," Phys. Rev. B **77**(24), 245435 (2008).

1. Introduction

Surface plasmon-coupled emission (SPCE) is of great interest in various areas including nanoscale optical antennas [1, 2], organic light-emitting diodes [3, 4], dye lasers [5] and fluorescence spectroscopy [6, 7]. Surface plasmons (SPs) are electromagnetic waves which originate from collective oscillations of charge density at metallic surfaces. SPs exhibit tightly confined field profile which is associated with greatly enhanced photonic mode density (PMD) and intensity of electromagnetic field at a metallic surface. Therefore, light radiated by emitters in the vicinity of a metal can be trapped by SPs and the coupling of absorption and emission dipoles of emitters with SPs dramatically alters their characteristics including the excitation rate, lifetime, and quantum yield [8, 9].

In order to convert energy emitted to SPs back to light waves propagating away from the metal, approaches utilizing diffraction gratings [10] and the reverse Kretschmann configuration of attenuated total reflection (ATR) method [11] were most commonly used. The employment of relief diffraction gratings for the extraction of fluorescence light from a metallic surface was firstly reported by Knoll et al. [12]. In this and later experiments, the corrugated metallic surfaces with the period comparable with the wavelength were typically used in studies including plasmon-mediated emission decay kinetics [13], angular distribution of emitted light [14], and emitted wavelength spectrum [15]. These investigations were carried out for gratings supporting regular SPs as well as coupled surface plasmon modes including Bragg-scattered surface plasmons [15, 16] and long range and short range surface plasmons on thin metallic films in refractive index symmetrical geometry [5, 17]. Relief gratings with non-sinusoidal profile allow additional control of the interaction strength between emitters and SPs through surface plasmon Bragg-scattering and associated bandgap occurring in their dispersion relation [5, 15]. The surface plasmon bandgap was shown to decrease the intensity of fluorescence light emitted via surface plasmons [15] which was, for instance, proposed for selective cancelling of spontaneous emission in plasmonic lasers [5]. In addition, Bragg-scattered surface plasmons were investigated for spatially controlled photobleaching of dyes [16]. In the other common optical platform of SPCE utilizing reverse Krestchmann configuration of ATR, a thin metal layer on a flat high refractive index substrate is used. The light emission occurs via surface plasmons that are leaky into the substrate forms a characteristic SPCE cone propagating away from the metal film [18, 19]. The polar angle of the cone is defined by the surface plasmon resonance (SPR) condition and it depends on the wavelength [19]. The width of the SPCE cone depends on the losses of surface plasmons and it can be strongly decreased by using long-range surface plasmons [20].

In this paper, we extend studies in surface plasmon-coupled emission on structures that combine the reverse Kretschmann configuration of ATR and dense sub-wavelength metallic gratings. These gratings carry a thin metallic film and are designed to alter dispersion relation of surface plasmon modes by Bragg-scattering on individual metal interfaces as well as by diffraction cross-coupling of SPs through the metal film. We show that these modes can be engineered to efficiently collect the fluorescence light from emitters on the top of the metal film and direct the emission to specific azimuth and polar directions into high refractive index substrate below the metallic film. The used dense sub-wavelength diffraction gratings do not couple the fluorescence light to the medium above the metal film.

2. Materials and methods

2.1 Materials

Photoresist Microposit S1818-G2 was purchased from Micro Resist Technology GmbH (Germany). Metal ion containing developer AZ 303 was obtained from MicroChemicals GmbH (Germany). Polydimethylsiloxane (PDMS) prepolymer and its curing agent were from Dow Corning (SYLGARD® 184). Amonil MMS10 was purchased from AMO GmbH (Germany). Poly(methyl methacrylate) (PMMA) was from Sigma-Aldrich Handels (Austria) and 1,1'-dioctadecyl-3,3,3′,3′-tetramethylindodicarbocyanine, 4 chlorobenzene-sulfonate salt (DiD) were from Invitrogen (LifeTech Austria). DiD dye exhibits the absorption and emission wavelengths of λ_{ab} = 644 nm and λ_{em} = 665 nm, respectively, and it was dispersed at the concentration of 700 nM in a toluene with dissolved PMMA (1.4 wt.%).

2.2 UV-NIL preparation of relief gratings

Holography was used for the preparation of master gratings. A polished Schott SF2 glass substrate with spin-coated photoresist layer was exposed to the interference field of two coherent collimated beams emitted from a HeCd laser at the wavelength λ = 325 nm (IK3031R-C, Kimmon Koha, Japan). Afterwards, the gratings were etched with a developer AZ-303 diluted with distilled water (volume ratio 1:9), rinsed with water and dried. Master gratings with sinusoidal relief modulation period Λ = 225-230 nm and depths of d = 10 and 30 nm were prepared and characterized by atomic force microscopy (data not shown). UV-nanoimprint lithography was used to replicate the master gratings as we described previously [21]. Briefly, a relief master grating was casted to a PDMS stamp which was cured overnight at 60 °C. Afterwards, the PDMS stamp was detached from the master and placed onto about 100 nm thick layer of UV-curable polymer Amonil that was spin-coated on a glass substrate. Amonil film in contact with the PDMS stamp was crosslinked by UV light dose of 36 J/cm^2 at a wavelength of λ = 365 nm (Bio-Link 365, Vilber Lourmat, Germany) followed by the release of the PDMS stamp from cured replica grating.

2.3 Layer structures supporting surface plasmons

LaSFN9 glass (refractive index of n_1 = 1.84 at λ_{em}) and BK7 glass (refractive index of n_1 = 1.51 at λ_{em}) substrates with Amonil grating (refractive index of n_2 = 1.51 at λ_{em}) were successively coated by layers supporting surface plasmons and containing DiD dye, see Fig. 1. Firstly, Ta$_2$O$_5$ (refractive index of n_3 = 1.79 at λ_{em}) and gold (refractive index n_4 = 0.167 + 3.91i at λ_{em}) films were deposited on the Amonil surface by using magnetron sputtering (UNIVEX 450C, Leybold Systems, Germany). The thickness of the gold film was set to 47 nm which is close to that providing the maximum strength of the coupling between surface plasmons and propagating waves in the glass substrate based on the Kretschmann configuration [22]. Afterwards, a 40 nm thick PMMA film (refractive index n_5 = 1.49 at λ_{em}) doped with DiD dyes was spin-coated on the gold surface and dried overnight at the room temperature. The PMMA surface was brought in contact with water (refractive index n_6 = 1.33 at λ_{em}) or air (refractive index n_6 = 1 at λ_{em}) in order to tune the propagation constant of

surface plasmons at the outer metal surface (SP_{outer}). The propagation constant of surface plasmons on the inner metallic surface (SP_{inner}) was varied by tuning the thickness of Ta_2O_5 layer t_3. Let us note that the Ta_2O_5 layer was deposited only on the LaSFN9 glass substrates with Amonil grating.
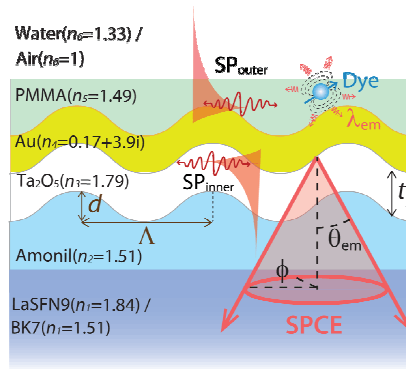

Fig. 1. Diffraction grating supporting surface plasmons that serve as emission channels for DiD dyes dispersed in a PMMA layer. Refractive indices of layers at the wavelength $\lambda_{em} = 670$ nm are shown for each layer.

3. Optical setup

Dispersion relation of surface plasmon modes on metallic grating surfaces was observed from angular reflectivity spectra R measured as a function of angle of incidence θ_I and wavelength λ. As seen in Fig. 2(a), a setup based on attenuated total reflection (ATR) method with Kretschmann configuration was used. A polychromatic beam from a halogen lamp (LSH102, LOT-Oriel, Germany) was coupled into an optical fiber (M25L02, Thorlabs, Germany), colimated with a lens (14 KLA 001, fl = 60 mm, CVI Melles Griot, Germany) and launched to a 90° glass prism that was made of identical glass as the grating sample substrate. At the prism base, the sample with a metallic grating was optically matched with a defined azimuth angle ϕ between the plane of incidence and grating vector **G**. The reflected light beam was coupled to an optical fiber and analyzed with a spectrometer (HR4000, Ocean Optics, USA). The prism and detectors were mounted on a two-circle rotation stage (Huber GmbH, Germany) in order to control the angle of incidence θ_I of the polychromatic beam in the prism. The data aquisition and control of the setup were supported by a home-built LabVIEW-based software. The reflectivity R was measured for transverse magnetic polarized incident beam (TM) and normalized with that measured for transverse electric polarization (TE).
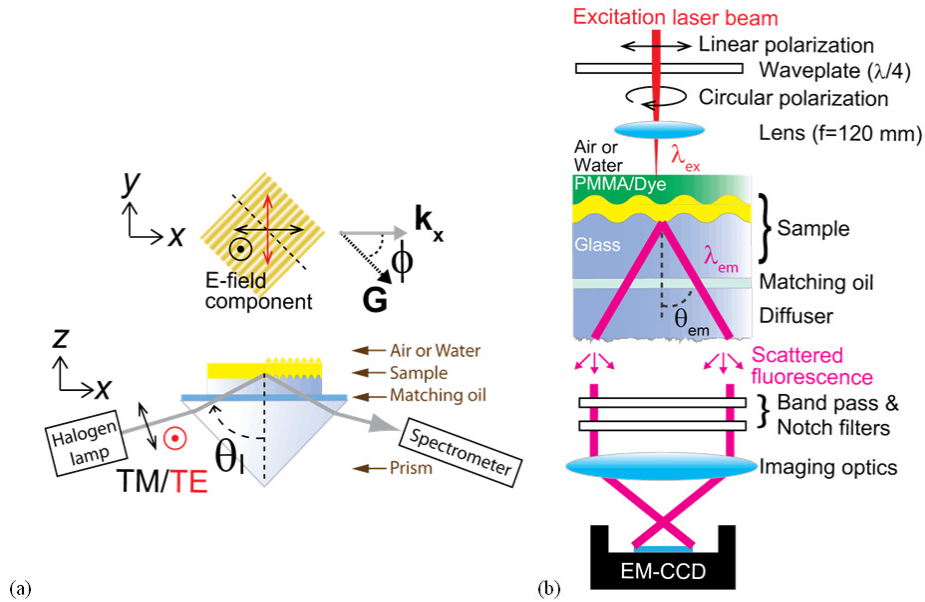
Fig. 2. Optical setup used for the measurement of (a) reflectivity spectra R as a function of angle of incidence θ_I, polar angle ϕ, and wavelength λ and (b) spatial distribution of surface plasmon-coupled emission in the glass substrate.

The measurement of spatial distribution of fluorescence intensity F emitted via surface plasmons into a glass substrate was carried out by using the setup depicted in Fig. 2(b). A sample with a metallic grating carrying a PMMA layer doped with a DiD dye was optically matched to a diffuser with rough bottom interface. Linearly polarized HeNe laser beam with the wavelength of $\lambda = 632.8$ nm that is close to the absorption wavelength of DiD dye $\lambda_{ab} = 644$ nm was circularly polarized by a quater waveplate (WPMQ05M-633, Thorlabs, Germany) and focused with a lens on the area of the surface of the structure with a diameter of about 100 μm. The fluorescence light coupled to surface plasmon modes at the emission wavelength λ_{em} of DiD dyes was re-radiated through the metal film based on the reverse Kretschamnn configuration, propagated through the substrate, and was scattered at the rough bottom surface of a diffuser made of LaSFN9 or BK7 glass. The spatial distribution of scattered fluorescence light was imaged onto an electron multiplying charge-coupled device (EM-CCD iXon + 885, Andor Technology, Ireland) by a camera lens (UNIFOC 58, Schneider Kreuznach, Germany). A set of filters including notch filter (XNF-632.8-25.0M, CVI Melles Griot, Germany) and band-pass filter (670FS10-25, LOT-Oriel, Germany) was used to reduce the background signal originating from the scattered and transmitted light at the excitation wavelength. The dependence of fluorescence signal on the polar angle θ_{em} in the glass substrate and azimuth angle ϕ was obtained from aquired fluorescence images. The central part of the image where the incident laser beam partially transmitted through the metal film was cut out by image processing as used filters did not suppress it totally.

4. Results and discussion

4.1 Surface plasmon-coupled emission on flat surface

The Bragg grating depicted in Fig. 1 supports surface plasmons at inner and outer interfaces of the metallic film. These modes act as pathways for fluorescence emission from dyes dispersed in the PMMA layer on the top of the gold film. Based on the Chance, Prock, and Silbey (CPS) model [9], we calculated the average energy dissipation density $dP/dk_{//}$ from an ensemble of dyes represented as randomly oriented dipoles. The energy dissipation density

for homogenously distributed dipoles in PMMA layer with the thickness of 40 nm was obtained by the averaging over distance from the metal surface between 0 and 40 nm as described in our previous work [20]. These simulations were carried out for flat layers (modulation depth $d = 0$ nm) shown in Fig. 1 with refractive indices taken from literature [23]. The results presented in Fig. 3 show $dP/dk_{//}$ as a function of in-plane component of the propagation constant $k_{//}$ of optical waves emitted from a dipole. $k_{//}$ is normalized by the propagation constant in vacuum k_0. They reveal that the coupling of fluorescence to surface plasmons at inner interface SP_{inner} (with the magnitude of propagation constant $k_{SPinner} = |\mathbf{k_{SPinner}}|$) and outer interface SP_{outer} (with the magnitude of propagation constant $k_{SPouter} = |\mathbf{k_{SPouter}}|$) is manifested as two distinct peaks. The probability of the emission via surface plasmons at inner and outer interfaces was calculated by integrating the energy dissipation density $dP/dk_{//}$ across respective peaks. For the layer architecture with 100 nm thick Ta_2O_5 on LaSFN9 glass and refractive index of the upper medium of $n_6 = 1.33$, 54 and 7% of emission events occurred via SP_{outer} and SP_{inner}, respectively. The fluorescence emission probability via SP_{outer} and SP_{inner} was redistributed to 40 and 14%, respectively, on the layer architecture consisting of BK7 glass without Ta_2O_5 layer. For both geometries, the peak energy dissipation density for the outer surface plasmon SP_{outer} is higher than that for the inner surface plasmon SP_{inner} due to the stronger overlap of SP_{outer} field with PMMA layer containing DiD dyes. The peak energy dissipation density for SP_{inner} is higher for the layer structure with BK7 substrate without Ta_2O_5 layer because its magnitude of propagation constant $k_{SPinner}$ is lower and thus larger portion of its field is carried in the PMMA layer. The fluorescence signal emitted via outer surface plasmon SP_{outer} can be recovered by the reverse Kretschmann configuration of ATR while that emitted via the inner surface plasmons SP_{inner} requires other means – e.g. diffraction grating. These simulations take into account fluorescence quenching due to the coupling to surface lossy waves with large propagation constant [9] ($k_{//}$ from 0 to $15k_0$ was assumed in the model). This coupling is highly dependent on the distance from the metal surface. The majority of emission events is quenched below a characteristics length of about 15 nm which is smaller than the thickness of PMMA layer with dispersed DiD dyes.
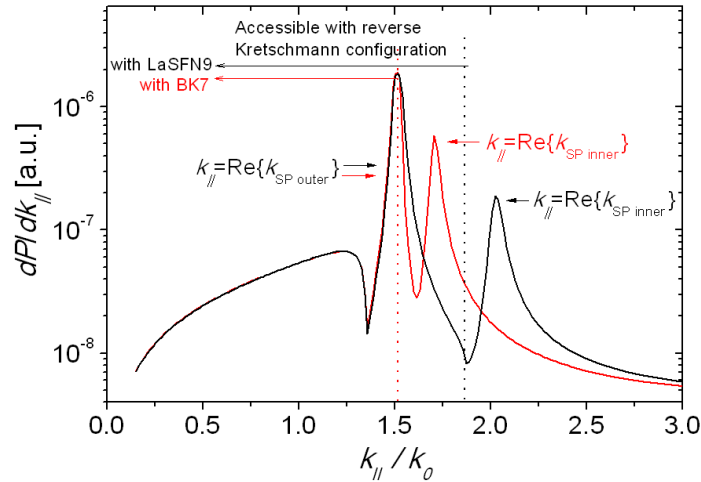

Fig. 3. Simulated average energy dissipation density $dP/dk_{//}$ of dyes dispersed in the 40 nm thick PMMA layer on the top of gold film with ($t_3 = 100$ nm, black line) or without ($t_3 = 0$ nm, red line) Ta_2O_5 layer. LaSFN9 (black line) and BK7 (red line) substrates were assumed. The PMMA layer is in contact with water ($n_6 = 1.33$).

4.2 Surface plasmon modes on corrugated metallic surfaces

On a corrugated layer structure, the characteristics of inner surface plasmons SP_{inner} and outer surface plasmons SP_{outer} are altered due to the interaction with the grating momentum $|\mathbf{G}| =$

$2\pi/\Lambda$. In order to investigate changes in SP_{inner} and SP_{outer} modes, numerical simulations were carried out by using finite element method (FEM) implemented in a diffraction grating solver DiPoG (Weierstrass Institute, Germany). Figure 4(a) shows an example of the simulated dispersion relation of surface plasmon in the dependence of the reflectivity R on the angle of incidence θ_I and wavelength λ. For the grating structure with the modulation depth of $d = 30$ nm, Ta_2O_5 layer thickness of $t_3 = 100$ nm, and the refractive index of the upper medium $n_6 = 1.33$, the dispersion relation of SP_{outer} (at angles $\theta_I > 47$ deg) is split in the vicinity to the wavelength of $\lambda = 670$ nm at which the grating momentum $\mathbf{G}$ matches the $2\mathbf{k_{SPouter}}$. In this region, the counter-propagating SP_{outer} are Bragg scattered [24], which gives rise to a bandgap in their dispersion relation. At edges of the bandgap, Bragg-scattered surface plasmon modes (BSSPs) can be excited at wavelengths of $\lambda = 630$ nm and 730 nm. These SP_{outer} modes are referred as to ω^+ mode ($\lambda = 630$ nm) and ω^- mode ($\lambda = 730$ nm) and they exhibit electric field intensity localized at grating peaks (ω^-) and valleys (ω^+) as seen in Fig. 5(a) and 5(b), respectively. Let us note that the electric field intensity profiles are normalized with the maximum intensity $|\mathbf{E_{max}}|^2$ to clarify the field distribution of considered plasmon modes. The increased PMD on the grating surface occurs at wavelengths where BSSPs can be excited as these modes are less dependent on the angle of incidence θ_I than regular surface plasmons, see Fig. 4. An additional resonance due to the $-1st$ order diffraction grating coupling to surface plasmons at the inner surface of the gold film ($G-SP_{inner}$) is observed in Fig. 4(a). This resonance is associated with the field enhancement at the inner interface of the gold film as confirmed by the electric field intensity distribution presented in Fig. 5(c). $G-SP_{inner}$ resonance crosses over the SP_{outer} dispersion relation at wavelengths λ around 800 nm. When decreasing the thickness of Ta_2O_5 layer t_3, the momentum of SP_{inner} decreases and the resonance wavelength for the excitation of $G-SP_{inner}$ is blue-shifted. For the layer structure with Ta_2O_5 layer thickness of $t_3 = 0$ nm, $G-SP_{inner}$ resonance overlaps with the bandgap in SP_{outer} dispersion relation, see Fig. 4(b). The electric field intensity profile for $G-SP_{inner}$ inside the bandgap is presented in Fig. 5(d) and it shows this mode is partially coupled to SP_{outer} and exhibits a BSSP ω^+ nature at both inner and outer metallic interfaces. We assume that it originates from diffraction coupled counter-propagating SP_{outer} and SP_{inner} when $\mathbf{k_{SPouter}} = \mathbf{G-k_{SPinner}}$ holds.
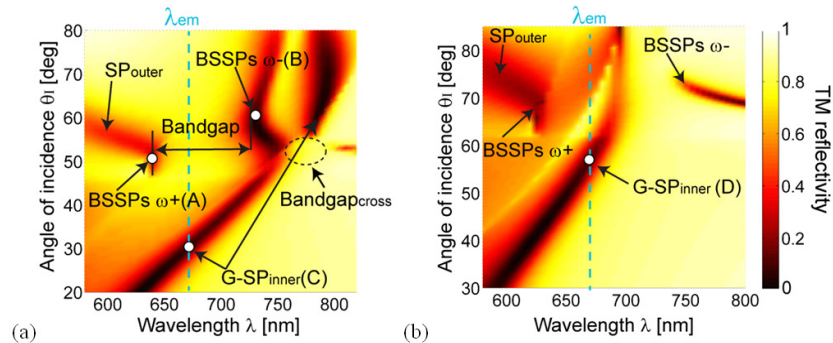

Fig. 4. Simulated reflectivity for grating modulation depth $d = 30$ nm and Ta_2O_5 layer with the thickness of (a) $t_3 = 100$ nm and (b) $t_3 = 0$ nm. The reflectivity (a) was calculated for LASFN9 substrate and (b) for BK7 substrate. Water on the top of PMMA layer and the azimuth angle $\phi = 0$ deg are assumed.
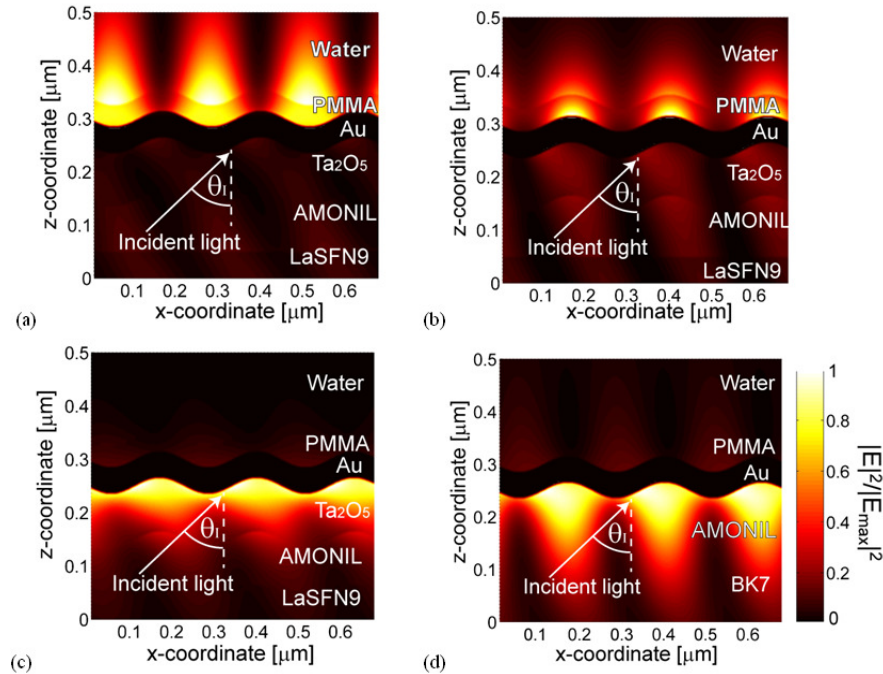
Fig. 5. Electric field intensity across the Bragg grating $|E|^2$ normalized with the maximum intensity $|(\mathbf{E})_{max}|^2$ calculated for (a) ATR–coupled BSSP mode ω^+ and (b) ATR–coupled BSSP mode ω^- at the outer gold interface, (c) grating-coupled propagating SP at the inner gold interface, and (d) coupled surface plasmon at the inner and outer interfaces. The respective angles and wavelengths are noted as circles in Fig. 4.

4.3 SPCE mediated by regular surface plasmons

SPCE on a flat layer structure without the corrugation ($d = 0$ nm) and air on the top ($n_6 = 1$) was firstly examined. The measured dispersion relation of surface plasmons for this geometry is shown in Fig. 6(a). It reveals that SPR occurs at the angle $\theta_I \sim 39$ deg in the LaFN9 glass substrate for the emission wavelength $\lambda_{em} = 670$ nm. The fluorescence image presented in Fig. 6(b) exhibits the characteristic SPCE cone with the polar angle $\theta_{em} \sim 38$ deg which is in agreement with the SPR condition at the emission wavelength λ_{em} in Fig. 6(a).
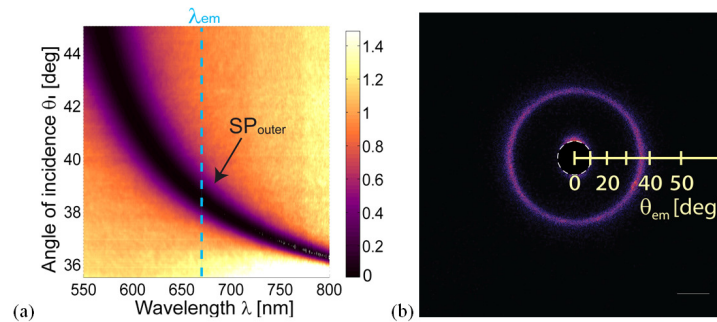

Fig. 6. (a) Dispersion relation of surface plasmons and (b) corresponding fluorescence emission image for flat layer structure on LaSFN9 substrate without Ta_2O_5 layer ($t_3 = 0$ nm) and air on the top $n_6 = 1$.

4.4 SPCE mediated by Bragg-scattered surface plasmons

Further, we investigated the effect of a Bragg grating to fluorescence emission on the samples supporting BSSPs modes close to the emission wavelength λ_{em}. When the refractive index of the upper medium is increased to $n_6 = 1.33$ and the layer structure is corrugated with the modulation depth of $d = 10$ nm, the resonant coupling to SP_{outer} shifts to higher angles and a gap appears in their dispersion relation. As seen in Fig. 7(a), BSSP modes located at edges of the bandgap occur at wavelengths of $\lambda = 670$ nm (ω^+) and 700 nm (ω^-). The BSSP ω^+ wavelength matches the fluorescence emission wavelength λ_{em} which leads to additional confinement of fluorescence signal on the SPCE cone at azimuth angles close to $\phi = 0$ and 180 deg, see Fig. 7(b). The peak intensity at these angles where emission via BSSP ω^+ occurs was increased by a factor of ~3 compared to that for regular SPCE cone. This effect is due to the enhanced PMD associated with the presence of BSSP at the emission wavelength λ_{em} [24]. The emission via BSSPs occurs only at narrow range of azimuth angles as the bandgap is blue-shifted away from the emission wavelength λ_{em} by increasing ϕ. When increasing the modulation depth to $d = 30$ nm, the bandgap becomes wider and BSSP ω^+ and ω^- modes shifts to the wavelengths of 625 nm and 730 nm, respectively [see Fig. 7(c)] which agrees well with simulations presented in Fig. 4(a). Small differences between measured and simulated dispersion relation can be attributed to the discrepancy in refractive indices of materials and possible changes in modulation depth of the replicated grating. For this sample, the emission wavelength λ_{em} lies inside the bandgap and thus SPCE signal is canceled in the direction $\phi = 0$ and 180 deg as shown in Fig. 7(d). Interestingly, the intensity of whole SPCE cone associated with emission via SP_{outer} modes is strongly decreased and the intensity of fluorescence signal at smaller polar angles θ_{em} is dramatically enhanced. This emission pattern is not symmetrical and the maximum intensity is observed at azimuth angles $\phi \sim \pm 50$ and ± 130 deg.
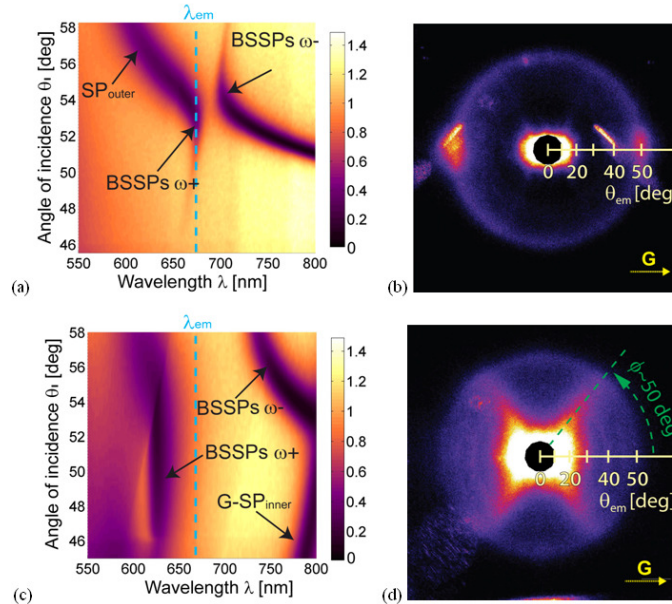

Fig. 7. Dispersion relations of surface plasmon modes on a gold grating surface with the Ta_2O_5 layer ($t_3 = 100$ nm) and water on the top ($n_6 = 1.33$) for the modulation depth of (a) $d = 10$ nm and (c) $d = 30$ nm. Corresponding spatial distribution of fluorescence light emitted into a LaSFN9 glass substrate for grating with the modulation depth of (b) $d = 10$ nm and (d) $d = 30$ nm.

In order to elucidate the origin of this feature, dispersion relation of surface plasmon modes supported by the grating was measured for azimuth angles varied from $\phi = 0$ to 90 deg.

As shown in Fig. 8(a)-8(d), the wavelength at which G-SP$_{inner}$ occurs is gradually blue-shifted and become less dependent on the angle of incidence θ_I when increasing the azimuth angle ϕ. This observation agrees with previously reported works [25]. The measured azimuthal dispersion indicates that the the resonant coupling to G-SP$_{inner}$ occurs at the emission wavelength of DiD dye λ_{em} = 670 nm for the azimuth angle ϕ = 50 deg. This angle matches the one at which the enhanced fluorescence emission was observed in Fig. 7(d). The weak dependence of the resonant wavelength on the angle of incidence θ_I explains the broad polar angular range at which the fluorescence light is emitted via G-SP$_{inner}$. These data reveal that SP$_{inner}$ can efficiently collect fluorescence light from fluorophores placed at the outer metallic surface. This feature is interesting as the simulated probability of the fluorescence emission for SP$_{inner}$ on a flat structure is 6 times smaller than that for SP$_{outer}$ (see Fig. 3) due to the relatively small overlap of SP$_{inner}$ field with the top PMMA layer containing dyes [see Fig. 5(c)]. The enhanced emission rate via SP$_{inner}$ can be ascribed to the redistribution of fluorescence emission pathways associated with the cancelling SP$_{outer}$ on the corrugated grating layer architecture.
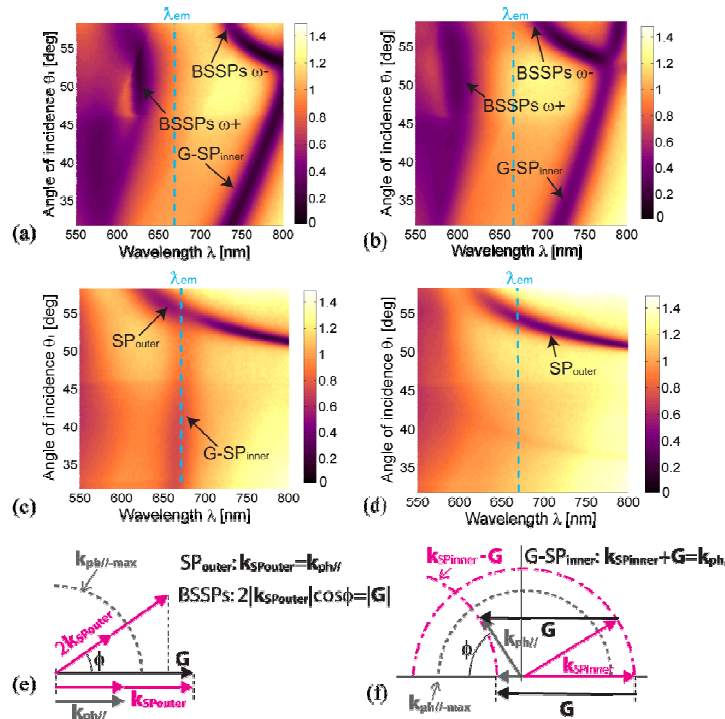

Fig. 8. Azimuth dependence of surface plasmon dispersion relation on a grating with the modulation depth d = 30 nm, Ta$_2$O$_5$ layer thickness t_3 = 100 nm, and water medium on the top n_6 = 1.33: (a) ϕ = 0 deg, (b) ϕ = 30 deg, (c) ϕ = 50 deg and (d) ϕ = 90 deg. Polar angles in LaSFN9 glass were measured. Momentum vector scheme for azimuth dependence of (e) Bragg-scaterred SP$_{outer}$ and (f) diffraction grating-coupled SP$_{inner}$.

In addition, momentum vector schemes are shown in Fig. 8(e)-8(f) in order to illustrate the azimuth dispersion of the coupling to SP$_{outer}$ and SP$_{inner}$. On the outer surface, the grating was designed to support Bragg-scattered SP$_{outer}$ (occurring when $2\mathbf{k_{SPouter}}$ = $\mathbf{G}$) at the wavelength 670 nm and azimuth angle ϕ = 0. Upon the excitation of SP$_{outer}$ at an increased azimuth angle ϕ > 0 deg, the parallel component of $2\mathbf{k_{SPouter}}$ to $\mathbf{G}$ is decreased and its magnitude does not match |$\mathbf{G}$|, see Fig. 8(e). In order to fulfill the Bragg-scattering condition, the magnitude of $\mathbf{k_{SPouter}}$ needs to be enlarged which occurs at lower wavelength and leads to

a blue shift of the bandgap as observed in Fig. 8(a)-8(d). For the inner surface, $SP_{SPinner}$ is excited by −1st diffraction order when the condition $\mathbf{k_{ph}}\text{-}\mathbf{G} = \mathbf{k_{SPinner}}$ holds (where $\mathbf{k_{ph//}}$ is the in-plane momentum vector of the incident light beam). As Fig. 8(f) shows, the G-SP_{inner} excitation requires an enhanced magnitude of the in-plane momentum of the incident light beam $|\mathbf{k_{ph//}}|$ when the azimuth angle ϕ is increased. This leads to the larger resonance (polar) angle of incidence θ_I at a given wavelength and to a blue shift of the G-SP_{inner} resonance at a fixed angle of incidence θ_I. This trend is in agreement with measured data presented in Fig. 8(a)-8(d).

4.5 SPCE mediated by cross-coupled surface plasmons

Finally, SPCE on the grating structure with cross-coupled surface plasmons at inner and outer metallic surface was studied. The gold grating with the modulation depth of d = 30 nm on BK7 glass substrate was brought in contact with air (n_6 = 1) and water (n_6 = 1.33) in order to tune the SP_{outer}. The refractive index at the inner gold surface was decreased by choosing the thickness of Ta_2O_5 layer t_3 = 0 nm which shifted the excitation of G-SP_{inner} to lower wavelength below 700 nm. For the structure in contact with air, anti-crossing between G-SP_{inner} and ATR-coupled SP_{outer} occurs as seen in the measured dispersion relation in Fig. 9(a). Figure 9(b) shows that for this configuration the SPCE signal at the direction parallel to the grating vector ϕ = 0 and 180 deg is cancelled due to the gap occurring at emission wavelength λ_{em}. In other directions ($\phi\neq0$ deg), SPCE retains its characteristic circular shape in the same manner with Fig. 8(b). When the refractive index of the upper medium is increased to n_6 = 1.33, the dispersion relation of SP_{outer} shifts to higher angles and a BSSP bandgap opens at wavelengths close to the emission wavelength λ_{em}, see Fig. 9(c).
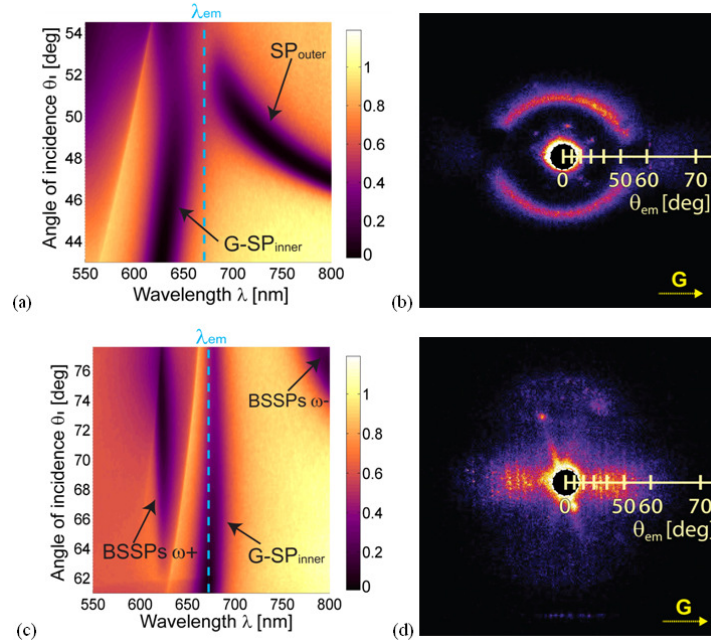

Fig. 9. Dispersion relation of cross-coupled surface plasmon modes for grating with the modulation depth of d = 30 nm and without Ta_2O_5 layer t_3 = 0 nm and the refractive index of upper medium (a) n_6 = 1 and (c) n_6 = 1.33 and respective fluorescence distributions emitted through the substrate (b) and (d).

As discussed in previous section, the grating-coupled SP_{inner} occurring inside this bandgap is partially cross-coupled to BSSPs ω^+ mode (see simulated dispersion relation in Fig. 4(b) which agree well with the experiment and electric field intensity profile in Fig. 5(d)). This

cross-coupling effect alters the dispersion relation of SP_{inner} which makes the resonance wavelength weakly dependent on the angle of incidence θ_I and increases the field strength at the outer gold interface, see Fig. 5(d). The corresponding SPCE image shows a dominant emission via SP_{inner} centered at azimuth angles $\phi = 0$ and 180 deg and cancelled SPCE cone via SP_{outer} modes. This fluorescence emission pattern has similarity to that shown in Fig. 7(d) for which the emission occurs at higher azimuth angles due to the larger propagation constant of SP_{inner} probing the Ta_2O_5 layer.

5. Conclusions

Dense sub-wavelength plasmonic gratings allow controlling spatial distribution of surface plasmon-coupled emission (SPCE) through a thin metal film on a dielectric substrate. The dispersion relation of surface plasmons at upper and lower interfaces of the thin metallic film can be simply tuned by changing the refractive index at respective metallic interfaces and enables exploiting a rich spectrum of Bragg scattered and cross-coupled surface plasmon modes. These waves can serve as efficient fluorescence decay channels for emitters placed on the top of the metallic film. In particular, modification of surface plasmon characteristics can suppress or enhance the fluorescence light intensity emitted to specific polar and azimuth directions on or inside the characteristic SPCE emission cone. These features can provide means for tuning the interaction of emitters with surface plasmons in areas including optical sources relying on nanoscale antennas and sensor utilizing surface plasmon-enhanced fluorescence spectroscopy. In particular, these observations may provide leads to advance plasmon-enhanced fluorescence sensors through more efficient collecting of fluorescence light emitted via Bragg-scattered surface plasmons, simpler detection of SPCE signal emitted at smaller polar angles and can be useful for multiplexing of sensing channels by emitting the fluorescence light from different sensing areas to different directions.

Acknowledgments

Active plasmonics with thermo-responsive hydrogel for biosensor applications

Mana Toma[†], Ulrich Jonas[‡,§], Anca Mataescu[‡], Wolfgang Knoll[†,Δ], Jakub Dostalek[,†]*

[†] AIT-Austrian Institute of Technology, BioSensor Technologies, Muthgasse 11/2, 1190 Vienna, Austria

[‡] Macromolecular Chemistry, University of Siegen, Department Chemistry -Biology, Adolf-Reichwein-Strasse 2, Siegen 57076, Germany

[§] Foundation for Research and Technology Hellas (FORTH), Bio-Organic Materials Chemistry Laboratory (BOMCLab), P.O. Box 1527, 71110 Heraklion, Crete, Greece

[Δ] Nanyang Technological University, Centre for Biomimetic Sensor Science, Singapore 637553

ABSTRACT: A new plasmonic sensor chip is developed which can rapidly actuate long range surface plasmons (LRSPs) and holds potential for biosensor applications. This approach relys on the thermo-responsive poly(N-isopropylacrylamide)-based hydrogel (NIPAAm) film attached to the sensor surface and rapid temperature modulation scheme based on indium tin oxide (ITO)

1

micro-heaters embedded into a sensor chip. The employed hydrogel exhibits a sharp phase transition in aqueous environment at lower critical solution temperature LCST=32 °C accompanied with a large thermo-optical coefficient of $dn/dT = 2 \times 10^{-2}$ °C^{-1}. In addition, the surface attached hydrogel film can simultaneously serve as an extended three-dimensional binding matrix in biosensor applications by modification with biomolecular recognition elements. In this paper, we developed layer architecture consisting of ITO micro-heaters, a sensing layer supporting long range surface plasmons and NIPAAm-based hydrogel layer on its top. This sensor platform was applied for time-resolved observations of swelling and collapsing processes of the NIPAAm-based hydrogel film. The results revealed that the hydrogel film with 1 μm thickness in swollen state can respond to a temperature stimulus faster than 100 ms a accompanied with a refractive index change as large as 0.1 over several hundred heating and cooling cycles. These features are employed to actuate LRSPs in surface plasmon-enhanced fluorescence (SPFS) biosensor for detection of fluorescence labeled molecular analytes. We revealed that rapid actuating of LRSPs allows switching on and off the fluorescence signal originating from target molecules captured in the hydrogel film on the sensor surface. Among others, this feature holds potential for implementation of time-multiplexing of sensing channels based on sequential readout of molecular binding events occurring at spatially separated areas on the sensor chip.

1. INTRODUCTION

Plasmonics represents rapidly developing research and technology that takes advantage of tight confinement of electromagnetic field at a metallic surface associated with resonant excitation of surface plasmons. The development of active plasmonic devices has attracted attentions due to

their potentials for applications in important areas, such as signal processing, photovoltaics, and sensing.[1] Up to now, various hybrid systems have been investigated to actuate surface plasmons, which are based on metallic surfaces with dielectric materials for electro-optical,[2, 3] thermo-optical,[4] magneto-optical,[5] photo-induced,[6] and electrochemical-based[7] modulating of refractive index. However, these approaches typically provide weak strength in refractive index modulation ($<10^{-2}$-10^{-3}) [8, 9] which is in most cases not sufficient to actuate surface plasmons.

In this work, we employ poly(N-isopropylacrylamide) (NIPAAm)-based hydrogel to actuate long range surface plasmons. NIPAAm represents a well characterized thermo-responsive material exhibiting a large thermo-optical coefficient in aqueous environment at the lower critical solution temperature (LCST) of 32 °C. Recently, this characteristics has been used to actuate localized surface plasmon resonance (LSPR) on arrays of metallic nanoparticles[10, 11] and implemented to surface-enhanced Raman spectroscopy[12] as well as surface plasmon resonance spectroscopy.[13, 14] In addition to the thermo responsive properties, NIPAAm-based hydrogel films attached to the SPR sensor surfaces can simultaneously serve as an extended three-dimensional binding matrix and optical waveguide mode supporting layers which are essential for biosensor applications[15]. In our laboratory, various NIPAAm-based hydrogel materials were developed and applied in optical biosensors based on hydrogel optical waveguide spectroscopy for direct detection[16, 17] and surface plasmon-enhanced fluorescence spectroscopy[18, 19] (SPFS) – for fluorescence detection of target analytes. The equilibrium thermo responsive properties of crosslinked NIPAAm-based layers were studied depending on the network density, medium in which hydrogel swells, and polymer backbone modifications.[13, 20-23] This paper extends these studies by investigating the swelling and collapsing kinetics of the thin hydrogel films and the

dependency of their thermo-responsive properties on the modifications by proteins. The thermo-responsive hydrogel is employed for rapid actuation of surface plasmons by using a micro-heater . The implementation of depeloped sensor architecture for time-multiplexing of sensing channels in plasmon-enhanced fluorescence biosensor is discussed.

2. EXPERIMENTAL SECTION

2.1 Materials Carboxylated poly(N-isopropylacryamide) (NIPAAm)-based hydrogel, sodium para-tetrafluorophenol-sulfonate (TFPS) and S-3-(benzoylphenoxy)propyl ethanthiate (benzophenone thiol) were synthesized as described in the literature[14]. The NIPAAm-based hydrogel was composed of the terpolymer with N-isoproprylacrylamide, methacrylic acid, and 4-methacryloyl benzophenone, see Figure 1. N-isoproprylacrylamide monomer provided the thermo-responsive characteristics, methacrylic acid allowed for post-modification by other functional groups, and benzophenone moieties enabled the photo-crosslinking of the polymer network. The Cytop fluoropolymer (CTL-809M) was purchased from Asahi Glass (Japan). SU-8 and its solvent were obtained from MicroChem (USA). Phosphate buffer saline (PBS, 10 mM phosphate, 140 mM NaCl, 3 mM KCl and a pH of 7.4) was from Callbiochem (Germany). PBS-Tween buffer (PBST) was prepared by adding 0.05 vol % of Tween 20 in PBS buffer solution. 1-Ethyl-3-(3-dimethylaminopropyl)carbodiimide (EDC) was obtained from Pierce (USA). 10 mM acetate buffer (ACT) with pH 4 was prepared from sodium acetate adjusting the pH by adding acetic acid. 1 M Ethanolamine with pH 8.5 was prepared from ethanolamine adjusting the pH by adding sodium hydroxide. Mouse immunoglobulin G (IgG) and goat anti-mouse IgG labeled with Alexa Fluor 647 were purchased from Molecular Probes (USA). The absorption and

emission bands of Alexa Fluor 647 label are at the wavelength λ_{ab}=652 and λ_{em}=670 nm, respectively. All other chemicals were purchased from Sigma-Aldrich (Germany).

Figure 1

2.2 Fabrication of sensor chip. Firstly, micro-heater that consisted of 25 nm thick indium tin oxide (ITO) pad with a pair of 50 nm thick gold electrodes was prepared on a BK7 glass substrate by sputtering (UNIVEX 450C from Leybold, Germany). The ITO pad area of 0.5×1 mm^2 and the gold electrodes stripe width of 0.5 mm were defined by using a set of CO_2 laser-cut stencil masks. On the top of ITO micro-heater, layer architecture supporting long range surface plasmons (LRSP) was deposited as described in our previous works.[24, 25] Briefly, Cytop fluoropolymer layer with a thickness of 600 nm was spincoated over the whole sensor chip followed by the sputtering of 20 nm thick SPR-active gold film. Let us note that the Cytop film protected the ITO micro-heater with gold electrodes. In addition, it served as a low refractive index buffer layer (with refractive index of 1.337 at the wavelength of λ=633 nm) providing a refractive index symmetrical geometry that is required for the excitation of LRSPs on the 20 nm thick gold film with a hydrogel swollen in aqueous medium on its top, see Figure 2.

Figure 2

5

NIPAAm-based hydrogel was tethered to a gold surface by using an SU-8 or BP-thiol linker[14] layers. The polymer was dissolved in ethanol at a concentration of 20 mg/mL and spincoated on the area supporting LRSPs. Afterwards, the layer was dried in vacuum and exposed to UV light (wavelength 365 nm, irradiation dose of 4 J cm^{-2}) in order to covalently crosslink and attach the polymer network to the gold surface. The thickness and refractive index of a dry hydrogel film were determined by surface plasmon resonance (SPR) as d_{h_dry}=135 nm and n_{h_dry}=1.48,[26] respectively.

The immobilization of mouse IgG catcher molecules in the NIPAAM-based hydrogel matrix was performed *in situ*. Firstly, the hydrogel was swollen in ACT buffer and its carboxylic moieties were activated by 20-minute flow of water solution with a mixture of TFPS (10.5 mg mL^{-1}) and EDC (37.5 mg mL^{-1}). Then, the surface was rinsed with ACT buffer for 5 minutes and mouse IgG dissolved in ACT buffer at a concentration of 50 µg mL^{-1} was flowed over the activated hydrogel surface. After the reaction of mouse IgG with TFPS-activated carboxylic groups in the hydrogel layer, the un-reacted TFPS moieties were blocked by 20-minute incubation in a solution with 1 M ethanolamine at pH 8.5. Finally, the functionalized hydrogel was successively washed with ACT and PBS for 5 and 10 min, respectively. The surface mass density Γ of covalently immobilized mouse IgG was controlled by the time for which the protein solution was flowed across the surface (between 0 and 60 min) and it was determined by the spectroscopy of LRSP and hydrogel optical waveguide (HOW) modes as described in our previous studies.[16, 17]

2.3 Experimental setup An optical setup utilizing attenuated total reflection (ATR) method with Kretschmann configuration was employed. This setup combined the angular interrogation of

6

LRSPs with spatially resolved measurements based on surface plasmon resonance imaging (SPRI). As shown in Figure 3, a parallel monochromatic light beam with transverse magnetic (TM) polarization was coupled to a 90° prism made of LASFN9 glass. As a light source, He-Ne laser (PL610P, Polytec, Germany) emitting light at a wavelength of 633 nm or LED (LE-1R-C, WT&T Inc.) with narrow transmission band pass filter (FL632.8-10, Thorlabs) was used. At the prism base, a sensor chip with ITO micro-heater and LRSP-supporting layers was optically matched by using refractive index matching oil. The intensity of the light beam reflected from the prism base was measured with a photodiode detector connected to a lock-in amplifier (Model 5210, Princeton Applied Research) or by using a CCD camera (piA1000-48gm, Basler AG) with a C-mount camera lens (UNIFOC 58, Schneider Kreuznach). Two-circle rotation stage (Huber GmbH, Germany) was used for the control of the angle of incidence θ of a light beam hitting the gold sensor surface. For the kinetics measurement, angle of incidence θ was fixed in vicinity to that where resonant coupling to LRSPs occurred and the reflectivity signal R was measured in time. Fluorescence light emitted into the aqueous medium from affinity captured molecules on the sensor surface was collected through the flow-cell with a lens (NA=0.3). The fluorescence intensity was measured in counts per second (cps) by a photomultiplier tube (H6240-01, Hamamatsu, Japan) which was connected to a counter (53131A, Agilent, USA). For spatially resolved measurements, the photomultiplier tube was replaced by electron multiplying charge-coupled device (EM-CCD iXon+885, Andor Technology, Ireland). A set of filters including notch (XNF-632.8-25.0M, CVI Melles Griot, Germany) and band-pass (670FS10-25, LOT-Oriel, Germany) filters were used in order to suppress the background signal outside the emission band centered at the wavelength of λ_{em}=670 nm.

Figure 3

Against the sensor surface, a flow-cell with the volume of 25 μL was attached in order to flow liquid samples at 0.5 mL/min by using a peristaltic pump. The sensor head comprising the prism, sensor chip and flow-cell was temperature stabilized at a background temperature T_0 by a Peltier device connected to a temperature control driver (LFI3751, Wavelength Electronics). In order to locally heat the sensor surface, ITO micro-heater gold electrodes were connected to a current modulator (NI9265, National Instruments). Typically, the ITO layer exhibited resistance of 280 Ω. The data acquisition, image processing and the control of the overall sensor system was performed by using LabVIEW-based software.

The local temperature changes induced by applying current to the micro-heater were calibrated by using temperature depending refractive index of water[27]. In this calibration process, the time resolved reflectivity measurement was performed at the angle of incidence which is slightly lower than that of LRSPs at bare gold sensor surface in contact with water. The reflectivity change was detected in time upon applying a series of current pulses I. Water is made to flow over the sensor surface. As shown in Figure 4a, the reflectivity R drops when the local temperature is increased by applying the current which is accompanied with decrease of refractive index of water.[27] At the end of the current pulse, the reflectivity R increases to the baseline as the heat rapidly dissipates from the sensor surface and local temperature decreases to that of background T_0. We defined the response time of the ITO micro-heater δt_μ as the time in which the change in reflectivity signal R reached to half of that in equilibrium (see Figure 4a).

The obtained response time of δt_μ=50 ms was identical for the heating and cooling phase. The dependence of equilibrium temperature T_{eq} on the current flow I was determined by comparing reflectivity changes δR upon the current flow I with those induced by changing the background temperature T_0 from 23 to 40°C. A typical calibration curve is presented in Figure 4b which shows a quadratic dependence of the temperature T_{eq} on the current I. It illustrates that developed micro-heater is able to increase the temperature on the sensor surface over 15 °C with respect to the background temperature T_0.

Figure 4

In order to determine thickness d_h and refractive index n_h of the hydrogel film at different temperatures, the measured angular reflectivity spectra were fitted by Fresnel-based model. A "box" approximation was employed in which the gradient of the hydrogel density perpendicular to the surface was omitted. By fitting the spectral features associated with the coupling to LRSP and hydrogel optical waveguide HOW modes, both n_h and d_h were independently determined.[16]

3. RESULTS AND DISCUSSION

3.1 Equilibrium characteristics of NIPAAm-based hydrogel. The equilibrium thermo-responsive properties of the surface attached NIPAAm-based hydrogel film were studied by measuring SPR spectra at various background temperatures T_0. Firstly, the temperature

depending thickness change of the hydrogel film in contact with water was investigated. Figure 5a shows a series of angular reflectivity spectra of the hydrogel film attached to the LRSPs supporting layer at various temperatures T_0=20 to 35 °C. The resonant excitations of LRSPs are manifested as a narrow dip in the angular reflectivity spectrum located at angles θ=49.5-50.5 deg. Additional feature is observed below the critical angle $\theta<\theta_c$ which is associated with coupling to HOW mode.[17] By increasing the temperature T_0, the LSPR dip shifted to higher angles and HOW dip disappears as can be seen in the increase of reflectivity below the critical angle. These changes are induced by the gradual collapse of the hydrogel film accompanied with an increase of its refractive index n_h. The thickness (d_h) and the refractive index (n_h) of the hydrogel are obtained by fitting the refractivity spectra. The swelling ratio Φ of the hydrogel film was determined by normalizing the fitted thickness d_h with that of the dry hydrogel film d_{h_dry}. The temperature dependence of the swelling ratio Φ and refractive index of the hydrogel film is shown in Figure 5b. These data show a sharp phase transition of the NIPAAm hydrogel accompanied with large changes in swelling ratio and refractive index at lower critical temperature, LCST=32 °C. The transition of the hydrogel from swollen to collapsed state is accompanied with a large refractive index change of Δn_h=0.1. Moreover, this change occurs within a narrow temperature range which leads to thermo-optical coefficient as large as dn_h/dT_0=2.2×10^{-2} °C^{-1} at T_0=32 °C. The swelling ratio differs by a factor of 4.1 between the swollen (Φ=6.2 at T_0=20 °C) and fully collapsed (Φ=1.5 at T_0=40 °C) state which agree with previous studies.[21]

Figure 5

Secondly, the thermo-responsive properties were investigated for the hydrogel films in contact with PBS buffer which is often used in biosensor applications. Particularly, the effects of chemical modification of carboxyl groups in hydrogel polymer chains (see Figure 1) on the thermo-responsive properties were investigated. In this set of experiments, the surface attached hydrogel films were modified with different amount of mouse IgG and ethanolamine (ETA). The amount of mouse IgG loaded in hydrogel film was obtained by fitting the SPR curves before and after the modification process. The swelling properties of the unmodified and modified hydrogel in PBS buffer were obtained by taking SPR spectra at various background temperatures. Figure 6 shows the temperature depending swelling ratio of the hydrogel films with different chemical modifications. For unmodified hydrogel film, it exhibits higher swelling ratio Φ=8.3 in contact with PBS buffer than that with water at T_0=20 °C. Furthermore, the thermo induced phase transition is strongly hindered as its swelling ratio decreases only by a factor of 1.3 at T_0=40 °C (see curve 1 in Figure 6). The thermal responsiveness of the hydrogel in PBS can be enhanced by the replacement of its carboxyl groups by ETA. The swelling ratio of ETA-modified hydrogel decreases by a factor of 2.3 (see curve 2 in Figure 6) by raising the temperature from T_0=20 to 40 °C. When the carboxyl groups were reacted with mouse IgG followed by the passivation with ETA, the responsiveness of the hydrogel gradually decreases with increasing the amount of the immobilized mouse IgG. As seen in Figure 6 (curves 3 and 4), the collapsing factors of 2.2 and 1.4 were observed for IgG-loaded hydrogel films with the surface mass densities of Γ=8.2 and 26.4 ng/mm^2, respectively. This weaker thermal responsiveness of the IgG-modified hydrogel films in PBS results in significantly lower thermo-optical coefficient of $dn_h/dT_{eq}\sim 10^{-3}$ °C^{-1} at the

original lower critical temperature T_0=32 °C for unmodified hydrogel film in water (see Figure 6).

Figure 6

3.2 Kinetics of swelling and collapse of NIPAAm-based hydrogel. The response time of the hydrogel film to temperature stimuli was investigated by time-resolved reflectivity measurement. In this measurement, the kinetics of swelling and collapsing of the hydrogel were studied upon the temperature stimuli induced by the ITO micro-heater. Firstly, the kinetics of unmodified NIPAAm-based hydrogel film in contact with water was investigated. The reflectivity was measured at the angle of incidence θ=49.8 deg which is in the slope of the reflectivity dip associated with LRSPs, see Figure 5a. The reflectivity R was acquired every 20 ms which is smaller than the response time of the ITO micro-heater δt_μ. The background temperature was adjusted to T_0=20 °C by using the Peltier element. After the reflectivity signal R was stabilized, the current I between 5 and 13 mA was flowed through the micro-heater (t=0 s) for 5 s in order to increase the local temperature between T_{eq}=24 and 34 °C. Then, the current flow was stopped and the local temperature decreased to T_0. Results in Figure 7a show that the heating sensor surface at t=0 s leads an increase in the reflectivity R due to the shift of resonance angle of LRSPs associated with the hydrogel collapses (see Figure 5). After stopping the current flow at

t=5 s, the reflectivity R rapidly drops to the baseline induced by temperature decreasing to T_0 accompanied with swelling of hydrogel film. When increasing the equilibrium temperature T_{eq} by raising the current I, the reflectivity R saturates at higher levels due to the stronger collapse of the hydrogel film. The reflectivity change δR observed for the sensor surface covered with the thermo-responsive hydrogel (see Figure 7a) is about one order of magnitude higher than that for the bare surface in contact with water (see Figure 4a). The reason is the larger thermo-optical coefficient of the hydrogel dn_h/dT_0=2.2×10^{-2} °C^{-1} with respect to that of water dn_{H2O}/dT_0=-1.2×10^{-4} °C^{-1} at T_0=32 °C.

Figure 7

Let us note that reflectivity changes δR shown in Figure 7a are not proportional to the hydrogel thickness d_h when the hydrogel is collapsed and the slope of the reflectivity cannot be assumed to be linear anymore, see the reflectivity spectra in Figure 5a. In order to obtain more detail information on the swelling and collapsing kinetics, the hydrogel thickness d_h were calculated by comparing the reflectivity signal R upon the current flow I = 13 mA (in Figure 7a) with a series of angular spectra measured for different equilibrium temperatures T_0 (in Figure 5a). As shown in Figure 7b, the result reveals that the collapsing process occurs in two phases. In the first 250 ms after the current apply, the hydrogel rapidly collapses from d_h =690 nm to 420 nm with a characteristic time of δt_I ~ 100 ms (phase I). Afterwards, the hydrogel undergoes a slower transition with one order of magnitude larger characteristic time δt_{II} ~ 1.1 s to reach the equilibrium (phase II) accompanied with the thickness change from d_h =420 nm to 290 nm. The

swelling process takes shorter time than that of collapsing process. The initial process (phase I) proceeds fast swelling accompanied with the thickness changes from d_h =290 nm to 610 nm with a characteristic time of $\delta t_I \sim 50$ ms. The following process (phase II) is less pronounced accompanied with thickness change from d_h =610 nm to 660 nm and shows a characteristic time of δt_{II}~800 ms. Let us note that the difference in the kinetics of swelling and collapsing can be attributed to the performance characteristics of the developed temperature modulation systems and the differences in the slopes of swelling ratio and temperature $d\Phi/dT_0$ where the hydrogel is swollen ($d\Phi/dT_0$=-0.12 °C^{-1} at T_{eq}=22.5 °C) and collapsed ($d\Phi/dT_0$=-0.49 °C^{-1} at T_{eq}=32 °C), see Figure 4a and Figure 5a, respectively. As shown in Figure 4a, the fast and dominant temperature changes occur within 100 ms after applying or stopping the current flow, and the changes become slower as they reach to the equilibrium temperature. In the collapsing process, the temperature needs to be increased over 10 °C in order to be above the LCST. In the fast heating period after the current is applied to the micro-heater, the hydrogel film exhibits small slope of $d\Phi/dT_0$ which results in small thickness changes in the phase I. When the temperature reaches to the LCST where the hydrogel film exhibits a large slope $d\Phi/dT_0$, temperature changes become slower that makes collapsing process slower in the phase II. This slow collapsing process can be partially attributed to hindered diffusion of water through denser polymer network. Contrary to the collapsing process, the swelling process is accompanied with the rapid cooling across the LCST and a large slope of $d\Phi/dT_{eq}$ which leads the rapid thickness changes of the hydrogel film. In addition, the rapid phase I of swelling may associate with fast diffusion of water into the polymer network. The slower collapsing process in phase II can be attributed to the possible slow relaxation of polymer chains.

Assuming that the phase transition of the hydrogel film is dominated by one-dimensional diffusion of polymer chains in water, its response time to an external stimulus can be described as $\sim d_\mathrm{h}^2/2D_\mathrm{m}$, where D_m is a mutual diffusion coefficient. As swelling and collapsing response time is faster than 100 ms for the 690 nm thick hydrogel film, the mutual diffusion coefficient D_m can be estimated to be larger than 4×10^{-6} mm^{2}s^{-1} which is within the lower range of values reported for similar hydrogel films by other works.[28] As the observed hydrogel response time is limited by the resolution of developed micro-heater ($\delta t_\mu \sim 50$ ms) the modulation speed of SPR can be enhanced by improving the performance of this component.

The kinetics of swelling and collapsing was studied for the IgG-modified hydrogel film in contact with PBS as well. Figure 8 shows the result of the time-resolved reflectivity measurement on swelling and collapsing of IgG-modified hydrogel film upon the repeating current flows to the micro-heater. In this measurement, the applied current was set to which can heat the sensor surface to 34 °C and repeating current pulses with 100 ms width are applied to the micro-heater. The magnitude of the reflectivity variations induced by heating was smaller by a factor of two with respect to that of unmodified hydrogel in contact with water. The swelling and collapsing of the hydrogel was shown to be fully reversible and allowed for several hundred cycles without a change in the thermo responsive properties. The width of the reflectivity peak induced by a current pulse was $\Delta t \sim 100$ ms (defined as full width of the half maximum - FWHM) as seen in Figure 8.

Figure 8

3.3 Implementation to surface plasmon-enhanced fluorescence biosensor. The developed

sensor platform with active plasmonic architecture is employed for the manipulation of

fluorescence signals in SPFS based biosensors. In this experiments, NIPAAm-based hydrogel

film with the thickness of d_h=860 nm in PBS was modified with mouse IgG with the surface

mass density Γ=19 ng/mm^2. Afterwards, Alexa Fluor 647 dye-labeled anti-mouse IgG dispersed

in PBST at concentration of 20 µg/mL was flowed over the sensor surface for 80 min followed

by rinsing with PBST for 10 min. The change in surface mass density due to the affinity binding

of anti-mouse IgG in the hydrogel matrix was determined as $\Delta\Gamma$=3.3 ng/mm^2 by fitting the

reflectivity spectra shown in Figure 9a. As this figure shows the binding of a-mIgG produces

strong fluorescence signal F at angles where HOW and LRSP modes are resonantly exited.

When the temperature is increased from T_{eq}=23 °C to 35 °C by using the micro-heater, the shifts

of the resonance angles lead the change in the fluorescence peaks, see Figure 9b. Especially, the

fluorescence intensity exhibits a dramatically change at the resonance angle of HOW mode

(θ=47.5 deg) at the temperature of T_0=23 °C, see δF in Figure 9b. The time-resolved

fluorescence measurement was carried out at this angle of incidence upon the temperature

modulations by using ITO micro-heater. As Figure 9c shows, the fluorescence signal F became

close to the background due to the weak coupling to HOW mode by heating the sensor pad to

T_{eq}=35 °C. After the decreasing of temperature to T_0=23 °C, the reflectivity signal R decreases

which indicates stronger coupling to HOW modes and fluorescence signal F is strongly

enhanced. The inserted fluorescence images in Figure 9c shows the spatial distribution of the

fluorescence signal that is measured from the sensor surface by using an EM-CCD camera. Upon

the resonant excitation of HOW mode at T_{eq}=23 °C a clear fluorescence signal is observed from

the sensor pad coated with NIPAAm-based hydrogel film. After increasing the temperature to

T_{eq}=35 °C, the signal decreases to background. Let us note that the angular spectra shown in Figure 9a-b are taken from different sensing spot in the same sensor chip. The beam diameter is adjusted by using an aperture in order to fit into the sensor spot before each experiment. That causes the difference in the reflectivity and fluorescence intensity of Figure 9a-c.

Figure 9

4. CONCLUSIONS

A new approach to rapid actuation of surface plasmon resonance (SPR) was investigated based on thermo-responsive NIPAAm-based hydrogel and an ITO micro-heater embedded to SPR-active layer architecture. The developed scheme allowed strong modulating of refractive index on a metallic surface supporting surface plasmons with the thermo-optical coefficient as large as 2.2×10^{-2} °C^{-1}. The kinetics measurements of swelling and collapsing of the hydrogel films were carried out with the unmodified and modified hydrogel with mouse IgG molecules. The characteristic response time of around 100 ms was obtained for a hydrogel film with sub-micrometer thickness. As the hydrogel layer can simultaneously serve as a binding matrix with a large binding capacity of the capture molecules, we implemented the developed sensor chip into a biosensor which relies on the surface plasmon-enhanced fluorescence and the fluorophore-labeled anti-mouse IgG antibodies was detected. The actuating of surface plasmon modes by collapsing and swelling of the hydrogel allowed switching on and off the fluorescence signal

17

from a sensing pad. This functionality can be employed in future work for time multiplexing of sensing channels that utilizes sequential readout from spatially separated sensing spots.

AUTHOR INFORMATION

Corresponding Author

* Tel +43 (0) 50550 4470. Fax: +43(0) 50550-4450. Email: jakub.dostalek@ait.ac.at.

Homepage: http://www.ait.ac.at.

NOTES

The authors declare no competing financial interest.

REFERENCES

1.   Schuller, J. A.; Barnard, E. S.; Cai, W. S.; Jun, Y. C.; White, J. S.; Brongersma, M. L., Plasmonics for extreme light concentration and manipulation. *Nature Materials* **2010,** 9, (3), 193-204.
2.   Dicken, M. J.; Sweatlock, L. A.; Pacifici, D.; Lezec, H. J.; Bhattacharya, K.; Atwater, H. A., Electrooptic Modulation in Thin Film Barium Titanate Plasmonic Interferometers. *Nano Letters* **2008,** 8, (11), 4048-4052.
3.   Smalley, J. S. T.; Zhao, Y. H.; Nawaz, A. A.; Hao, Q. Z.; Ma, Y.; Khoo, I. C.; Huang, T. J., High contrast modulation of plasmonic signals using nanoscale dual-frequency liquid crystals. *Optics Express* **2011,** 19, (16), 15265-15274.
4.   Gagnon, G.; Lahoud, N.; Mattiussi, G. A.; Berini, P., Thermally activated variable attenuation of long-range surface plasmon-polariton waves. *Journal of Lightwave Technology* **2006,** 24, (11), 4391-4402.
5.   Temnov, V. V.; Armelles, G.; Woggon, U.; Guzatov, D.; Cebollada, A.; Garcia-Martin, A.; Garcia-Martin, J. M.; Thomay, T.; Leitenstorfer, A.; Bratschitsch, R., Active magneto-plasmonics in hybrid metal-ferromagnet structures. *Nature Photonics* **2010,** 4, (2), 107-111.
6.   Chen, H. S.; Wang, J. Y.; Yeh, S. S.; Chen, C. D.; Lin, H. Y., Modulation of surface plasmon wave by photo-induced refractive index changes of CdSe quantum dots. *Applied Physics Letters* **2012,** 100, (1).
7.   Leroux, Y.; Lacroix, J. C.; Fave, C.; Trippe, G.; Felidj, N.; Aubard, J.; Hohenau, A.; Krenn, J. R., Tunable electrochemical switch of the optical properties of metallic nanoparticles. *Acs Nano* **2008,** 2, (4), 728-732.
8.   Coppola, G.; Sirleto, L.; Rendina, I.; Iodice, M., Advance in thermo-optical switches: principles, materials, design, and device structure. *Optical Engineering* 50, (7).
9.   Zhang, X. Y.; Zhang, T.; Hu, A. M.; Xue, X. J.; Wu, P. Q.; Chen, Q. Y., Tunable Microring Resonator Based on Dielectric-Loaded Surface Plasmon Polariton Waveguides. *Journal of Nanoscience and Nanotechnology* 11, (12), 10520-10524.
10.   Tokareva, I.; Minko, S.; Fendler, J. H.; Hutter, E., Nanosensors based on responsive polymer brushes and gold nanoparticle enhanced transmission surface plasmon resonance spectroscopy. *Journal of the American Chemical Society* **2004,** 126, (49), 15950-15951.
11.   Gehan, H.; Mangeney, C.; Aubard, J.; Levi, G.; Hohenau, A.; Krenn, J. R.; Lacaze, E.; Felidj, N., Design and Optical Properties of Active Polymer-Coated Plasmonic Nanostructures. *Journal of Physical Chemistry Letters* **2011,** 2, (8), 926-931.
12.   Gehan, H.; Fillaud, L.; Chehimi, M. M.; Aubard, J.; Hohenau, A.; Felidj, N.; Mangeney, C., Thermo-induced Electromagnetic Coupling in Gold/Polymer Hybrid Plasmonic Structures Probed by Surface-Enhanced Raman Scattering. *Acs Nano* 4, (11), 6491-6500.
13.   Kuckling, D.; Harmon, M. E.; Frank, C. W., Photo-cross-linkable PNIPAAm copolymers. 1. Synthesis and characterization of constrained temperature-responsive hydrogel layers. *Macromolecules* **2002,** 35, (16), 6377-6383.
14.   Beines, P. W.; Klosterkamp, I.; Menges, B.; Jonas, U.; Knoll, W., Responsive Thin Hydrogel Layers from Photo-Cross-Linkable Poly(N-isopropylacrylamide) Terpolymers. *Langmuir* **2007,** 23, (4), 2231-2238.
15.   Aulasevich, A.; Roskamp, R. F.; Jonas, U.; Menges, B.; Dostálek, J.; Knoll, W., Optical Waveguide Spectroscopy for the Investigation of Protein-Functionalized Hydrogel Films. *Macromolecular Rapid Communications* **2009,** 30, (9-10), 872-877.

16.   Aulasevich, A.; Roskamp, R. F.; Jonas, U.; Menges, B.; Dostalek, J.; Knoll, W., Optical Waveguide Spectroscopy for the Investigation of Protein-Funcionalized Hydrogel Films. *Macromolecular Rapid Communications* **2009,** 30, 872-877.

17.   Wang, Y.; Huang, C. J.; Jonas, U.; Dostalek, J.; Knoll, W., Biosensor based on Hydrogel Optical Waveguide Spectroscopy. *Biosensors and Bioelectronics* **2010,** 25, 1663-1668.

18.   Wang, Y.; Brunsen, A.; Jonas, U.; Dostalek, J.; Knoll, W., Prostate Specific Antigen Biosensor Based on Long Range Surface Plasmon-Enhanced Fluorescence Spectroscopy and Dextran Hydrogel Binding Matrix. *Analytical Chemistry* **2009,** 81, (23), 9625-9632.

19.   Huang, C. J.; Dostalek, J.; Knoll, W., Long range surface plasmon and hydrogel optical waveguide field-enhanced fluorescence biosensor with 3D hydrogel binding matrix: On the role of diffusion mass transfer. *Biosens. Bioelectron.* **2010,** 26, (4), 1425-1431.

20.   Junk, M. J. N.; Anac, I.; Menges, B.; Jonas, U., Analysis of Optical Gradient Profiles during Temperature- and Salt-Dependent Swelling of Thin Responsive Hydrogel Films. *Langmuir* 26, (14), 12253-12259.

21.   Anac, I.; Aulasevich, A.; Junk, M. J. N.; Jakubowicz, P.; Roskamp, R. F.; Menges, B.; Jonas, U.; Knoll, W., Optical Characterization of Co-Nonsolvency Effects in Thin Responsive PNIPAAm-Based Gel Layers Exposed to Ethanol/Water Mixtures. *Macromolecular Chemistry and Physics* 211, (9), 1018-1025.

22.   Yu, H.; Grainger, D. W., Thermosensitive Swelling Behavior in Cross-Linked N-Isopropylacrylamide Networks - Cationic, Anionic, and Ampholytic Hydrogels. *Journal of Applied Polymer Science* **1993,** 49, (9), 1553-1563.

23.   van den Brom, C. R.; Anac, I.; Roskamp, R. F.; Retsch, M.; Jonas, U.; Menges, B.; Preece, J. A., The swelling behaviour of thermoresponsive hydrogel/silica nanoparticle composites. *Journal of Materials Chemistry* 20, (23), 4827-4839.

24.   Dostalek, J.; Kasry, A.; Knoll, W., Long range surface plasmons for observation of biomolecular binding events at metallic surfaces. *Plasmonics* **2007,** 2, (3), 97-106.

25.   Huang, C. J.; Dostalek, J.; Knoll, W., Optimization of layer structure supporting long range surface plasmons for surface plasmon-enhanced fluorescence spectroscopy biosensors. *Journal of Vacuum Society and Technology B* **2010,** 28, (1), 66-72.

26.   Wang, Y.; Huang, C.-J.; Jonas, U.; Wei, T.; Dostalek, J.; Knoll, W., Biosensor based on hydrogel optical waveguide spectroscopy. *Biosensors and Bioelectronics* **2009,** 25, (7), 1663-1668.

27.   Schiebener, P.; Straub, J.; Sengers, J.; Gallagher, J. S., REFRACTIVE-INDEX OF WATER AND STEAM AS FUNCTION OF WAVELENGTH, TEMPERATURE AND DENSITY. *Journal of Physical and Chemical Reference Data* **1990,** 19, (3), 677-717.

28.   Singh, J.; Weber, M. E., Kinetics of one-dimensional gel swelling and collapse for large volume changes. *Chemical Engineering Science* **1996,** 51, (19), 4499-4608.

FIGURE CAPTIONS

Figure 1 Schematics of NIPAAm-based hydrogel system and its modification with protein molecules by using active ester chemistry.

Figure 2 Sensor chip with embedded indium tin oxide (ITO) micro-heater and SPR-active layer architecture with thermo-responsive hydrogel layer on the top.

Figure 3 Optical setup employed for the spectroscopy of LRSP modes combined with SPR imaging and surface plasmon-enhanced fluorescence spectroscopy (SPFS) for detection of molecular analytes captured in a hydrogel matrix.

Figure 4 Micro-heater calibration: (a) LRSPR response measured at a fixed angle of θ=48.7 deg for the bare gold surface in contact with water upon its heating and relaxing back to the background temperature T_0=23 °C and (b) typical calibration curve showing the equilibrium temperature T_{eq} depending on the current flow I through the ITO pad.

Figure 5 (a) Angular reflectivity spectra measured upon the probing of un-modified NIPAAm-based hydrogel film swollen in water at temperatures T_0= 20, 30, 33 and 35 °C. (b) Temperature depending swelling ratio $\Phi=d_h/d_{h\_dry}$ of un-modified NIPAAm-based hydrogel film swollen in wate

Figure 6 Comparison of the temperature depending equilibrium swelling ratio $\Phi=d_h/d_{h\_dry}$ for the unmodified hydrogel (triangles), hydrogel modified by ETA (diamonds), and hydrogel modified with mouse IgG molecules with surface mass density $\Gamma=8.2$ (circle) and 26.4 ng/mm^2 (squares) swollen in PBS. Lines represent the fitted reflectivity curves by using a Fresnel reflectivity-based model.

Figure 7 (a) Kinetics of swelling and collapse of un-modified NIPAAm-based hydrogel film that is swollen in water seen from LRSPR reflectivity changes. A current pulse was flowed through the ITO micro-heater with the magnitude between $I=5$ mA and 13 mA leading to an increase in the equilibrium temperature from $T_{eq}=25$ to 34 °C. (b) Obtained time-evolution of hydrogel film thickness d_h upon its swelling and collapse as a response to a temperature pulse inducing an increase of the temperature from $T_0=20$ °C to $T_{eq}=34$ °C.

Figure 8(d) LRSPR reflectivity response to series of temperature pulses for the sensor surface with NIPAAm-based hydrogel and immobilized IgG molecules swollen PBS. Current pulses with the magnitude of 14 mA current were applied with 2 sec interval and the background temperature was set to $T_0=20$ °C.

Figure 9 (a) Angular reflectivity and fluorescence spectra of hydrogel film modified with mouse-IgG in PBS buffer before and after capture of labeled anti-mouse goat-IgG, and (b) hydrogel film modified with mouse-IgG and labeled anti-mouse goat-IgG upon the temperature change from 23℃ to 35℃ by applying a current to ITO pad. (c), Time evolution measurement of reflectivity and fluorescence intensity upon the current flow to ITO pad at angle of 47.5 deg. Inserted

pictures are fluorescence images of sensor patch at the excitation angle of HOW mode with(b) and without(a) current flow.
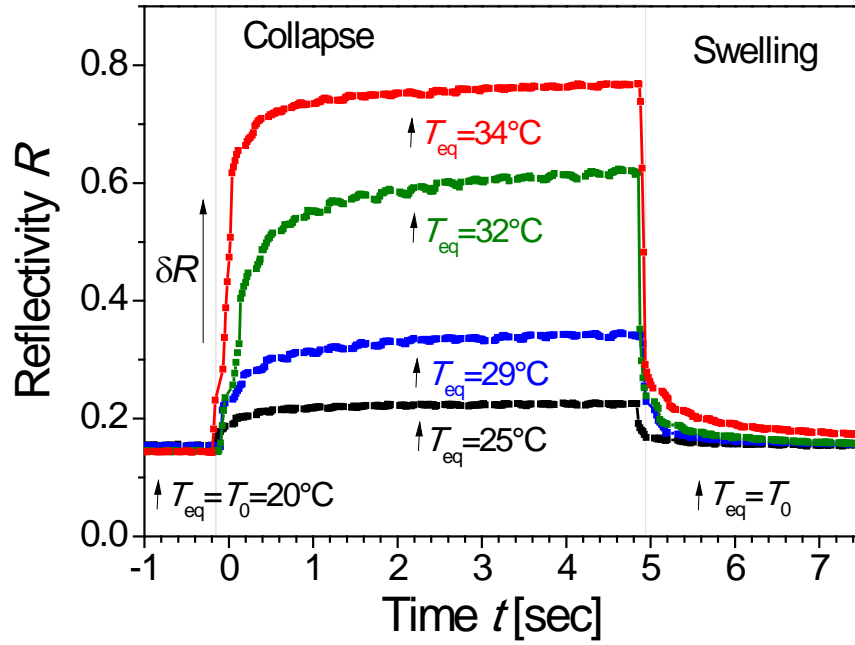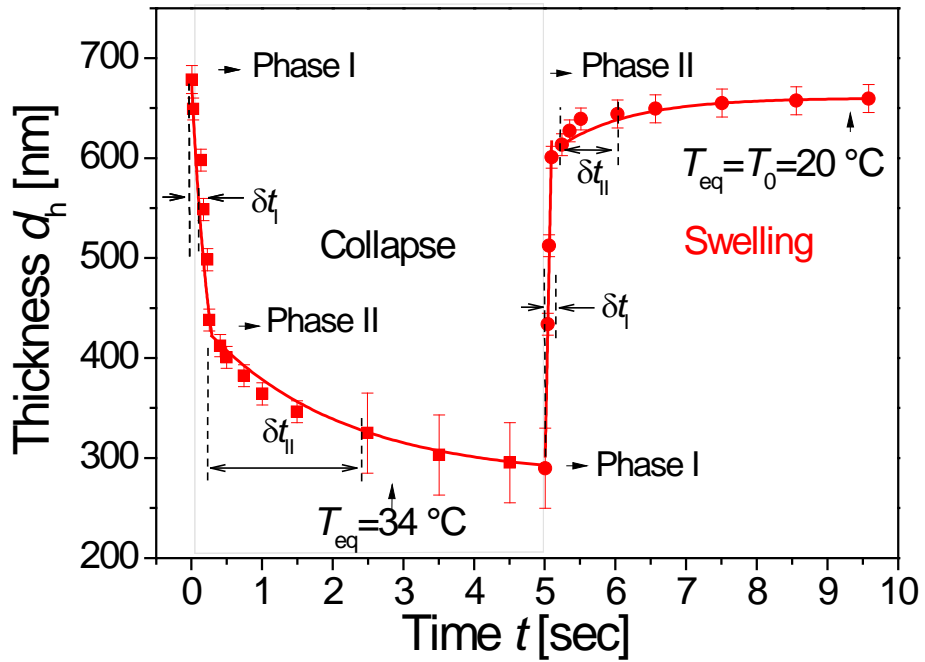
Figure 1
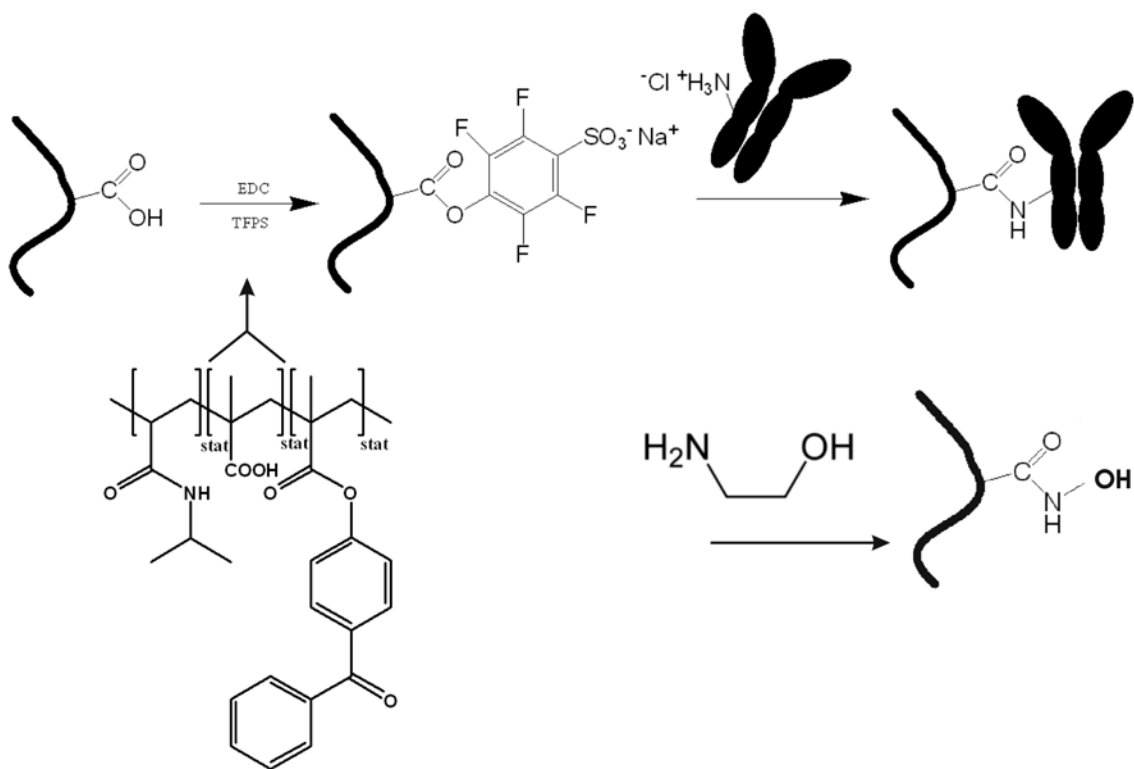
Figure 2
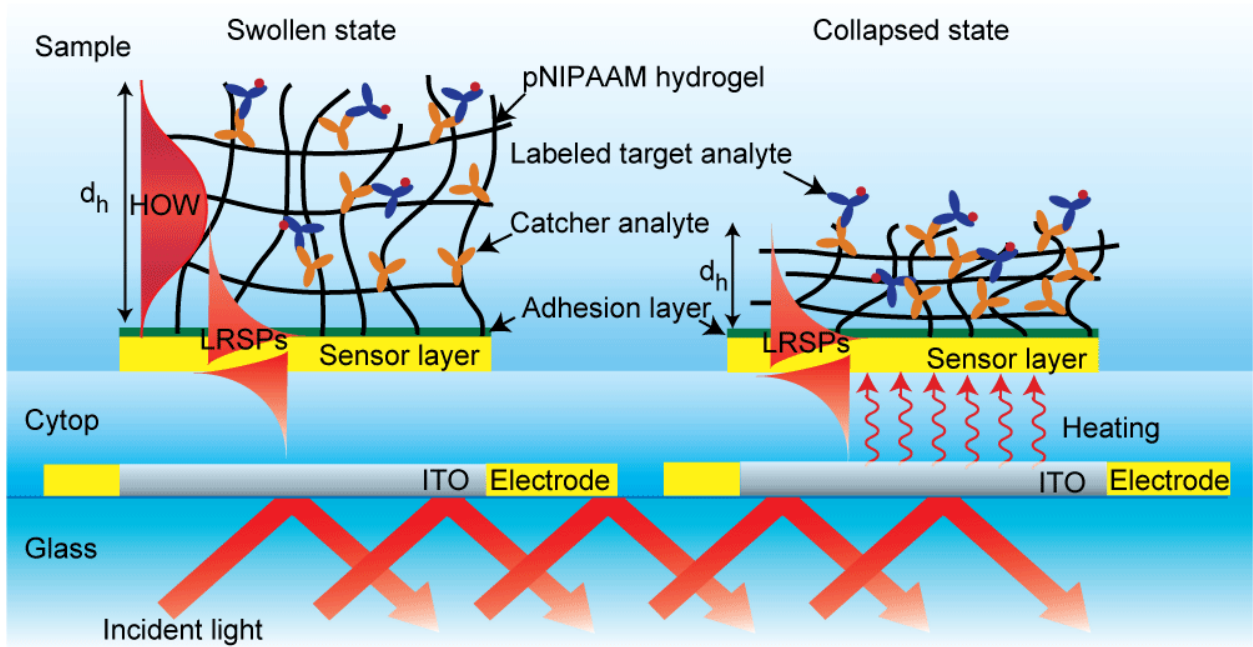
Figure 3
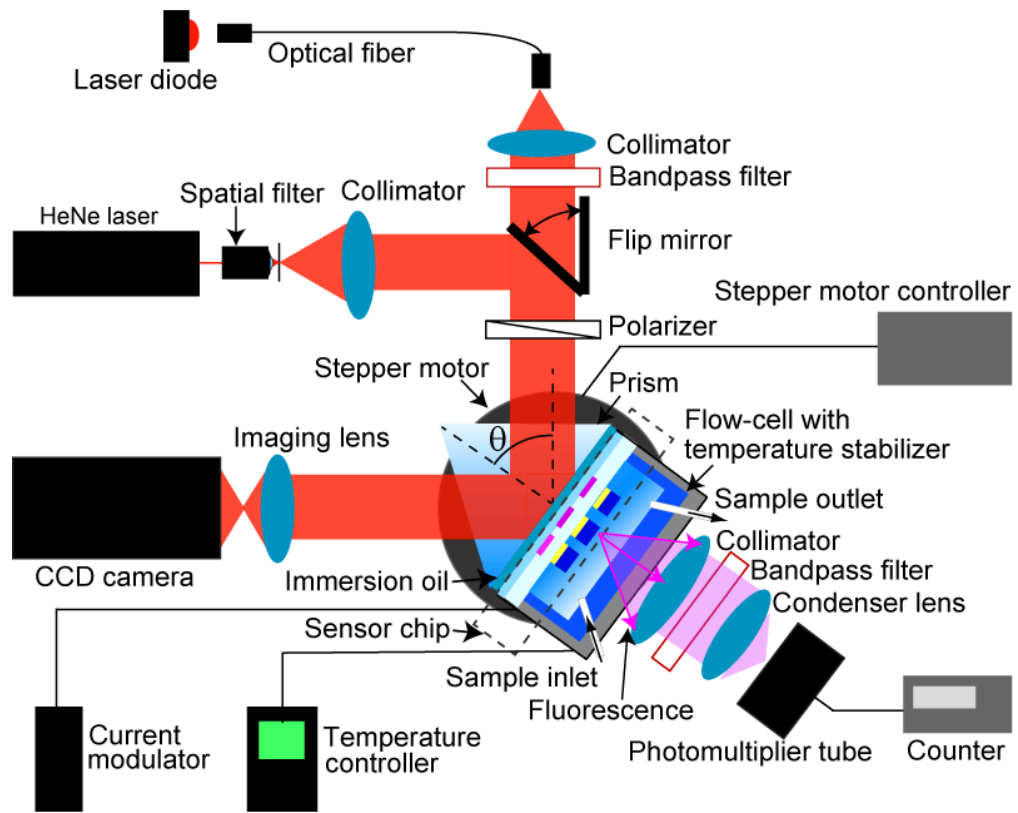
Figure 4

(a)

(b)

Figure 5

(a)

(b)

Figure 6

The figure shows swelling ratio $d_h/d_{h\text{-dry}}$ versus Temperature T_0 [°C], labeled "In PBS", with curves:
- (1) $\Gamma{=}0$ ng/mm^2, COOH
- (2) $\Gamma{=}0$ ng/mm^2, ETA
- (3) $\Gamma{=}8.2$ ng/mm^2, ETA
- (4) $\Gamma{=}26.4$ ng/mm^2, ETA
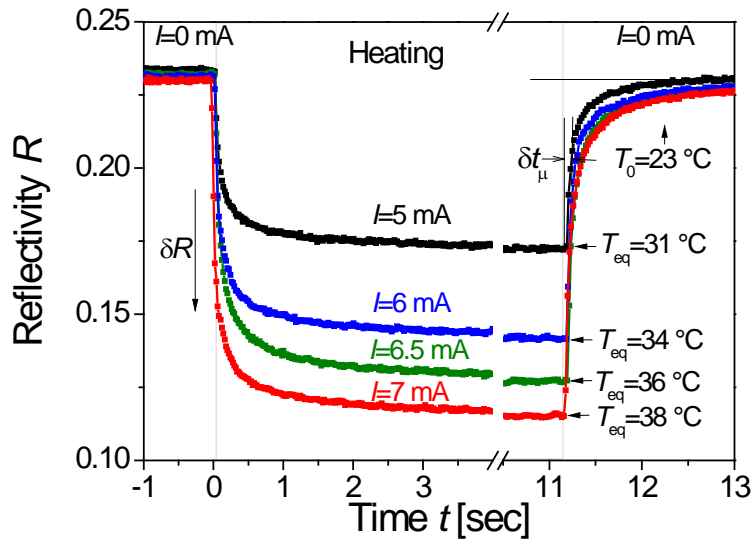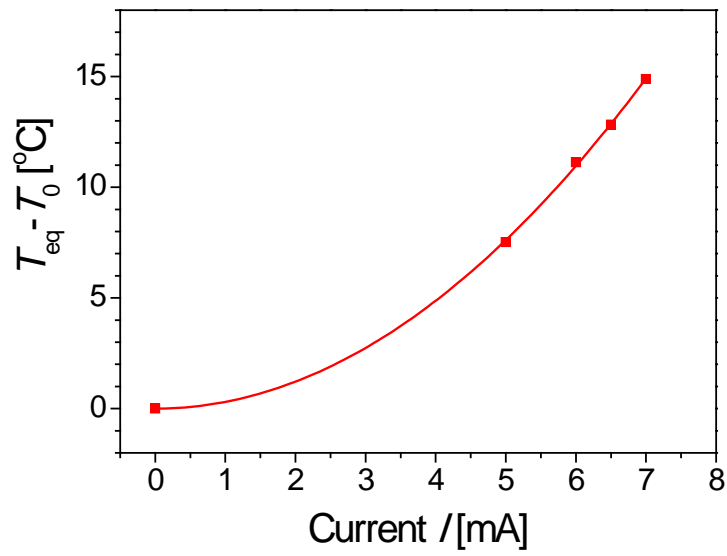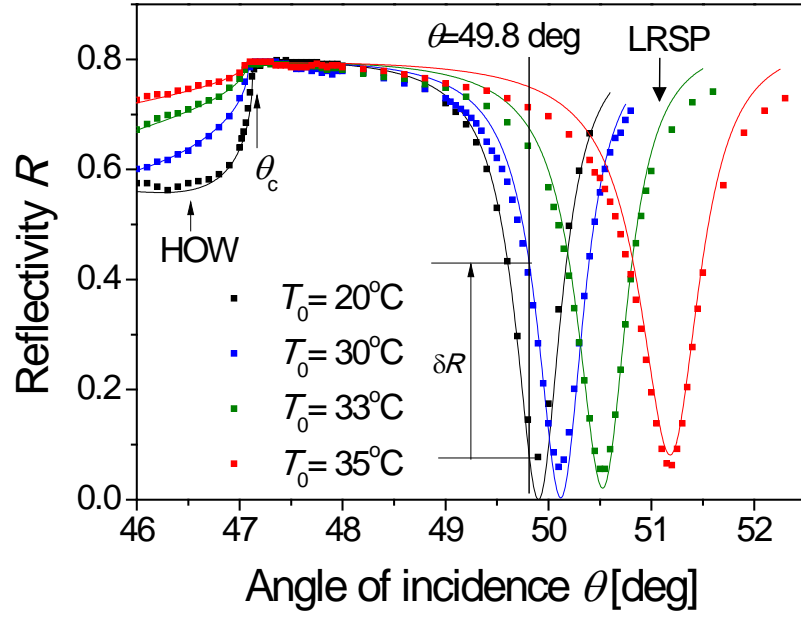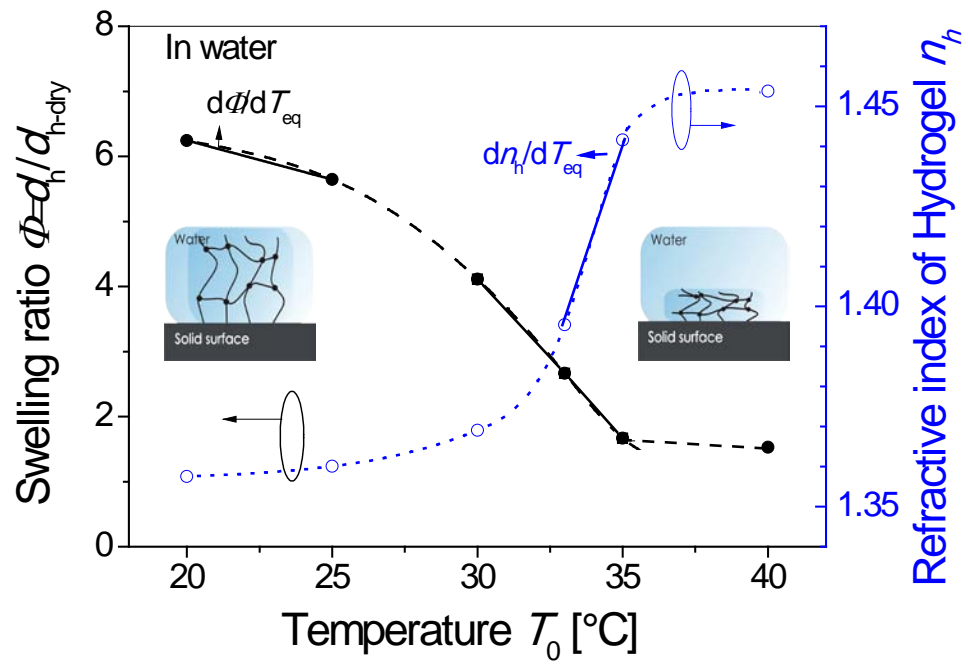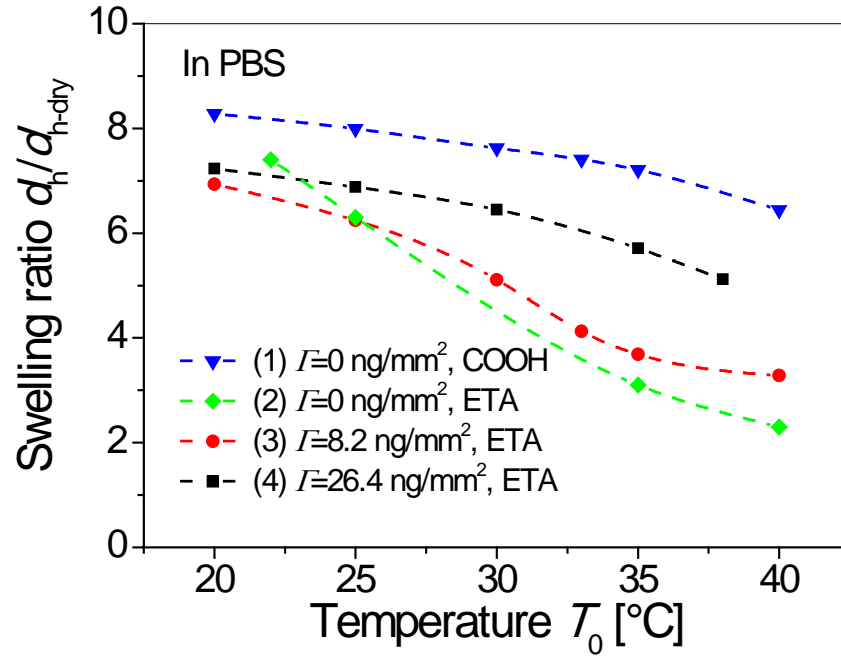
Figure 7

(a)

(b)
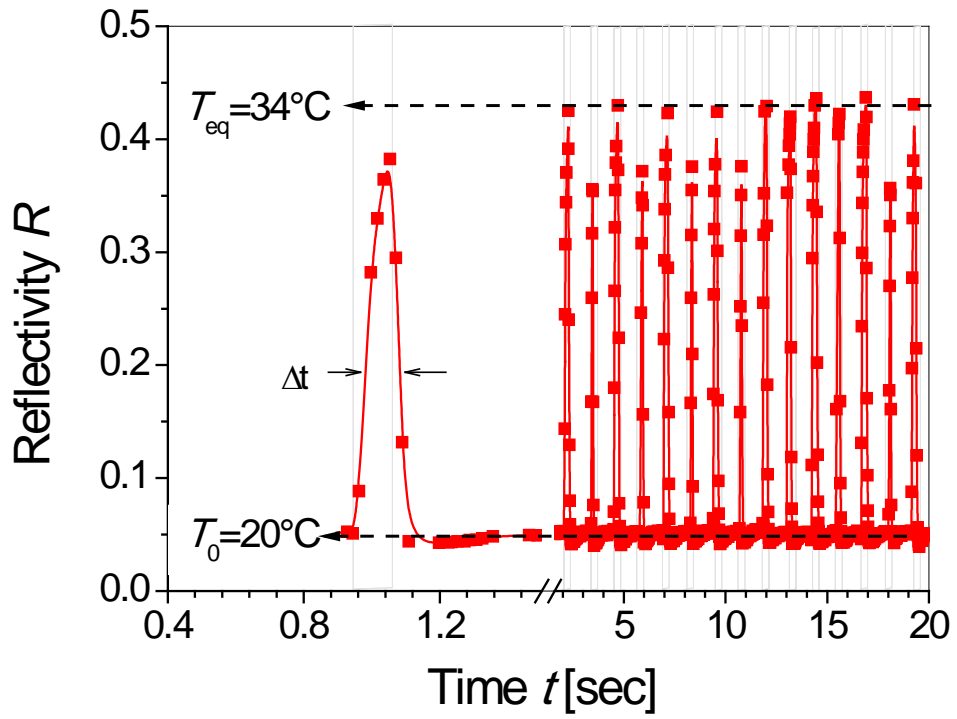
Figure 8

Figure 9
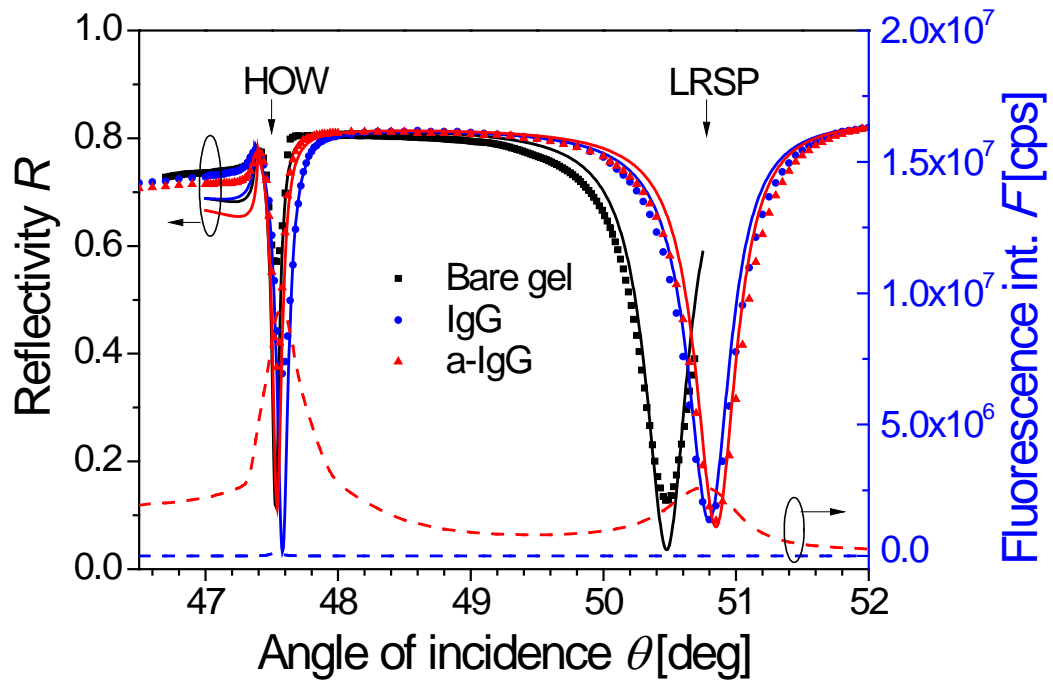
(a)
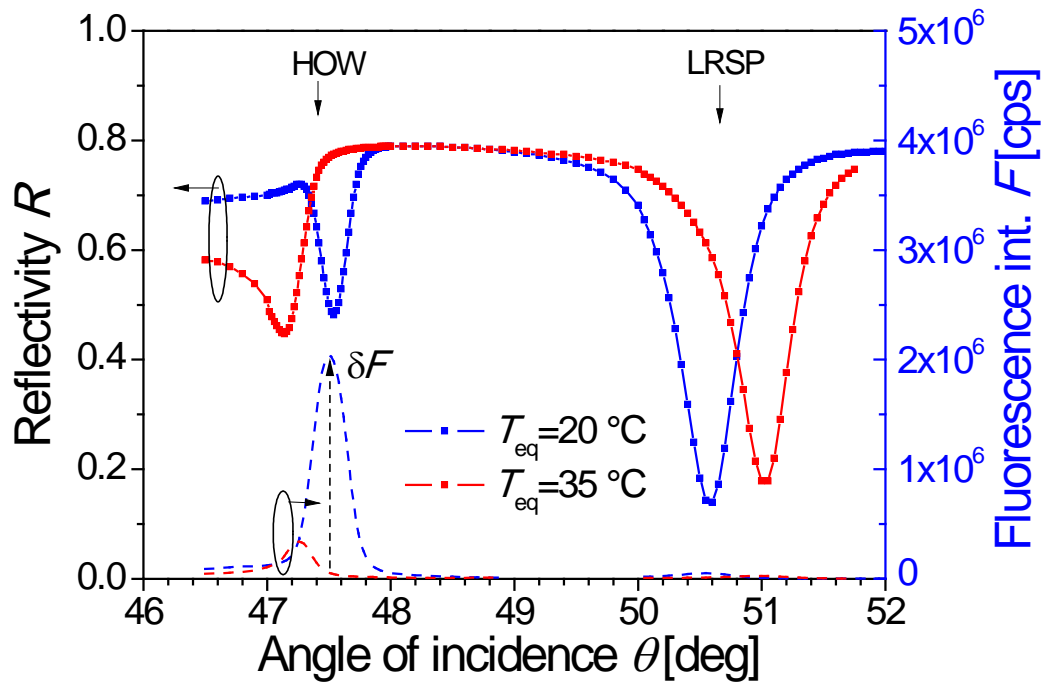
(b)
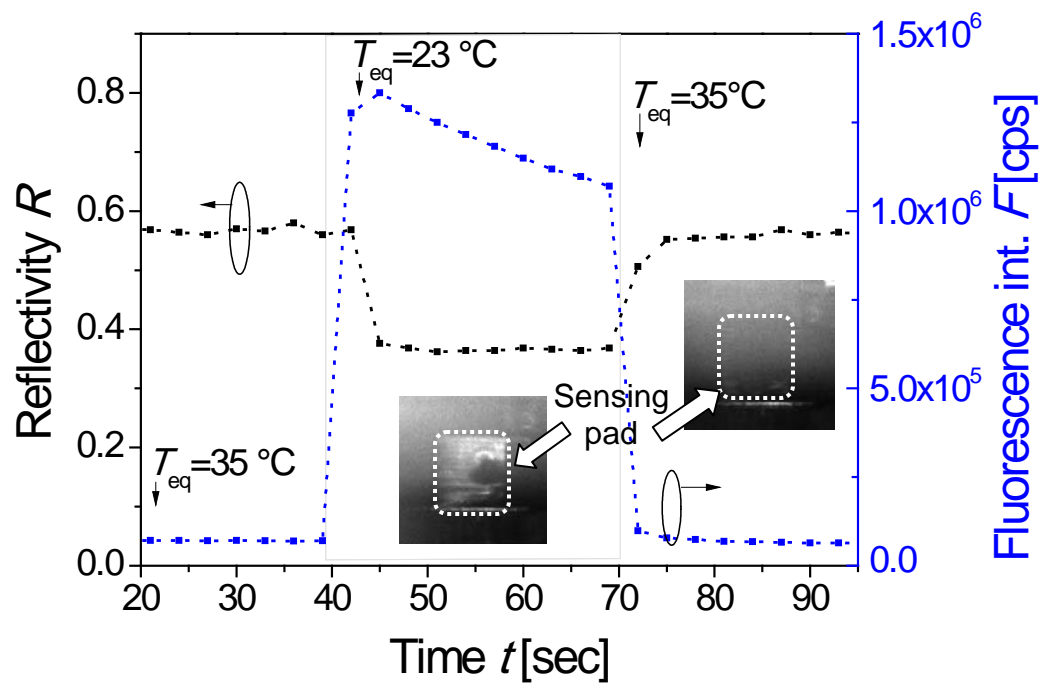
(c)

Plasmonic biosensor schemes with thermo-responsive hydrogel binding matrix

Mana Toma, Wolfgang Knoll and Jakub Dostalek*
Health and Environment
AIT – Austrian Institute of Technology GmbH
Vienna, Austria
*jakub.dostalek@ait.ac.at

Anca Mateescu, Ulrich Jonas
BOMCLab
FORTH/IESL
Heraklion, Greece

Abstract—**We propose a new approach for surface plasmon-enhanced fluorescence spectroscopy (SPFS) biosensor with efficient collecting of molecular analytes from a sample at the sensor surface. It is based on a responsive hydrogel binding matrix that is tethered on a metallic sensor surface and that can reversibly swell and collapse upon triggering by an external stimulus. The swelling is associated with a rapid uptake of an aqueous sample into the matrix and subsequent selective binding of a specific analyte to the catcher molecules anchored to the matrix. Upon the collapse the gel, the sample fluid is expelled and the captured analyte is compacted in close proximity to the sensor surface where large field enhancement occurs. We pursue this approach by using an indium tin oxide (ITO) microheater with surface plasmon-supporting metallic layer and thermo-responsive poly(*N*-isopropylacrylamide) (PNIPAAm) hydrogel on the top. The NIPAAm-based gel can be functionalized with catcher molecules and we show that the developed setup enables rapid cycling of its swelling / collapsing state by temperature modulation around 32 °C.**

I. INTRODUCTION

In biosensors based on surface plasmon-enhanced fluorescence spectroscopy (SPFS), a liquid sample with a target analyte is brought in contact with catcher molecules immobilized on the metallic sensor surface, where the analyte binding events are probed in the surface plasmon field with highest intensity at the metal-liquid interface. This field excites fluorophore-labeled molecules in proximity to the surface and directly increases the strength of measured fluorescence signal the closer the analytes to the metal surface [1]. In our laboratory, we pursued research to further advance the sensitivity of SPFS biosensor technology by increasing the field enhancement, controlling the angular spectrum of fluorescence light, and employing large binding-capacity biointerfaces [2-4].

II. CONCEPT

In SPFS and other methods utilizing heterogeneous assay-based detection of molecular analytes, the sensitivity is hindered by a slow diffusion of the analyte molecules from a sample volume to the sensor surface. We propose a new concept for rapid collecting of analytes and their compacting on the sensor surface for improved sensitivity of SPFS detection. This detection scheme is based on a thermo-responsive hydrogel matrix that is functionalized with catcher

molecules. This matrix can rapidly swell and collapse by an external stimulus (such as temperature changes) and thus actively drive target analyte to the surface, see Fig.1. Firstly, a sample with the target analyte is brought in contact with the collapsed hydrogel that is modified with appropriate catcher molecules (a). Consequently, the hydrogel is rapidly swollen by water molecules from the sample solution, which drags the analyte into the sensor matrix (b). Finally, the collapse of the hydrogel biding matrix is externally triggered, which expels the excess sample volume from the matrix and compacts the selectively captured analyte molecules in close proximity to the sensor surface (c).

III. MATERIALS AND METHODS

A. Sensor chip

Microheaters with gold electrodes (50 nm thick Au layer with 3 nm of Ta adhesion layer) and ITO pads (thickness 50-100 nm) were deposited on BK7 glass using magnetron sputtering and laser-cut stencil masks. Afterwards, 46 nm thick Au pads were prepared on top of ITO microheaters with a 300 nm thick Ta_2O_5 layer in between as insulator layer. The Au sensor surface was modified with S-3-(benzoylphenoxy)propyl ethanthioate (BP-thiol) followed by spincoating poly(*N*-isopropylacrylamide) (PNIPAAm)-based hydrogel as described previously [5].
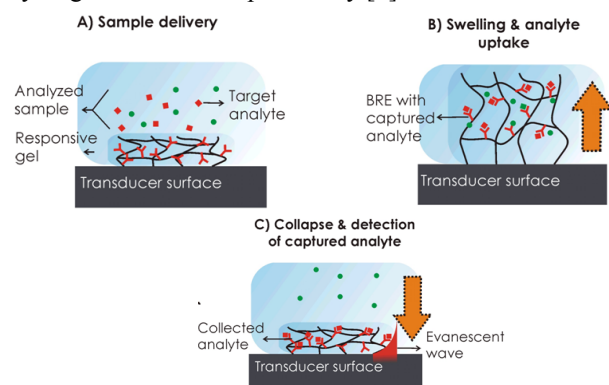

Fig.1 Schematic of "analyte fishing " based on a responsive hydrogel matrix: a) sample with a target analyte is delivered to the sensor surface, b) the hydrogel binding matrix is swollen by uptake of a sample, and c) the hydrogel is collapsed and the bound analyte compacted on the surface for evanescent wave detection.

The hydrogel with a thickness in the dry state of $d_{dry}=200$ nm was simultaneously crosslinked and attached to the surface by exposing to UV light (wavelength 365 nm, irradiation dose of 2 J cm^{-2}). The used PNIPAAm-based hydrogel carries carboxylic groups (that can be further modified with capture molecules [6]) and exhibits a lower critical solution temperature T_c = 32 ˚C. The NIPAAm-based hydrogel is below T_c in the swollen state, and collapsed above T_c.

B. Experimental setup

An optical setup based on attenuated total reflection (ATR) method in Kretschmann configuration was employed for the observation of the thermo-responsive hydrogel film. As shown in Fig. 2, TM polarized light at a wavelength of 633 nm (from a He-Ne laser or a halogen lamp with narrow transmission band pass filter) was coupled to a 90° LASFN9 optical prism. A SPR sensor chip was optically matched to the prism base by using refractive index matching oil, and a flow cell was attached to its surface in order to pass liquid samples. The intensity of the laser beam reflected from the prism base was measured with a photodiode detector and a lock-in amplifier (Model 5210, Princeton Applied Research) or a CCD camera (piA1000-48gm, BASLER). The sensor head assembly comprising a prism, sensor chip and a flow cell was mounted on a two-circle rotation stage (Huber GmbH) in order to measure angular reflectivity spectra R(θ) or temporal reflectivity changes R(t) at a fixed angle in the steep slope of the SPR dip. The whole sensor head was temperature stabilized by a Peltier device and a temperature control driver (LFI3751, Wavelength Electronics). The gold electrodes of the ITO microheaters were connected to a current modulator (NI9265, National Instruments) and the electric current passing through the ITO layer (with the resistance of 280 Ω) allowed rapid heating in close proximity to the sensor surface.

IV. RESULTS AND DISCUSSIONS

A. Temperature calibration

In order to calibrate the ITO microheater, we observed SPR changes due to the temperature modulated refractive index of water. Firstly, the temperature of the whole sensor chip was controlled by a Peltier device and the reflectivity was recorded at temperatures between T = 20 and 40 °C.
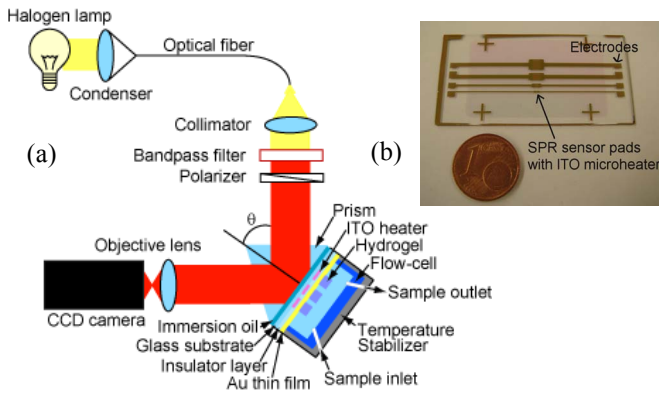
Fig.2 (a) Schematics of the optical setup and (b) photograph of the sensor chip carrying four different sizes of ITO micro-heaters.

Afterwards, the Peltier temperature control was set to T = 20 °C and increasing current was flowed through the ITO micro-heater. The temperature changes in close proximity to the sensor surface were observed by the corresponding SPR reflectivity changes R(t), as seen Fig.3 (a).One can see that after a current flow is applied, the reflectivity R(t) rapidly decreases due to a decreasing refractive index of water at the sensor surface. The correlation of the observed reflectivity changes with the temperature setting of the Peltier control allowed calibration of the equilibrium temperature with respect to the heater current, as plotted in Fig.3 (b). The rise and fall times defined as the time after which the induced reflectivity change reached half of its maximum value were 100-200 ms.

B. Thermoresponsive properties of the PNIPAAM-hydrogel

Fig. 4 (a) shows typical angular spectra R(θ) measured for a gold surface with a swollen (T = 20 °C) and collapsed (T = 35 °C) hydrogel film in contact with water. The evaluated dependence of the refractive index n_h (proportional to density) and thickness d_h of the hydrogel on temperature T were obtained by fitting reflectivity curves with a transfer matrix-based model and is displayed at Fig.4 (b). It reveals that a temperature increase from 28 °C to 33 °C translates to a dramatic decrease in the thickness d_h from 1.7 µm to 0.38 µm. The temporal changes of the refractive index n_h (inversely proportional to the thickness d_h) of the hydrogel upon applying temperate pulses from T = 20 to 46 °C were probed by SPR. The sensorgram in Fig.4 (c) shows that the half maximum change in the reflectivity was reached at around 200 ms, which is similar to the response measured without the hydrogel (see Fig.3 (a)).
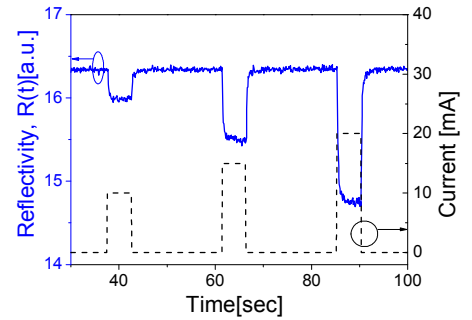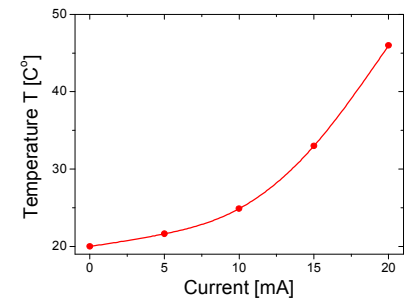
Fig. 3 (a) Temporal changes of the SPR reflectivity R(t) in response to the current flow through an ITO micro-heater with the resistance of 280 Ω and area of 2 mm^2. (b) Dependence of the equilibrium temperature at the sensor surface on the heater current.

The response time of a hydrogel to an external stimulus scales with a characteristic size Δx and a diffusion coefficient D_g of the network as $\sim \Delta x^2 / D_g$ [6]. For the hydrogel films with thickness 1 μm, this corresponds to the response time in the range of 0.1-10 milliseconds, which can be reached through further design optimization of the ITO microheater.

V. CONCLUSIONS

We developed a new sensor setup for the excitation and interrogation of surface plasmons with integrated ITO microheater. The setup was employed for a rapid control of swelling and collapsing of a thin thermo-responsive hydrogel film attached to its surface. It allowed changing the temperature between 20 and 46 °C with a time resolution around 100 milliseconds.

(a)

(b)

(c)
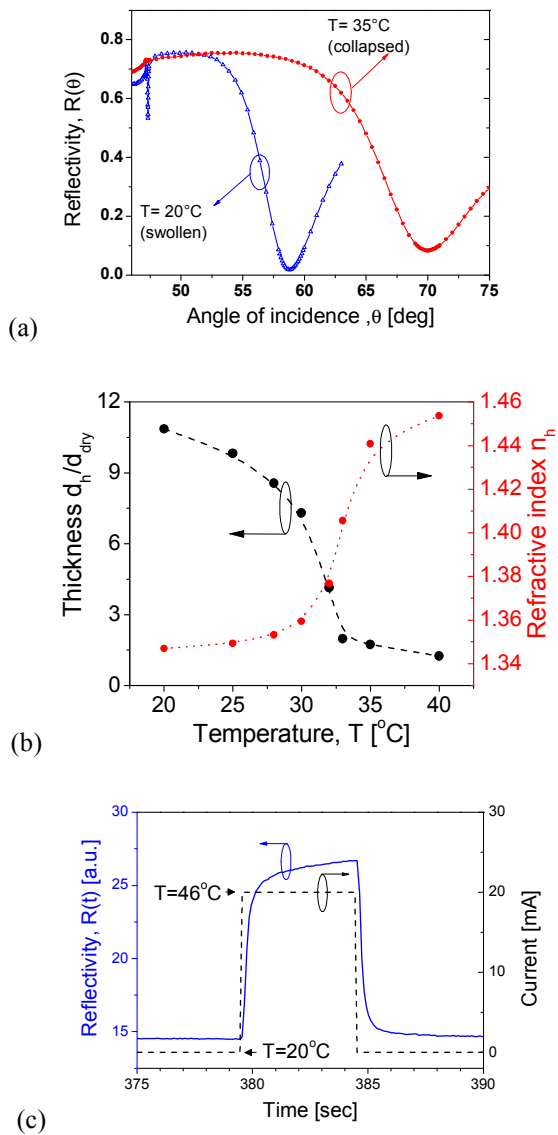
Fig.4 (a) Typical angular spectra of a swollen and collapsed hydrogel in water. (b) Dependence of refractive index and thickness of the hydrogel on equilibrium temperature. (c) Temporal evolution of the SPR reflectivity R(t) upon temperature modulation in thermo-responsive hydrogels in dependence of the appled current in the ITO micro-heater.

We show that the PNIPAAm-based hydrogel film with the swelling ratio of ~10 and the thickness ~2 μm undergoes reversible swelling and collapsing at the time scale below hundreds of millisecond (observations were limited by the current time resolution of the setup) which is orders of magnitude faster compared to that observed for more bulky structures used in e.g. actuators [7].

In the next step, the developed system with thermo-responsive PNIPAAm-based hydrogel will be functionalized and employed for the biosensor application with analyte collection. In addition, let us note that the reported approach holds potential for actuating surface plasmons. The approaches pursued up to now based on electro-optical modulation [8], magneto-optical [9], and thermo optical modulation [10] allow refractive index modulation $< 10^{-3}$ refractive index units (RIU), which is often not sufficient for actuating surface plasmons with relatively short propagation length. The responsive hydrogels can provide much higher refractive index modulation $\sim 10^{-1}$ RIU and millisecond response times.

REFERENCES

[1] J. Dostalek and W. Knoll, "Biosensors based on surface plasmon-enhanced fluorescence spectroscopy," *Biointerphases,* vol. 3, pp. 12-22, 2008.

[2] K. Toma, J. Dostalek, and W. Knoll, "Long range surface plasmon-coupled emission for biosensor applications," unpublished.

[3] Y. Wang, A. Brunsen, U. Jonas, J. Dostalek, and W. Knoll, "Prostate Specific Antigen Biosensor Based on Long Range Surface Plasmon-Enhanced Fluorescence Spectroscopy and Dextran Hydrogel Binding Matrix," *Analytical Chemistry,* vol. 81, pp. 9625-9632, 2009.

[4] C. J. Huang, J. Dostalek, and W. Knoll, "Long range surface plasmon and hydrogel optical waveguide field-enhanced fluorescence biosensor with 3D hydrogel binding matrix: On the role of diffusion mass transfer," *Biosens. Bioelectron.,* vol. 26, pp. 1425-1431, 2010.

[5] P. W. Beines, I. Klosterkamp, B. Menges, U. Jonas, and W. Knoll, "Responsive thin hydrogel layers from photo-cross-linkable poly(N-isopropylacrylamide) terpolymers," *Langmuir,* vol. 23, pp. 2231-2238, 2007.

[6] I. Tokarev and S. Minko, "Stimulli-responsive hydrogel thin films," *Soft Matter,* vol. 5, pp. 511-524, 2009.

[7] J. Wang, Z. Chen, M. Mauk, K.-S. Hong, M. Li, S. Yang, and H.-H. Bau, "Self-Actuated, thermo-responsive hydrogel valves for lab on a chip," *Biomedical Microdevices,* vol. 7, pp. 313-322, 2005.

[8] M. J. Dicken, L. A. Sweatlock, D. Pacifici, H. J. Lezec, K. Bhattacharya, and H. A. Atwater, "Electrooptic Modulation in Thin Film Barium Titanate Plasmonic Interferometers," *Nano Letters,* vol. 8, pp. 4048-4052, Nov 2008.

[9] V. V. Temnov, G. Armelles, U. Woggon, D. Guzatov, A. Cebollada, A. Garcia-Martin, J.-M. Garcia-Martin, T. Tomay, A. Leitenstorfer, and R. Bratschitsch, "Active magneto-plasmonics in hybrid metal-ferromagnet structures," *Nature Photonics,* vol. 4, p. 107, 2010.

[10] G. Gagnon, N. Lahoud, G. A. Mattiussi, and P. Berini, "Thermally acivated variable attenuation of long-range surface plasmon-polariton waves," *Journal of Lightwave Technology,* vol. 24, pp. 4391-4402, 2006.

Hydrogel optical waveguide spectroscopy based biosensor for label-free detection of small molecules

Mana Toma[1], **Qingwen Zhang**[1], **Ulrich Jonas**[2,3], **Wolfgang Knoll**[1] and **Jakub Dostalek**[1,*]

[1] AIT – Austrian Institute of Technology GmbH, Vienna, Austria
[2] Foundation for Research and Technology - Hellas (FORTH), Institute of Electronic Structure & Laser (IESL), Heracleion, Greece
[3] University of Siegen, Department of Chemistry and Biology, Siegen, Germany
*jakub.dostalek@ait.ac.at

Introduction

Surface plasmon resonance (SPR) biosensors have established as a method enabling rapid direct detection of molecular analytes in various important fields including medical diagnosis, food control and environmental monitoring. However, they **lack the sensitivity** for the analysis of **low molecular weight analytes** (molecular weight < 5 kDa) which does not produce detectable RI changes when captured on the sensor surface. **Hydrogel optical waveguide spectroscopy** (HOWs) was proposed for improving refractive index resolution and sensitivity of this detection platform [1,2] based on **large figure of merit (FOM)** and **binding capacity**.

Objectives

1. Implementation of HOWS with **high refractive index resolution** and for **reference-compensated measurements**
2. Demonstration of **direct detection** of low **MW target analyte** (drug vancomycin with MW of 1450)

Layer architecture on the sensor surface

UV cross-likable poly(N-isopropylacrylamide) (PNIPAAm)-based hydrogel was attached to sensor surface in order to simultaneously serve as a waveguide and binding matrix for the capture of target analyte.
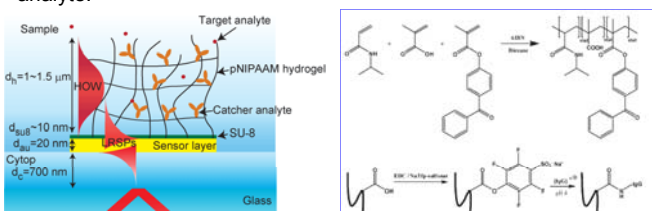
Fig. Layer architecture supporting HOW mode (left) and schematics of poly(N-isopropylacrylamide) (PNIPAAm)-based hydrogel binding matrix (right).

References

[1] Y. Wang et al., *Biosens. Bioelectron.*, (2010), 25, 1663-1668.
[2] A. Aulasevich et al., *Macromol. Rapid Commun*, (2009), 30, 872-877.
[3] M .J. Rybak et al., *Clin. Infect. Dis.* (2010), 211, 1018-1025.
[4] Y. Wang et al., *Anal. Chem.* (2009) 81, 23, 9625-9632

Optical setup & data processing

ATR coupling method with Kretschmann geometry was employed. The angular reflectivity spectra from four channels were imaged at a CCD camera and averaged in time (over 100 times). The angular position of HOW modes is determined by polynomial fitting the averaged spectra.
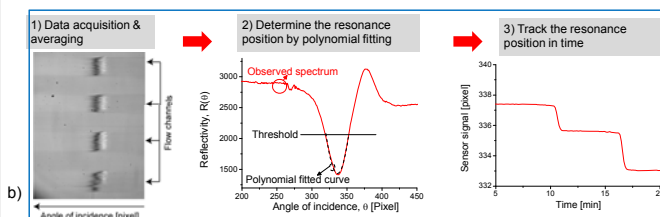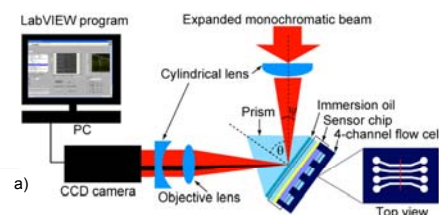
Fig. a) Optical setup for four-channel HOWS biosensor and b) data processing diagram.

Bulk refractive index resolution

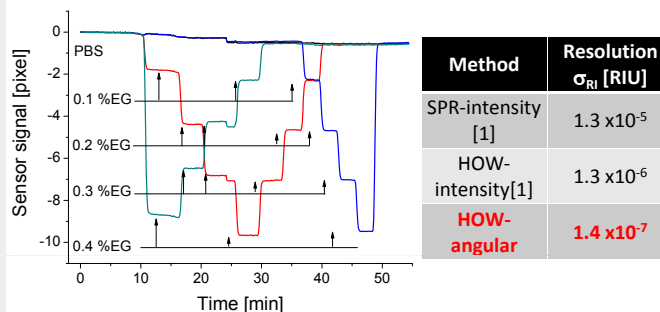| Method	Resolution σ_RI [RIU]
SPR-intensity [1]	1.3×10^{-5}
HOW-intensity[1]	1.3×10^{-6}
HOW-angular	**1.4×10^{-7}**

Fig. Time resolved angular measurement of HOW mode upon the injections of PBS buffer spiked with ethylene glycol at concentration from 0.1 to 0.4 %.

Sensitivity consideration

Surface mass density $\Delta\Gamma$ due to analyte capture ($\partial n_h / \partial c = 0.2$ mm³/mg)

$$\Delta\Gamma = \frac{(\Delta n_h)d_h}{\partial n / \partial c}$$

Surface mass density of IgG antibody (MW ~ 160 kDa) for d_h~1 μm.

Γ=10-100 ng/mm² [4]

Estimated RI change due to the capture of vancomycin (MW ~ 1450)

$\Delta n_h < 10^{-5} – 10^{-4}$

The RI resolution σ_{RI} is about 100 times lower than the estimated maximum RI change Δn_h induced by capture of vancomycin.

Vancomycin biosensor – preliminary data

Vancomycin – a glycopeptide antibiotic used in the prophylaxis and treatment of infections caused by Gram-positive bacteria – was detected with the developed reference compensated HOW sensor.
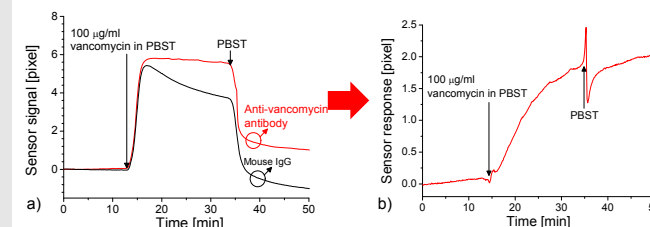
Fig. a) Time resolved angular measurement of HOW mode upon the injections of 100 μg/ ml in PBST, the sensing channel and reference channel was functionalized with anti-vancomycin antibody and mouse IgG, respectively. b) Reference compensated sensor response.

Summary

- Angular spectroscopy of HOW modes from four sensing channels was developed.
- The sensor performance characterization revealed refractive index resolution as low as 1.4×10^{-7} RIU.
- Preliminary data on detection of vancomycin by immunoassays are presented. Future work will include further exploitation for the analysis of small target analyte (e.g., estradiol MW = 272 g/mol).

PLASMON-ENHANCED FLUORESCENCE BIOSENSOR WITH ACTIVE RESPONSIVE HYDROGEL BINDING MATRIX

M. Toma[a], A. Mateescu[b], U.Jonas[b,c], W. Knoll[a], J. Dostalek[a,*]

[a] AIT Austrian Institute of Technology GmbH, Vienna, Austria
[b] FORTH/IESL, Heraklion, Greece
[c] University of Siegen, Germany

Jakub.Dostalek@ait.ac.at

In surface plasmon resonance (SPR) [1] and surface plasmon-enhanced fluorescence (SPFS) [2] biosensors, target analyte contained in a liquid sample is brought in contact with a metallic surface carrying biomolecular recognition elements. The specific capture of target analyte from the sample on the sensor surface is probed by resonantly excited surface plasmons and detected either from binding-associated refractive index changes (SPR) or from surface plasmon-amplified fluorescence signal (SPFS). In general, SPR and SPFS biosensors rely on diffusion of target analyte to the sensor surface which limits their sensitivity. In this contribution, we present a new approach for manipulating with molecular analytes on the sensor surface by using responsive three-dimensional hydrogel binding matrix that is modified with biomolecular recognition elements. As seen in figure below, the hydrogel matrix is tethered to the metallic sensor surface and can rapidly swell and collapse by an external stimulus. Firstly, a sample with target analyte is delivered on top of a collapsed hydrogel (1). Afterwards, the hydrogel is rapidly swelled which is associated with diffusion of water molecules and drag analyte into the matrix (2). Finally, the hydrogel biding matrix is collapsed which leads to expelling of the sample from the matrix and compacting of captured analyte molecules in close proximity to the sensor surface followed by SPFS readout (3). We implemented this approach by using an SPFS sensor chip with ITO microheater for rapid temperature modulation and thermo-responsive poly (N-isopropylacrylamid) hydrogel (PNIPPAm) – based binding matrix. As showed in our laboratory [3], this hydrogel can be functionalized with protein catcher molecules and exhibits a dramatic change in its swelling ratio when temperature is modulated around 33 ℃ (> 10 in water). An SPFS sensor scheme with the temperature modulation on the sensor surface (amplitude ΔT>10 °C and characteristic time <100 ms) was developed. The performance characteristics of the concept will be demonstrated in terms of improved analyte mass transfer to the surface, fluorescence signal strength and limit of detection for SPFS readout and model immunoassay experiment.
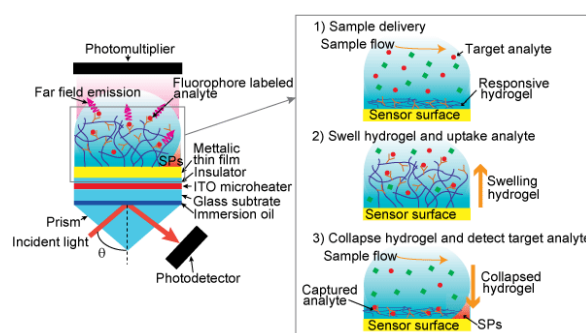

Fig. New scheme of active biointerfaces for manipulating with molecular analyte on the surface of SPR and SPFS biosensor

[1]   J. Homola, Surface plasmon resonance sensors for detection of chemical and biological species, Chemical Reviews, (2008), 108, 462-493.
[2]   T. Liebermann, W. Knoll, P. Sluka and R. Herrmann, Complement hybridization from solution to surface-attached probe-oligonucleotides observed by surface-plasmon-field-enhanced fluorescence spectroscopy, Colloids and Surfaces a-Physicochemical and Engineering Aspects, (2000), 169, 337-350.
[3]   P. W. Beines, I. Klosterkamp, B. Menges, U. Jonas and W. Knoll, Responsive Thin Hydrogel Layers from Photo-Cross-Linkable Poly(N-isopropylacrylamide) Terpolymers, Langmuir, (2007), 23, 2231-2238.

Plasmon-enhanced fluorescence biosensor with active responsive hydrogel binding matrix

Mana Toma[1], **Anca Mateescu**[2], **Ulrich Jonas**[2,3], **Wolfgang Knoll**[1] **and Jakub Dostalek**[1],*

[1] AIT – Austrian Institute of Technology GmbH, Vienna, Austria
[2] Foundation for Research and Technology - Hellas (FORTH), Institute of Electronic Structure & Laser (IESL), Heracleion, Greece
[3] University of Siegen, Department of Chemistry and Biology, Siegen, Germany
*jakub.dostalek@ait.ac.at

Introduction

Hydrogel optical waveguide-enhanced fluorescence spectroscopy (HOW-FS) is a method enabling highly sensitive and rapid detection of molecular and biological analytes [1]. In this method, an analyte in a liquid sample is flowed over a metallic sensor surface covered with hydrogel thin film with catcher molecules. The hydrogel thin film provides high binding capacity of catcher analyte and serves as optical waveguide supporting layer [2]. The capture of fluorophore-labeled molecules is detected from the increased intensity of fluorescence. Among the various types of hydrogel, poly(N-isopropylacrylamide) (pNIPAAm)-based hydrogel exhibits responsiveness to external stimuli such as temperature, pH and ionic strength which opens up a new sensor scheme advancing sensor performance [3-4].

Objective
To demonstrate a new sensor concept for parallel detection of multiple analytes with conventional SPFS setup by actuating sensor signal by thermo-responsive hydrogel binding matrix and ITO microheater

Experimental setup & surface architecture

The experimental setup which enables to spatial resolved reflectivity measurement and temperature control was developed based on the optical setup for angle-resolved reflectance/fluorescence spectroscopy with ATR coupling method. A sensor chip with ITO microheater which supports HOW mode and long range surface plasmon mode was prepared.
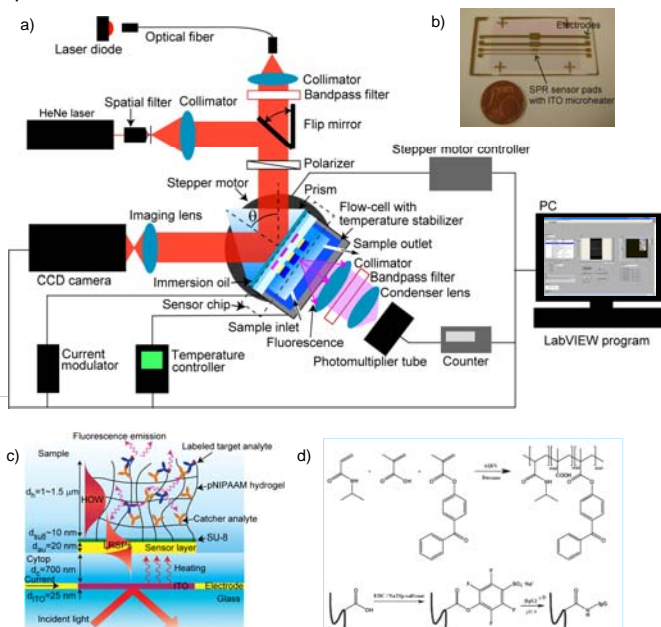

Fig. a) Sketch of an optical setup of combined surface plasmon resonance imaging (SPRi) and surface plasmon fluorescence spectroscopy, b) SPR sensor chip with ITO microheater, c) the layer architecture and d) UV cross-linkable poly(N-isopropylacrylamide) (PNIPAAm)-based hydrogel binding matrix [2]

Immunoassay with HOW-FS

Model immunoassay with mouse IgG and labelled anti-mouse IgG was carried out with HOW-FS readout. The LOD of anti IgG was determined to be 30 fM for 30 min of analysis time [1].
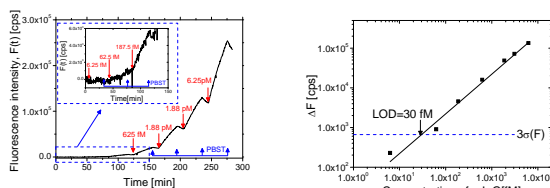

Fig.a) Binding kinetics of labelled anti-mouse IgG at various concentrations. b) Calibration curve of HOW-FS biosensor for detection of anti-IgG fitted with a linear function. The baseline noise and LOD are indicated.

References

[1]   C.J. Huang et al., *Biosens. Bioelectron.*, (2010), 26, 1425-1431.
[2]   A. Aulasevich et al., *Macromol. Rapid Commun*, (2009), 30, 872-877.
[3]   I. Anac et al., *Macromol. Chem. Phys.* (2010), 211, 1018-1025.
[4]   C.J. Huang et al.; *Proc. SPIE 2009*, Vol. 7356, 735625
[5]   M. Toma et al., *Proc. Biophotonics 2011*, 8-10 June 2011, Italy, page 1-3

Swelling property of protein-loaded pNIPAAM hydrogel

Temperature depending equilibrium swelling properties of pNIPAAm hydrogel functionalized with mouse IgG in PBS was studied by SPR spectroscopy. The hydrogel collapsed about 2 times at T= 38 ℃.
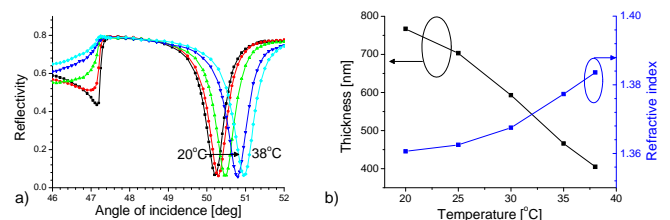

Fig.a) Angular reflectivity spectra of hydrogel modified with mouse IgG as at various temperatures. b) Fitted thickness and refractive index of hydrogel layer as a function of temperature.

Fast temperature modulation by ITO microheater

The response time of hydrogel against thermal stimulation was investigated by time resolved reflectivity measurement. The fast temperature modulation by ITO microheater enables to switch swell/collapse state of hydrogel within 1 sec [5].
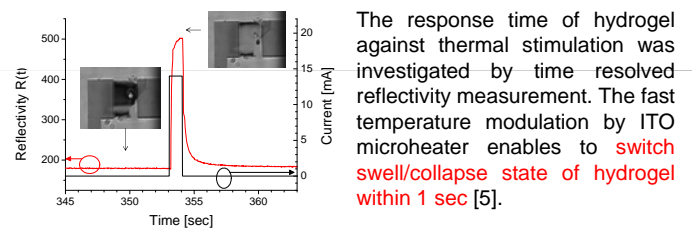
Fig.Typical time resolved reflectivity measurement of hygdrogel response against currrent. The inserted pictures are SPR images of swollen /collapsed hydrogel .

Fluorescence signal manipulation

Fluorescence signal from captured anti-mouse IgG excited by HOW mode was manipulated with developed sensor chip by current flow.
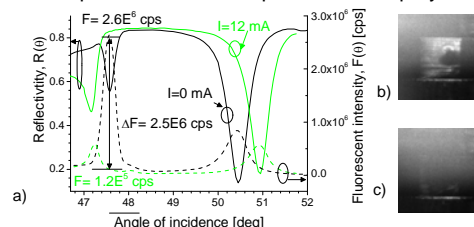

Fig.a) Angular reflectivity and fluorescence spectra of hydrogel modified with mouse IgG and labelled anti-mouse IgG. SPFS images at resonance angle of HOW mode depending on the applied current b) I= 0 mA and c) I= 12 mA .

Summary

- A new sensor chip which enables to reversibly switch on and off fluorescence signal of HOW-FS was developed. This scheme is based on thermo responsiveness of hydrogel which serves as binding matrix and optial waveguide supporting layer on top of ITO microheater.

- Future work will include parallel detection of multiple target analyte in a model immunoassay.

BRAGG-SCATTERED SURFACE PLASMONS FOR HIGH RESOLUTION SPR IMAGING

M. Toma, J. Dostalek[*], W. Knoll

AIT Austrian Institute of Technology GmbH, Vienna, Austria

jakub.dostalek@ait.ac.at

Over the last years, surface plasmon resonance (SPR) imaging (also referred to as surface plasmon microscopy)[1] become an increasingly popular tool for sensitive and label-free readout of microarrays in high throughput biomolecular interaction analysis (BIA) and biosensors for parallel detection of multiple target analytes.[2][3] This method relies on probing the spatial distribution of refractive index changes on the sensor surface by surface plasmons – guided waves propagating along metal-dielectric interfaces. Besides others, the characteristics of surface plasmons depend on used materials and wavelength. For the commonly used gold SPR-active surfaces, the maximum refractive index resolution is obtained for the wavelengths around $\lambda=800$ nm.[3] However, at this wavelength the propagation length of surface plasmons reaches of about 30 µm that significantly deteriorates the spatial resolution of SPR imaging. Up to date, investigated approaches based on surface plasmons propagating with larger damping (at lower wavelength or on stronger absorbing metals) were shown to achieve higher-spatial resolution SPR imaging (up to 2 µm),[4,5] however they inherently suffer from a lower accuracy in refractive index measurement (contrast). In this contribution, we present a new approach based on Bragg-scattered surface plasmons (BSSPs) supported by a nano-structured metallic surface enabling to achieve both high spatial resolution (near diffraction-limited) and accuracy of the measurement of refractive index changes in SPR imaging.
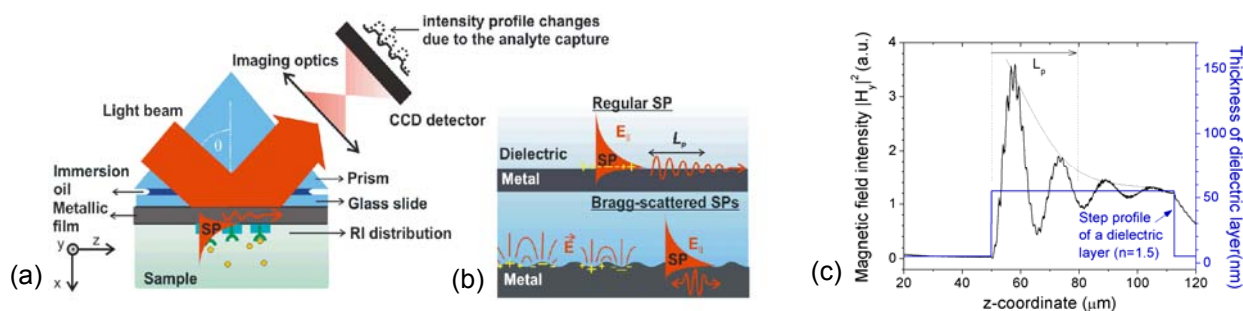

Fig. (a) Typical implementation of SPR imaging. (b) Scheme of the a metallic surface supporting regular SPs and the BSSPs (c) Simulated magnetic field intensity reflected from a gold film (50 nm thickness) with a step in the refractive index of a dielectric layer on its top.

Finite element method (FEM)-based theoretical study of Bragg-scattered surface plasmons on periodically modulated metallic surfaces and their implementation for refractometric sensors will be presented. The parameters of the nano-structured metallic surface (including period and depth and profile of a periodic modulation) allowing the excitation of Bragg-scattered surface plasmons will be determined and the key performance characteristics of the regular and BS-SPR imaging sensors evaluated. Spatial resolution of SPR imaging will be evaluated from simulations of a reflected light beam intensity profile upon the excitation of BSSPs that probe a spatial refractive index features on a metallic surface. These simulations reveal that probing by BSSPs and SPs provide a similar the refractive index resolution (quantified by figure of merit - FOM). Due to their fact that BSSPs are non-propagating surface plasmon modes (exhibiting standing wave nature), we expect they will enable improving the spatial resolution of SPR imaging. We envisage that the tailoring of properties of surface plasmons in SPR biosensors will open new ways for their applications in areas such as very high density microarrays.

[1] B. Rothenhäusler, W. Knoll, *Nature* (1988), 332, 615-617.
[2] S. Scarano et al. *Biosensors and Bioelectronics* (2009) in press.
[3] J. Homola, *Chemical Reviews* (2008), 108, 462-493.
[4] M. Piliarik, J. Homola, *Optics Express* (2009), 17, 16505-16517.
[5] C. E. H. Berger et al., *Review of Scientific Instruments* (1994), 65, 2829-2836.
[6] K. F. Giebel et al. *Biophysical Journal* (1999),76, 509-516

Bragg-scattered surface plasmons for high resolution SPR imaging

Mana Toma, Jakub Dostalek, Wolfgang Knoll

AIT Austrian Institute of Technology GmbH, Health & Environmental Department
Donau-City-Strasse 1, 1220 Vienna (Austria). E-mail: Mana.Toma.fl@ait.ac.at

Introduction

Over the last years, surface plasmon resonance (SPR) imaging[1] become an increasingly popular tool for sensitive and label-free readout of microarrays in high throughput biomolecular interaction analysis (BIA) and biosensors for parallel detection of multiple target analytes.[2] This method relies on probing the spatial distribution of binding-induced refractive index changes on the sensor surface by surface plasmons – guided waves propagating along metal-dielectric interfaces. The characteristics of surface plasmons depend on used materials and wavelength. For commonly used gold surface, the maximum refractive index resolution is obtained for the wavelengths around λ=800 nm.[3] However, at this wavelength the propagation length of surface plasmons reaches of about 30 μm that significantly limits the spatial resolution of SPR imaging. Approaches relying using propagating surface plasmons with large losses (at lower wavelength or on stronger absorbing metals) were shown to improve the spatial resolution but provided deteriorated refractive index resolution[4,5]. Similar, structures supporting localized plasmons allowed achieving almost diffraction limited measurements, the refractive index resolution (contrast) was order of magnitude lower than that for regular SPR imaging[7].
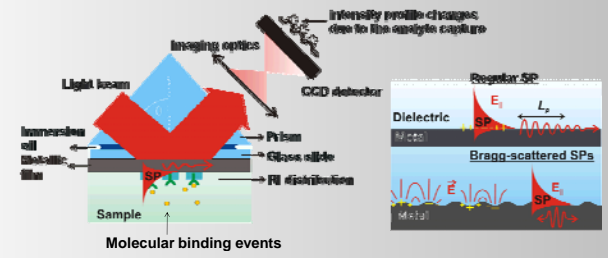

Fig. 1 (a) Typical implementation of SPR imaging. (b) Metallic interfaces supporting propagating SPs and the standing wave Bragg-scattered SPs

Concept of BSSPs supported SPR imager

In this contribution, we present a new approach to SPR imaging which holds potential for both high refractive index sensitivity and spatial resolution near diffraction limit. This approach is based on probing the sensor surface with Bragg-scattered surface plasmons (BSSPs) supported by a nano-structured metallic surface. These modes originate on diffraction coupling counter-propagating SPs on a periodically modulated surface when k_{sp} matches the half value of $2\pi/\Lambda$.

- BSSPs become localized through the scattering as they "bounce back and forth" on the metallic sensor surface - potential for high spatial resolution.
- The losses of BSSP (accumulated propagation length) are similar to that of regular surface plasmons - refractive index sensitivity close to regular SPR[8].
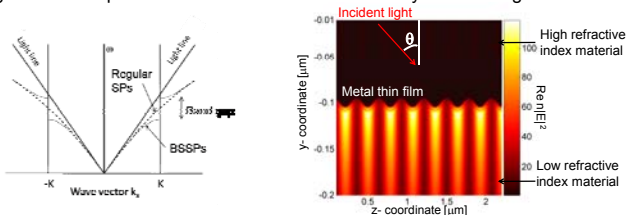

Fig.2 (a) Dispersion curve of BSSPs[6], (b) Electric intensity field of BSSPs on a corrugated 50 nm thick gold film (Λ=285nm, d=10nm).

Methods

Experimental

The implementation of SPR imaging based on attenuated total reflection (ATR) with Kretschmann configuration was employed. Metallic sensor surface was coated by a patterned UV cross-linkable thin NIPAAm-based hydrogel film. The hydrogel was cross-linked by unsing UV light through a mask with array of 70 μm openings in diameter.
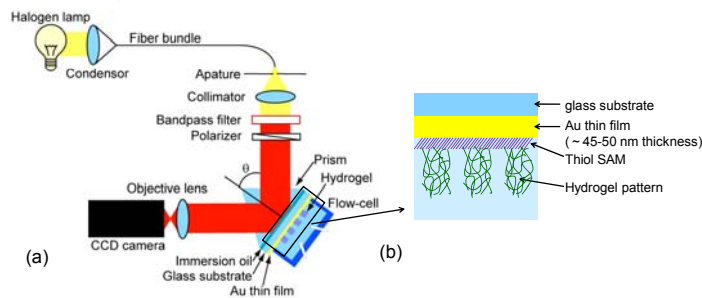

Fig.3 (a) Experimental setup for SPR imaging and (b) metallic sensor surface with deposited hydrogel film.

Simulations

Finite element (FEM) method implemented in the diffraction grating solver DiPoG (Weierstrass Institute, Germany) was employed. This numerical diffraction solver was used for the simulations of the profile of reflected light intensity from the surface of SPR imager and for the simulations of BSSP characteristics.
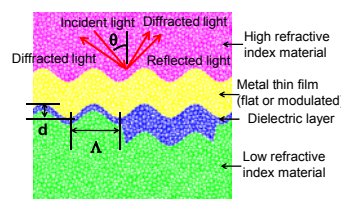

Fig.4 Typical mesh structure.

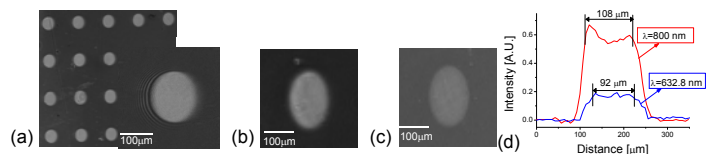## Results

SPR imaging of hydrogel spots array

Fig.5 Experimental SPR images of gold film covered with hydrogel spots array for λ = 800 nm upon the gel was in contact with in air (a) and swollen in water. For the comparison, the same spot was SPR imaged at λ = 633 nm (c). The measured profiles at λ = 633 nm and λ = 800 nm is presented (d).
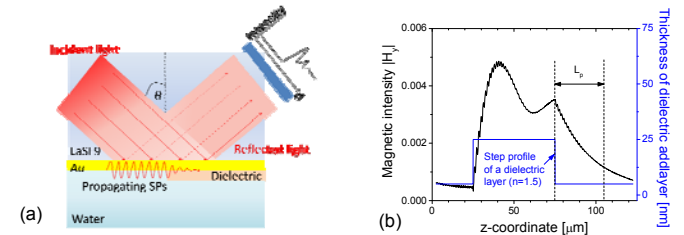

Fig.6 Simulations of the lateral distribution of reflected light upon probing a refractive structure with a refractive index step on a gold surface (a). Magnetic field intensity profile of a reflected light wave (λ = 800 nm) is presented (b).

Probing refractive index changes by Bragg-scattered SPs

Simulations of reflectivity changes due to the refractive index of a 5 nm thick adlayer (approximating binding of biomolecules) on the top of a gold film in contact with water were carried out both of BSSPs and reguler SPs (Fig.7).
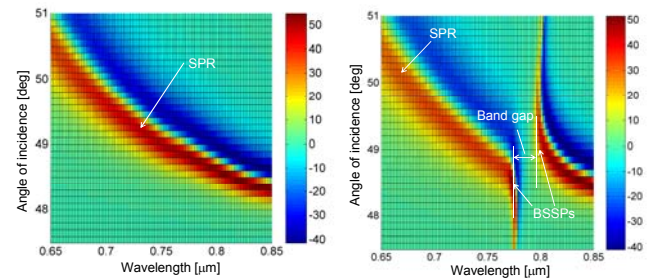

Fig.7 Angular and wavelength dependence of SPR reflectivity difference between a bare gold surface and a gold surface with a 5 nm thick adlayer (δn=0.17): (a) regular SPs on a flat surface, and (b) BSSPs on a corrugated gold film (Λ=285nm, d=10nm).

Summary

- SPR imaging instrument for the observation of a hydrogel microarray was developed and a numerical model for the simulation spatial resolution of SPR imaging was carried out.
- Nanostructured metallic surfaces supporting BSSPs were proposed to advance the spatial resolution SPR imaging method without reducing the refractive index sensitivity (contrast). Design of structures supporting these modes and their refractive index sensitivity was investigated.
- The future work will include the study of spatial resolution of proposed approach, its experimental implementation and application in fields including high density microarrays.

References

[1] B. Rothenhäusler and W. Knoll, *Nature* (1988), 332, 615-617.
[2] J. Homola, *Chemical Reviews* (2008), 108, 462-493.
[3] M. Piliarik and J. Homola, *Optics Express* (2009), 17, 16505-16517.
[4] C. E. H. Berger, et al., *Review of Scientific Instruments* (1994), 65, 2829-2836.
[5] K. F. Giebel, et al., *Biophysical Journal* (1999),76, 509-516
[6] W. L. Barnes et al. *Physical Review* (1996), 54, 6227-6244.
[7] M. E. Stewart, et al., *Applied Physical sciences* (2006), 103, 17143-17148
[8] J. Dostálek, et al., *Optics Letters* (2007), 32 ,2903-2905.